JUNCTION RIEMANN PROBLEM FOR SHALLOW WATER EQUATIONS IN NETWORKS

MOHAMED ABDELREHIM SELIM IBRAHIM ELSHOBAKI

University of L'Aquila

Department of Information Engineering, Computer Science and Mathematics
Hydraulic Engineering Group
via Vetoio (snc), Località Coppito, L'Aquila 67010, Italy

Abstract: In this paper, the Riemann solution of an extended Riemann problem in channel networks is presented. The Riemann problem at a junction network is well defined in the literature. However, it is limited to symmetric networks. Here, we extend the Riemann problem to non-symmetric networks such that neither the channel width equality nor the discharge equality are assumed. The Riemann solution is given under subcritical flow conditions to ensure the existence and uniqueness of the solution at the junction. Taking into account the mass and energy conservation laws, the necessary conditions for the Riemann solution are drawn. The results are summarized in a theorem. The theorem is illustrated with a set of numerical examples.

In order to perform a one-dimensional simulation in channel networks, the inner boundary conditions at the junction (*i.e.*, the channel intersection point) are required. It has turned out that the classical models (*i.e.*, the Equality, Gurram, Hsu models) that have been used to supply such a boundary suffer from many drawbacks.

Thus, here we propose to use the Riemann solution at the junction networks to provide proper boundary conditions. Then, we compare all the junction models together. The junction models are validated against experimental results found in the literature for steady state flows. Generally, the Riemann model shows good results in matching the experimental data. In particular, the Riemann model shows the best results when the bottom discontinues at the junction. For the unsteady state flows, we perform prototype case studies to test the junction models in the channel networks, and the numerical solutions are compared with the analytical solutions. The Riemann model continues to show the best results that agree with the analytical solutions. However, the validation of the junction models in the unsteady state flows remains for future work due to the limited amount of real data.

Keywords: channel network, Riemann problem, subcritical flows, channel junctions, open channel flows, subcritical flows

Abbreviations

PDE **P**artial **D**ifferential **E**quations
SWE **S**hallow **W**ater **E**quations
 1D **O**ne-**D**imensional
CFL **C**ourant **F**redrich **L**ewy stability criterion
SST **S**teady **S**tate **T**ransition

Symbols

A	constant	$(\mathrm{ms^{-1}})$
A	system matrix	(—)
a	polynomial parameter	(m)
b	channel width	(m)
C	constant	$(\mathrm{m^2s^{-1}})$
c	polynomial parameter	$(\mathrm{m^2s^{-1}})$
c	wave celerity	$(\mathrm{ms^{-1}})$
$\mathcal{D}$	fluctuations	(—)
E	specific energy	(m)
Fr	Froude number	(—)
e	errors	(—)
E	relative percentage error	(—)
F	Flux function	(—)
f	function	(—)
G	point quadrature rule	(—)
w	weights	(—)
h	water depth	(m)
h_o^{lm}	depth maximum of left locus curve	(m)
h_o^{rm}	depth minimum of right locus curve	(m)
h_*	depth component of intermediate state	(m)
h_c	critical depth	(m)
$h_{\triangleright}$	water depth component in the junction curve	(m)
i	spatial index $(i=1,2,3)$	(—)
k	channel index $(k=1,2,3)$	(—)
L	channel length	(m)
ℓ^1	norm error	(—)
N	mesh cell number	(—)
Q	total discharge	$(\mathrm{m^3s^{-1}})$
q	specific discharge	$(\mathrm{m^2s^{-1}})$
q_o^{lm}	discharge maximum of left locus curve	$(\mathrm{m^2s^{-1}})$
q_o^{rm}	discharge minimum of right locus curve	$(\mathrm{m^2s^{-1}})$
$\hat{q}$	specific discharge reference	$(\mathrm{m^2s^{-1}})$
q_*	specific discharge component of intermediate state	$(\mathrm{m^2s^{-1}})$
$q_{\triangleright}$	water discharge component in the junction curve	$(\mathrm{m^2s^{-1}})$
r	eigenvector	(—)
u	water velocity	$(\mathrm{ms^{-1}})$
$\hat{u}$	water velocity reference	$(\mathrm{ms^{-1}})$
U	vector of conservative variables	(—)
v	vector of non-conservative variables	(—)
S	vector source term	(—)
s	parameter $(s \in [0,1])$	(—)
t	time	(s)

Δt	time step	(s)
$\mathbf{W}$	vector of cell average of the non-conservative variables	(—)
X	depth ratio	(—)
x	space	(m)
x_j	junction node position	(m)
Δx	spatial step	(m)
$\mathbf{v}_l$	initial left state vector	(—)
$\mathbf{v}_r$	initial right state vector	(—)
$\mathbf{v}_*$	intermediate state vector	(—)
$\mathbf{v}^m$	state minimum or maximum of locus curves	(—)
R	general discharge ratio	(—)
$\mathcal{R}$	rarefaction curve	(—)
$\mathcal{R}^\mathcal{B}$	backward rarefaction curve	(—)
r	discharge ratio	(—)
ω	channels width ratio	(—)
J	junction curve	(—)
o	sub-index refer to initial value	(—)
S_o	bed slope	(—)
S_f	slope friction	(—)
S	shock speed	(ms^{-1})
$\mathcal{S}$	shock curve	(—)
$\mathcal{S}^\mathcal{B}$	backward shock curve	(—)
Y	depth function	(m)
Y^{lm}	maximum depth value of the junction function	(m)
Z	bottom elevation difference at the junction	(m)
z	bottom elevation	(m)
λ	eigenvalue	(ms^{-1})
ζ	an auxiliary variable $\left(\frac{x}{t}\right)$	(ms^{-1})
ξ_l	left locus function	$(\mathrm{m^2s}^{-1})$
ξ_r	right locus function	$(\mathrm{m^2s}^{-1})$
τ_l	left locus curve	(—)
τ_r	right locus curve	(—)
η	non-dimensional water depth	(—)
Γ	non-dimensional water specific energy	(—)
α	angle between representative lateral velocity and main channel direction	(∘)
β	momentum correction coefficient	(—)
γ	energy correction coefficient	(—)
ψ	line integral path	(—)
Ψ	function	(—)
Φ	function	(—)
μ	non-dimensional polynomial parameter	(—)
Δ	discriminant	(—)
δ	junction angle	(∘)
Ω	angle between main upstream and downstream channels	(∘)
Π	boundary edge index	(—)
$\mathcal{Z}$	non-dimensional bottom elevation difference	(—)
θ	polynomial angle	(∘)
Θ	non-dimensional polynomial parameter	(—)

1. General introduction and paper outline

1.1. *The power of one-dimensional shallow water system*

In general, the one-dimensional (1D) shallow water equations (SWE) system has been widely used in water flow simulations [1], where it has been used in single open channels, supported by theoretical findings, see, for example [2−4]. In the recent years, the technology has had a direct impact on the numerical field where high performance computers can easily handle two (2D) and three dimensional (3D) simulations in competitive running time. However, large domains such as rivers that run over thousands of kilometres [5] can limit such facilities. The question whether the use of 2D or 3D models is the best choice for an imagine channel network consisting of thousands of branches and nodes that can be hundreds of kilometres long. Examples of natural junction networks are river bifurcations as seen in Figures 1−3. The computational cost in large networks as such rivers basins remains an obstacle to use 2D and 3D models rather than a 1D model. In the 2D or 3D cases the program running time could be few days or even more. For this reason, the 1D-SWE system remains preferable even with the development of 2D and 3D simulation tools.

Although well known, the 1D-SWE system itself is still a very interesting field of research. It has been used to simulate the water flow in open channel networks [6], however, mathematical difficulties have appeared at the junction network [7]. These difficulties will be addressed in the present paper.
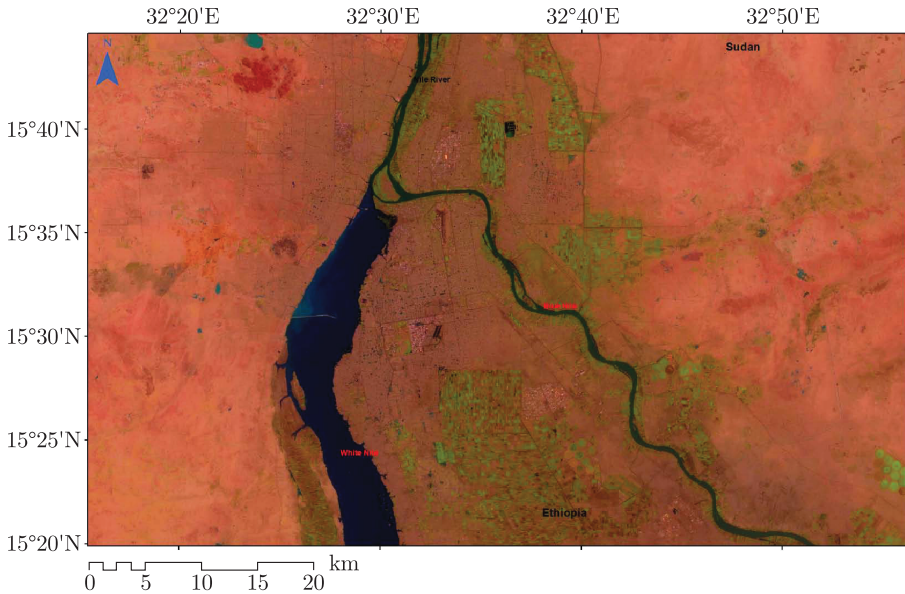

Figure 1. The Blue Nile and the White Nile confluence image taken by Landsat 8 (data available from U.S. geological survey)
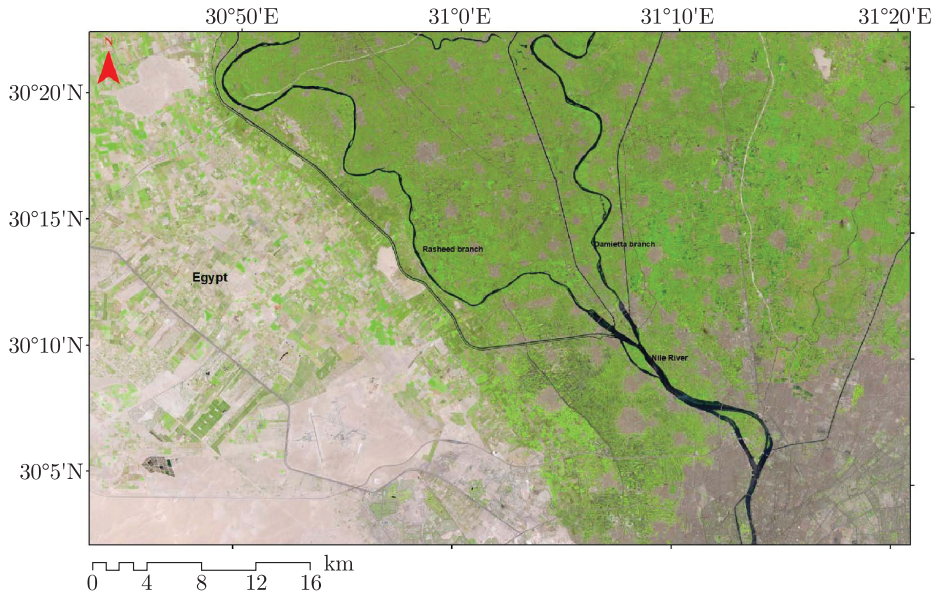
Figure 2. The Nile confluence in Egypt, image taken by Landsat 8 (data available from U.S. geological survey)
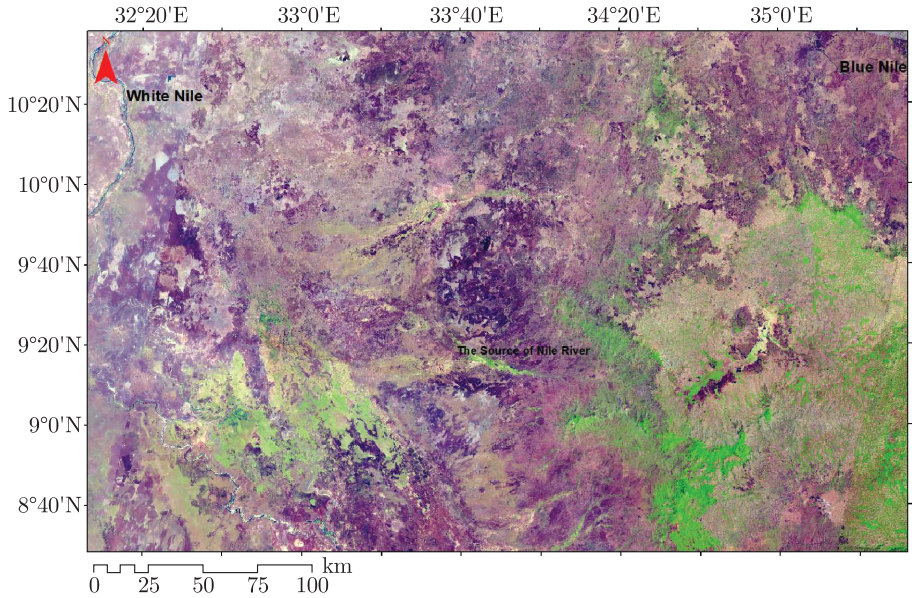

Figure 3. The Nile river basin image taken by Landsat 8 (data available from U.S. geological survey)

1.2. Restriction on using one-dimensional shallow water equations system in channel networks

The 1D-SWE system cannot be used directly at the junction network, where the system becomes singular at the junction. Special methods are required to use the 1D-SWE system at the junction in order to resolve this singularity. It may be useful to use energy and momentum balances at the junction to avoid such singularities in the mathematical model. Many research studies in the literature such as [8–12] depend on energy and momentum balances and suffer from their empirical formulations that limit their ability to address more realistic cases.

1.3. Objectives and organization of the paper

The objectives formulated and accomplished in the paper are as follows:

- The 1D-SWE are redefined at the junction network, taking into account parameters such as the channel width and bed elevation variations at the junction.
- The Riemann problem for the 1D-SWE is defined at the junction in a way avoiding the singularity problem.
- The Riemann problem at the junction is solved recursively, where numerical and geometrical interpretations are given.
- The Riemann solution is mathematically investigated by proving the existence and uniqueness of the solution at the junction, and the necessary conditions to guarantee such results are given.
- The Riemann solution is used as a model to provide the inner boundary conditions for the 1D simulations of channel network flows.
- The Riemann model is compared to classical models in providing the inner boundary conditions.
- All models were tested versus analytical solutions and experimental data.

The paper is organized as follows.

Chapter 2 introduces the partial differential equations of a 1D-SWE system. The SWE properties are given by defining the critical curve. The subcritical and supercritical curves are based on the loci and integral curves. The hyperbolicity of the SWE is discussed. The SWE are strictly hyperbolic under subcritical flow conditions. Some useful lemmas are drawn to be used in further Chapters. The corresponding standard Riemann problem of the 1D-SWE is discussed. A new viewpoint at the Riemann solution is given, based on the geometrical relations between the critical and subcritical curves. Finally, some numerical examples are given.

Chapter 3 shows the Riemann problem for the junction at a junction network with channel width variation and bottom discontinuities at the junction. The Riemann solution is given under subcritical flow conditions. The necessary conditions to ensure the existence and uniqueness of the solution are discussed.

They are associated with such physical interpretation as mass-energy conservations. The junction curves that satisfy the mass-energy conservation at the junction are explained to complete the Riemann solution. Finally, numerical examples are given at the end of the Chapter to illustrate the Riemann solution for the junction from both the geometrical and numerical point of view.

Chapter 4 validates the Riemann problem for junctions in supplying the inner boundary conditions. 1D numerical simulations of the channel network flow are performed. The Riemann model is used together with other models to supply the inner boundary conditions. Other models such as the Equality, Gurram, and Hsu models are modified to fit the presented case studies. The experimental data is used to validate each model. Furthermore, analytical solutions are also used to be compared with the numerical results, where the numerical results are produced by the junction models (the Riemann, Equality, Gurram, and Hsu models). Symmetric and non-symmetric confluences are addressed in this Chapter.

Chapter 5 summarizes the results. The Riemann solution for the junction is validated. The advantages and disadvantages of each junction model are highlighted and discussed. Finally, recommended and possible future works are mentioned.

2. One-dimensional shallow water equations

2.1. Introduction

The shallow water equations (SWE) have been widely used to describe steady and unsteady flows. They represent a simple mathematical model to describe incompressible flows and water waves [13]. Furthermore, they draw more attention from the mathematical point of view because they form the basis of many mathematical models used in simulations of natural phenomena. The currents in oceans, seas, lakes and rivers as well as atmospheric flows can be successively described by the SWE. The SWE are similar to the gas dynamics equations but they are simpler in treatment and manipulation [14]. Looking at any of the handbooks in open channel hydraulic [15, 16], hyperbolic conservation laws [17], or numerical methods [18, 14], we realize the importance of the SWE. Mathematically, the SWE are a class of hyperbolic partial differential equations. They are considered to be a conservative system for the zero source term. For the non-zero source term, they are a system of balance laws. Therefore, the hyperbolic theory in both conservative and non-conservative form can be applied to the SWE [19].

The SWE are written in space and time. Therefore, they can be used to describe unsteady flows. Taking into account the spatial variation only, the SWE are used to describe steady flows. The SWE are also called Saint-Venant equations in the 1D form. For the first time, they were derived by [2]. The SWE are a particular case of Navier-Stokes equations [20] which is obtained by integrating mass and momentum equations over the depth. The horizontal length scale is considered much greater than the vertical length scale.

Motivated by the importance of the SWE, many researches have been concerned about the development of theoretical and numerical treatments of the SWE in a single open channel. In such case, the analytical solutions of the SWE are defined as self-similarity solutions. The solutions combine two dependent space-time variables into one variable by a linear combination using the Rankine-Hugoniot conditions or the Riemann invariant relationships for their corresponding Riemann problems. Solutions are obtained for two different cases.

The first case treats the SWE with the zero source term. The corresponding Riemann problem is solved. The self-similarity solutions are directly obtained by applying the Rankine-Hugoniot and the Riemann invariant for the shock and rarefaction waves, respectively. The solutions depend heavily on the nature of the flow which is either subcritical or supercritical. For the subcritical flow, self-similarity solutions consist of two waves that spread into the left and right directions, associated with the left and right characteristic lines, respectively. Each wave is either a shock or a rarefaction wave. As for the supercritical flow, the two waves propagate in the same direction, more details can be found in [14].

The second case is due to the complexity of the bottom geometry in real life applications. The Riemann problem of the SWE with the non-zero term is extensively treated in the literature, where the bottom is discontinuous. It is the works by [3, 4, 21] that are appreciated among the vast literature. Using the total heat and mass conservation over the bed step, [3] shows how very rich the SWE solutions are. At least 20 different configurations are presented in contrast with only four in the case of the Riemann problem in a single channel of a flat bed. [4] establishes the existence of two-parameter wave sets instead of wave curves. The Riemann solution is constructed. It depends continuously on the left-hand or right-hand sides of the initial states. The Riemann solution does not always exist. In this case, even if the solution exists, it is non-unique and the Riemann problem can admit up to three distinct solutions for different ranges of left-hand and right-hand initial states for the resonance case. [21] presents an exact solution to the SWE with a discontinuous bottom topography, where two certain assumptions are made. Both the conservation of mass and momentum are used to derive the Rankine-Hugoniot conditions across the bottom step in addition to the entropy condition to be fulfilled. No transition between subcritical and supercritical flow conditions is allowed over the bottom step. Therefore, the self-similar solution of the 1D-SWE is shown to be unique and can be computed by solving a set of algebraic equations. Mathematically, the Riemann solution of the 1D-SWE in a single channel is rather well established in the literature.

The purpose of this Section is to form the background that will be used as a tool in the further considerations. The 1D-SWE as well as their solution in a single open channel are presented. In particular, the solution of the Riemann problem of the 1D-SWE is discussed. The wave curves are defined to play an important role for achieving the overall aim of this thesis. The rest of the Chapter is organized as follows: in Section 2.2, we present the mathematical formulation of

the 1D-SWE in a single open rectangular channel. Some useful Lemmas are given in Section 2.3. In Section 2.4, we highlight the Riemann problem of the SWE and its classical standard solution. A set of numerical examples are performed in Section 2.5 to justify the Riemann solution. Finally, the topic of the Chapter is summarized in Section 2.6.

2.2. *Mathematical model*

As stated in the introduction, the 1D-SWE, also known as Saint-Venant equations are defined as a mathematical model to describe an open channel flow in a single channel (Figure 4) by considering that the vertical depth scale is small with respect to the horizontal length scale. Also, the SWE are a particular case of the Navier-Stokes equations, obtained by integrating the mass and momentum equations over the depth. The 1D-SWE can be written in a conservative form as:

$$\frac{\partial \mathbf{U}}{\partial t} + \frac{\partial \mathbf{F}}{\partial x} = \mathbf{S}, \text{ in } [0,L], t \in \mathbb{R}^+, x \in \mathbb{R} \tag{1}$$

with

$$\mathbf{U} = \begin{bmatrix} h \\ hu \end{bmatrix}, \quad \mathbf{F} = \begin{bmatrix} hu \\ hu^2 + \frac{gh^2}{2} \end{bmatrix}, \quad \mathbf{S} = \begin{bmatrix} 0 \\ -gh(S_0 - S_f) \end{bmatrix} \tag{2}$$
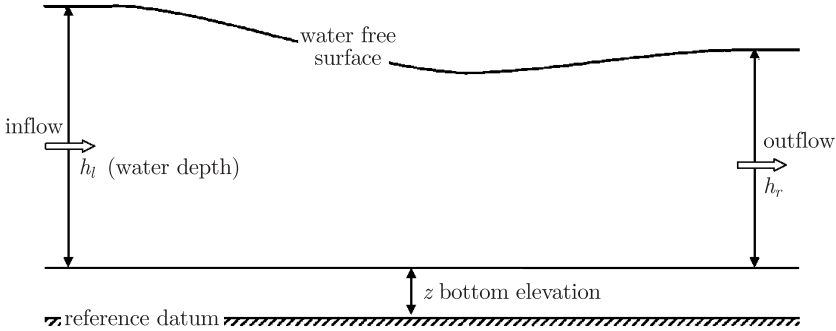

Figure 4. Single open channel flow

where u and h are the flow velocity and the flow depth, respectively. L is the channel length. g is the gravitational acceleration. $S_o = -\frac{\partial z}{\partial x}$ is the bed slope and z is the bottom elevation. S_f is the friction slope computed by taking into account the Manning's formula [15] due to the friction force exerted between the fluid and the bottom materials. Physically, the friction term can be neglected if the channel length is small. Therefore, the Riemann solution is associated to the frictionless case [3], where the friction slope is neglected. It is assumed here to be equal to zero. The flat bottom elevation is considered along the channel. Equation (1) can be cast in a quasi-linear form. This allows considering the bottom elevation as a state variable. Indeed, the movable bed can be present as an important feature in the river geomorphology. However, in this paper we restrict ourselves to a fixed

bottom. At the same time, the state variable z is kept constant in the time variable, for simplicity. Indeed, the 1D-SWE are written in a quasi-linear form as follows:

$$\frac{\partial \mathbf{v}}{\partial t} + \mathbf{A}(\mathbf{v})\frac{\partial \mathbf{v}}{\partial x} = 0, \text{ in } [0, L], t \in \mathbb{R}^+, x \in \mathbb{R} \tag{3}$$

with

$$\mathbf{v} = \begin{bmatrix} h \\ hu \\ z \end{bmatrix}, \quad \mathbf{A}(\mathbf{v}) = \begin{bmatrix} 0 & 1 & 0 \\ c^2 - u^2 & 2u & gh \\ 0 & 0 & 0 \end{bmatrix} \tag{4}$$

The quasi-linear form in Equation (3) allowed [4] to theoretically investigate the Riemann problem in case of a discontinuous bottom. The matrix $\mathbf{A}$ is not the Jacobian matrix for the flux function as for the strictly hyperbolic system. Here, the matrix $\mathbf{A}$ has three real distinct eigenvalues λ_i with indices $i = 1, 2, 3$:

$$\lambda_1(\mathbf{v}) = \frac{q}{h} - c, \quad \lambda_2(\mathbf{v}) = \frac{q}{h} + c, \quad \lambda_3(\mathbf{v}) = 0 \tag{5}$$

where $c = \sqrt{gh}$ is the wave celerity. $q = hu$ is the specific discharge. The corresponding eigenvectors can be chosen as follows:

$$\mathbf{r}_1(\mathbf{v}) = \begin{bmatrix} 1 \\ \frac{q}{h} - \sqrt{gh} \\ 0 \end{bmatrix}, \quad \mathbf{r}_2(\mathbf{v}) = \begin{bmatrix} 1 \\ \frac{q}{h} + \sqrt{hg} \\ 0 \end{bmatrix}, \quad \mathbf{r}_3(\mathbf{v}) = \begin{bmatrix} gh \\ 0 \\ u^2 - gh \end{bmatrix} \tag{6}$$

2.2.1. Critical curves

The critical curves can be defined as curves which separate the subcritical flow and the supercritical flow. Indeed, from the eigenvalues and their corresponding eigenvectors, the first and the third characteristics field coincide as:

$$(\lambda_1(\mathbf{v}), \mathbf{r}_1(\mathbf{v})) = (\lambda_3(\mathbf{v}), \mathbf{r}_3(\mathbf{v})) \tag{7}$$

on a hypersurface and can be identified as the right critical curve as:

$$C^+ := \{(h, q, z) | q = h\sqrt{gh}\} \tag{8}$$

Similarly, the second and the third characteristic fields coincide as:

$$(\lambda_2(\mathbf{v}), \mathbf{r}_2(\mathbf{v})) = (\lambda_3(\mathbf{v}), \mathbf{r}_3(\mathbf{v})) \tag{9}$$

on a hypersurface which is identified by the left critical curve as:

$$C^- := \{(h, q, z) | q = -h\sqrt{gh}\} \tag{10}$$

Here, the first and the third characteristic fields $(\lambda_1, \mathbf{r}_1)$ and $(\lambda_2, \mathbf{r}_2)$ are genuinely nonlinear. The third characteristic field $(\lambda_3, \mathbf{r}_3)$ is linearly degenerate such that

$$-\nabla\lambda_1(\mathbf{v}).\mathbf{r}_1(\mathbf{v}) = \nabla\lambda_2(\mathbf{v}).\mathbf{r}_2(\mathbf{v}) = \frac{3}{2}\sqrt{gh} \neq 0, \text{ and } \nabla\lambda_3(\mathbf{v}).\mathbf{r}_3(\mathbf{v}) = 0 \tag{11}$$

A very important parameter for the SWE is the Froude number $\text{Fr} = \frac{u}{c}$, particularly for a free surface flow. The flow is said to be subcritical if $\text{Fr} < 1$, critical if $\text{Fr} = 1$, and supercritical if $\text{Fr} > 1$. The critical curves are rewritten as follows:

$$C^+ := \{q = h\sqrt{gh}\}, \quad C^- := \{q = -h\sqrt{gh}\} \tag{12}$$

Due to the condition given in Equation (11) that leads to the coincidence of the characteristic fields, the SWE system loses its hyperbolicity and therefore the

system (3) is not a strictly hyperbolic system, for more details, we recommend the work of [22] which provides a fair explanation of the role of hyperbolicity for the SWE system and how it can be beneficial for both analytical and numerical treatments of such a system. Under the subcritical flow conditions, we can see that the SWE system is always strictly hyperbolic and that the theory of hyperbolic systems can be applied thereto. In other words, the strict hyperbolicity is not connected if we consider all ranges of the flow (subcritical, transitional, and supercritical) and therefore the Riemann problem becomes more delicate to solve. Indeed, enforcing the subcritical condition allows establishing the solution of the Riemann problem and it is proved later on. In natural channel networks, the Froude number Fr is generally small, therefore, considering the Fr number smaller than 1 (*i.e.* subcritical) only will not limit the practical utility of our analysis. For this motivation, we restrict ourselves to the subcritical flow conditions for the rest of the thesis. This restriction is mandatory for the development of the junction Riemann problem theory in the next Chapter. Figure 5 shows the critical curves parameterized as a function of the water depth where the area between the two curves refers to the subcritical flow and the shadow areas above the right critical curve and below the left curve refer to the supercritical flow. Along the critical curves the SWE lose their hyperbolicity [22].
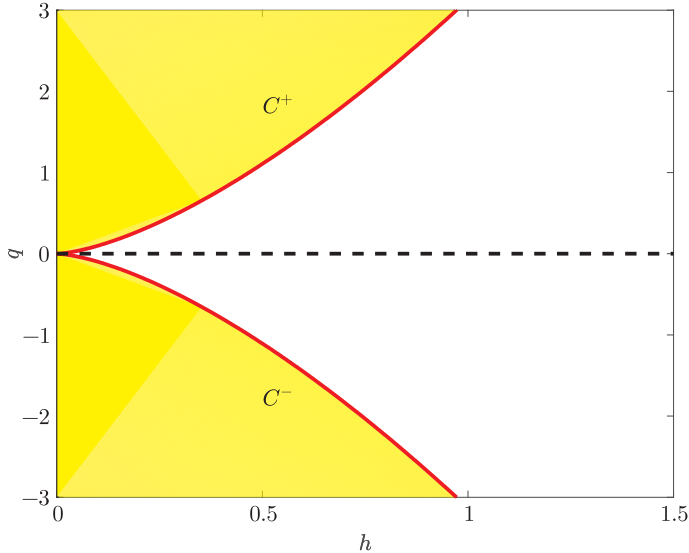

Figure 5. Left and right critical curves

2.3. Loci and integral curves

In this Section we define the wave curves that will be used to give the Riemann solution later on. Giving a constant left state $\mathbf{v}_o = (h_o, q_o, z_o)$, the system (1) has two elementary waves (shock waves and rarefaction waves) such that the shock curves consist of all right hand states $\mathbf{v} = (h, q, z)$ that can be

connected to the left states by shock waves. Indeed, system (1) implies that the left and the right states are connected by the Rankine-Hugoniot relations [17]. Thus, by applying the Rankine-Hugoniot relation to the SWE system (3) we have

$$
\begin{cases}
-\mathsf{S}\left[h-h_o\right]+\left[hu-h_o u_o\right]=0 & (13) \\
-\mathsf{S}\left[hu-h_o u_o\right]+\left[\left(hu^2+\dfrac{gh^2}{2}\right)-\left(h_o u_o^2+\dfrac{gh_o^2}{2}\right)\right]=0 & (14)
\end{cases}
$$

where S are the shock speeds. A straightforward calculation from system $(13)-(14)$ leads to the Hugoniot curves parameterized as a function in the water depth h. Starting by changing the reference frame such that

$$
\hat{u}=u-\mathsf{S}\Longrightarrow h\hat{u}=hu-h\mathsf{S}\Longrightarrow \hat{q}=q-h\mathsf{S} \tag{15}
$$

and

$$
\hat{u}_o=u_o-\mathsf{S}\Longrightarrow h_o\hat{u}_o=h_o u_o-h_o\mathsf{S}\Longrightarrow \hat{q}_o=q_o-h_o\mathsf{S} \tag{16}
$$

From Equations (13), (15), and (16) we get

$$
\hat{q}=\hat{q}_o\Longrightarrow h\hat{u}=h_o\hat{u}_o \tag{17}
$$

Plugging Equations (15), (16), and (17) into Equation (14) we get

$$
q=q_o+(h-h_o)\left[\frac{q_o}{h_o}\pm\sqrt{\frac{gh(h+h_o)}{2h_o}}\right] \tag{18}
$$

which is associated to the first and the second characteristic fields. Furthermore, the following holds along the Hugoniot curves

$$
\begin{aligned}
\frac{dq}{dh}&=\frac{q_o}{h_o}\pm\sqrt{\frac{g}{2}}\left(\sqrt{\frac{h(h+h_o)}{h_o}}+(h-h_o)\frac{2\left(2h+h_o\right)}{\sqrt{\frac{h(h+h_o)}{h_o}}}\right)\\
&\longrightarrow\frac{q_o}{h_o}\pm\sqrt{gh_o}\text{ as }h\to h_o
\end{aligned} \tag{19}
$$

The shock speeds along the Hugoniot curves are given by

$$
\mathsf{S}=\frac{q_o}{h_o}\pm\sqrt{\frac{gh}{2}\left(\frac{h+h_o}{h_o}\right)} \tag{20}
$$

The shock speeds are required to satisfy the Lax shock inequalities or, in other words, the entropy conditions [17] such that the following inequality is true

$$
\lambda_{1,2}(\mathbf{v})<S(\mathbf{v}_o,\mathbf{v})<\lambda_{1,2}(\mathbf{v}_o) \tag{21}
$$

Taking into account the Hugoniot curves and the lax entropy condition, the first shock curve $\mathcal{S}_1(\mathbf{v}_o,\mathbf{v})$ associated to the first characteristic fields and initiated from

the left-hand state $\mathbf{v}_o$ consisting of all right-hand states $\mathbf{v}$ which may connect to $\mathbf{v}_o$ by the Lax shock, is

$$\mathcal{S}_1(\mathbf{v}): \quad q = q_1(h, \mathbf{v_o}) = q_o + (h - h_o)\left[\frac{q_o}{h_o} - \sqrt{\frac{gh(h + h_o)}{2h_o}}\right], \quad h > h_o \qquad (22)$$

Similarly, the second shock curve $\mathcal{S}_2(\mathbf{v}_o, \mathbf{v})$ associated to the second characteristic field, initiated from the left-hand state $\mathbf{v}_o$ and that may connect to the whole right hand state $\mathbf{v}$ through the Lax shock, is

$$\mathcal{S}_2(\mathbf{v}): \quad q = q_2(h, \mathbf{v_o}) = q_o + (h - h_o)\left[\frac{q_o}{h_o} + \sqrt{\frac{gh(h + h_o)}{2h_o}}\right], \quad h < h_o \qquad (23)$$

We might also define the backward shocks similarly in view of the Lax inequalities. The first backward shock curve $\mathcal{S}_1^{\mathcal{B}}$ associated to the first characteristic field, initiated from the right-hand state $\mathbf{v}_o$ that may connect to all left-hand state $\mathbf{v}$ through Lax shock, is

$$\mathcal{S}_1^{\mathcal{B}}(\mathbf{v}): \quad q = q_1(h, \mathbf{v_o}) = q_o - (h - h_o)\left[\frac{q_o}{h_o} - \sqrt{\frac{gh(h + h_o)}{2h_o}}\right], \quad h < h_o \qquad (24)$$

Similarly, the second back shock curve $\mathcal{S}_2^{\mathcal{B}}(\mathbf{v}_o, \mathbf{v})$ associated to the second characteristic field, initiated from the right-hand state $\mathbf{v}_o$ and that may connect to all left-hand state $\mathbf{v}$ through the Lax shock, is

$$\mathcal{S}_2^{\mathcal{B}}(\mathbf{v}): \quad q = q_2(h, \mathbf{v_o}) = q_o + (h - h_o)\left[\frac{q_o}{h_o} - \sqrt{\frac{gh(h + h_o)}{2h_o}}\right], \quad h > h_o \qquad (25)$$

As for the rarefaction waves, the Riemann invariants are used to derive the mathematical formulas of the rarefaction waves. The rarefaction waves satisfy the following ordinary differential equations:

$$\frac{d\mathbf{v}}{d\zeta} = \frac{r_i(\mathbf{v})}{\nabla\lambda_i(\mathbf{v}).r_i(\mathbf{v})}, \quad \zeta = \frac{x}{t}, \quad i = 1, 2 \qquad (26)$$

For the family of waves associated to the first characteristic $\lambda_1 = u - c$, we get

$$\frac{dh(\zeta)}{d\zeta} = -\frac{2}{3}\frac{\sqrt{h(\zeta)}}{\sqrt{g}} \qquad (27)$$

$$\frac{dq(\zeta)}{d\zeta} = -\frac{2}{3}\frac{\left(\frac{q(\zeta)}{h(\zeta)} - \sqrt{gh(\zeta)}\right)}{\sqrt{\frac{g}{h(\zeta)}}} \qquad (28)$$

$$\frac{dz(\zeta)}{d\zeta} = 0 \qquad (29)$$

While combining Equations (27) and (28) leads to

$$\frac{dq}{dh} = \frac{q}{h} - \sqrt{gh} \tag{30}$$

If we integrate Equation (30), then the integral curve passing through the initial state $\mathbf{v} = (h_o, q_o, z_o)$, is given by

$$q = h\left(\frac{q_o}{h_o} \mp 2\left(\sqrt{gh} - \sqrt{gh_o}\right)\right) \tag{31}$$

Across the rarefaction fan the characteristic speed should be increased and the following relation must be satisfied

$$\lambda_{1,2}(\mathbf{v}) \geq \lambda_{1,2}(\mathbf{v}_o) \tag{32}$$

Furthermore, the first rarefaction curve $\mathcal{R}_1(\mathbf{v}_o)$ associated to the first characteristic field, initiated from a given left-hand state, and consisting of all right-hand states $\mathbf{v}$ that may connect to the state $\mathbf{v}$ through a rarefaction wave, is

$$\mathcal{R}_1(\mathbf{v}_o): \quad q = q_1(h, \mathbf{v_o}) = h\left(\frac{q_o}{h_o} - 2\left(\sqrt{gh} - \sqrt{gh_o}\right)\right), \quad h \leq h_o \tag{33}$$

Similarly, the second rarefaction curve $\mathcal{R}_2(\mathbf{v}_o)$ associated to the second characteristic field, initiated from a given left-hand state, and consisting of all right-hand states $\mathbf{v}$ that may connect to the state $\mathbf{v}$ through a rarefaction wave, is

$$\mathcal{R}_2(\mathbf{v}_o): \quad q = q_2(h, \mathbf{v_o}) = h\left(\frac{q_o}{h_o} - +2\left(\sqrt{gh} - \sqrt{gh_o}\right)\right), \quad h \geq h_o \tag{34}$$

Thus, the backward rarefaction curves can be defined as follows: the first backward rarefaction curve $\mathcal{R}_1^{\mathcal{B}}(\mathbf{v})$ associated to the first characteristic field, initiated from a given right-hand state $\mathbf{v}_o$, consisting of all left-hand states $\mathbf{v}$ that may connect to the state $\mathbf{v}_o$ through a rarefaction wave, is

$$\mathcal{R}_1^{\mathcal{B}}(\mathbf{v}_o): \quad q = q_1(h, \mathbf{v_o}) = h\left(\frac{q_o}{h_o} - 2\left(\sqrt{gh} - \sqrt{gh_o}\right)\right), \quad h \geq h_o \tag{35}$$

Therefore, the second backward rarefaction curve $\mathcal{R}_2^{\mathcal{B}}(\mathbf{v})$ associated to the second characteristic field, initiated from a given right-hand state $\mathbf{v}_o$, consisting of all left-hand states $\mathbf{v}$ that may connect to the state $\mathbf{v}_o$ through a rarefaction wave, is

$$\mathcal{R}_2^{\mathcal{B}}(\mathbf{v}_o): \quad q = q_2(h, \mathbf{v_o}) = h\left(\frac{q_o}{h_o} - +2\left(\sqrt{gh} - \sqrt{gh_o}\right)\right), \quad h \leq h_o \tag{36}$$

Finally, by combining the first shock curve and the first rarefaction curve, we obtain the first locus curve that is associated to the first characteristic field, referenced by the left locus curve and which is therefore given by $\tau_l(\mathbf{v}_o) := (h, \xi_l(h)) = \mathcal{S}_1(\mathbf{v}_o) \cup \mathcal{R}_1(\mathbf{v}_o)$ such that

$$\xi_l(h) = \begin{cases} q_o + (h - h_o)\left[\frac{q_o}{h_o} - \sqrt{\frac{gh(h+h_o)}{2h_o}}\right], & h > h_o \\ h\left(\frac{q_o}{h_o} - 2\left(\sqrt{gh} - \sqrt{gh_o}\right)\right), & h \leq h_o \end{cases} \tag{37}$$

Combining the second shock curve and the second rarefaction curve, we obtain the second locus curve. The locus curve is associated to the second characteristic

field. It is referenced by the right locus curve and therefore it is given by $\tau_r(\mathbf{v}_o) := (h, \xi_r(h)) = \mathcal{S}_2(\mathbf{v}_o) \cup \mathcal{R}_2(\mathbf{v}_o)$ such that

$$
\xi_r(h) = \begin{cases} q_o + (h - h_o)\left[\dfrac{q_o}{h_o} + \sqrt{\dfrac{gh(h+h_o)}{2h_o}}\right], & h < h_o \\ h\left(\dfrac{q_o}{h_o} + 2\left(\sqrt{gh} - \sqrt{gh_o}\right)\right), & h \geq h_o \end{cases} \tag{38}
$$

Figure 6 shows the configuration of the loci curves. The solid line portions refer to the shock curves and the dot-line portions refer to the rarefaction curves. Taking into account the wave curves and the given constant initial states $\mathbf{v}_o$, we are analytically and geometrically able to sketch the Riemann solution. Furthermore, the Riemann solution is discussed in more details in the next Section.
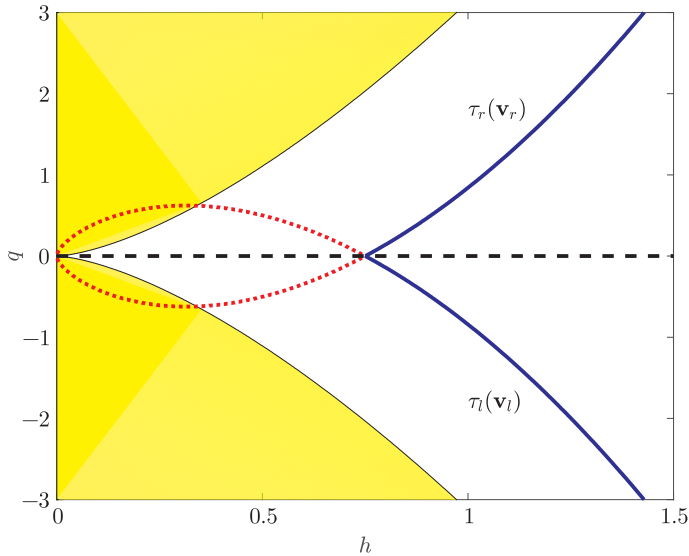

Figure 6. Left and right loci curves

2.4. Classical Riemann problem

In this Section we highlight the classical Riemann problem of the 1D-SWE and its solution in a single open channel. The bed is considered to be flat. As for the case of the bottom discontinuity in a single channel, a brief description of the solution in the spirit of [3] is given. For simplicity in this Section, the standard Riemann solution is derived for the flat bed case only. The Riemann solution is given in both analytical expression and geometric configurations. Assuming a constant bottom elevation in a single channel, the system (3) can be used to define the standard Riemann problem for a single open channel flow. We consider the following initial piecewise constant states

$$
\mathbf{v}_o := \mathbf{v}(0, x) = \begin{cases} \mathbf{v}_l & \text{if } x < 0, \quad x \in \mathbb{R} \\ \mathbf{v}_r & \text{if } x > 0 \quad x \in \mathbb{R} \end{cases} \tag{39}
$$

where $\mathbf{v}_l$ and $\mathbf{v}_r$ are the left and right initial states, respectively. In the subcritical conditions, the solution consists of two unperturbed states and an intermediate state separated by left and right waves [22]. The intermediate state is connected to the left unperturbed state through a shock wave or a rarefaction wave, and is connected to the right unperturbed state through a shock wave or a rarefaction wave. Therefore, the intermediate states are defined by using the Shock curves and the Riemann integral curves as it is shown in Section 2.3. For a clear picture of the Riemann solution of system (3)–(39), we start introducing the following useful Lemmas.

2.4.1. Lemma

Considering the subcritical flow conditions, the only portion of the left loci curve $\tau_l(\mathbf{v}_l)$ that intersect with the right critical curve C^+ is the rarefaction portion. This intersection denoted by $\mathbf{v}_o^{lm}$, is characterized by the maximum of ξ_l and is given by

$$h_o^{lm} = \frac{1}{g}\left(\frac{q_l}{3h_l} + \frac{2}{3}\sqrt{gh_l}\right)^2 \tag{40}$$

$$q_o^{lm} = \xi_l(h_o^{lm}) = h_o^{lm}\sqrt{gh_o^{lm}} \tag{41}$$

Moreover, $\tau_l(\mathbf{v}_l)$ is given by a concave function that is increasing in the interval $]0, h_o^{lm}]$ and decreasing in the interval $[h_o^{lm}, +\infty[$. Therefore, the increasing part of the function varies from

$$\lim_{h_o \to 0^+} \xi_l(h_o) = 0 \quad \text{to} \quad \xi_l(h_o^{lm}) = h_o^{lm}\sqrt{gh_o^{lm}} \tag{42}$$

and the decreasing part varies from

$$\xi_l(h_o^{lm}) = h_o^{lm}\sqrt{gh_o^{lm}} \quad \text{to} \lim_{h_o \to +\infty} \xi_l(h_o) = -\infty \tag{43}$$

Proof

Starting from the shock portion of the left (first) locus curve $\tau_l(\mathbf{v}_l)$ *i.e.*, $\mathcal{S}_l(\mathbf{v}_l)$ that intersects with the right (the positive) critical curve C^+ and given the left constant state $\mathbf{v}_l$, then according to the definition of the right critical curve in Equation (8), the following equalities are true

$$q_l = h_l\sqrt{gh_l}, \text{and } q_o = h_o\sqrt{gh_o} \tag{44}$$

From the shock curve in Equation (22) we have

$$q_o = q_l + (h_o - h_l)\left[\frac{q_l}{h_l} - \sqrt{\frac{gh_o(h_o + h_l)}{2h_l}}\right], \quad h_o > h_l \tag{45}$$

Assuming the left shock portion intersects with the right critical curve, therefore from Equations (44) and (45) we have

$$h_o\sqrt{gh_o} = q_l + (h_o - h_l)\left[\frac{q_l}{h_l} - \sqrt{\frac{gh_o(h_o + h_l)}{2h_l}}\right] \tag{46}$$
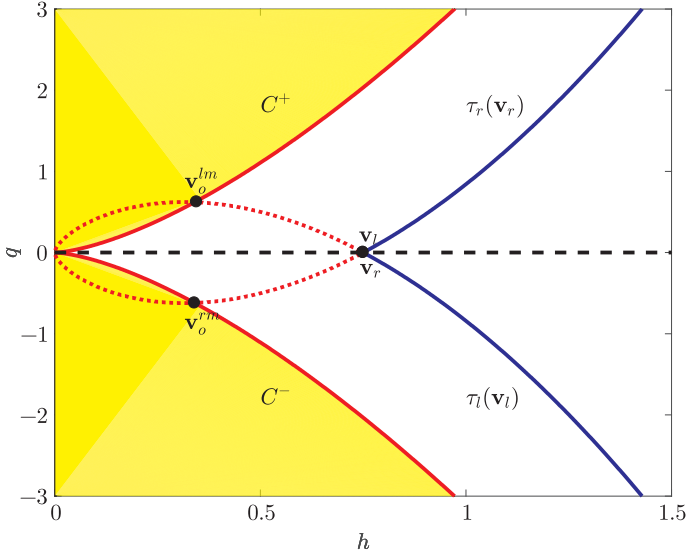
Figure 7. Intersection of loci curves with critical curves at minimum and maximum of loci functions for constant initial states

This implies that $\frac{q_l}{h_l} - \sqrt{gh_o} > 0$.

In fact, this is not true since $h_o > h_l$ implies $\frac{q_l}{h_l} - \sqrt{gh_o} < \frac{q_l}{h_l} - \sqrt{gh_l} < 0$

By contradiction the left shock portion cannot intersect with the right critical curve.

Starting from the left rarefaction portion of the left locus curve $\tau_l(\mathbf{v}_l)$ that may intersect with the left critical curve C^+ we get

$$h_o\sqrt{gh_o} = h_o\left(\frac{q_l}{h_l} - 2\left(\sqrt{gh_o} - \sqrt{gh_l}\right)\right), \quad h_o \leq h_l \tag{47}$$

that is simplified to

$$\sqrt{gh_o} = \frac{q_l}{h_l} - 2\sqrt{gh_o} + 2\sqrt{gh_l} \tag{48}$$

and implies

$$\frac{q_l}{h_l} - \sqrt{gh_l} < \frac{q_l}{h_l} - \sqrt{gh_o} < 0; \, h_o \leq h_l \tag{49}$$

Indeed, the only admissible intersection between the left locus curve and the left critical curve is only through the left rarefaction portion curve. To prove that the intersection point is the maximum of the left locus function, we rewrite Equation (48) in the following form

$$\sqrt{gh_o^{lm}} = \frac{q_l}{h_l} - 2\sqrt{gh_o^{lm}} + 2\sqrt{gh_l} \tag{50}$$

Arranging Equation (50) somewhat and squaring it, we have

$$h_o^{lm} = \frac{1}{g}\left(\frac{q_l}{3h_l} + \frac{2}{3}\sqrt{gh_l}\right)^2 \tag{51}$$

where h_o^{lm} is the first component of the state $\mathbf{v}_o^{lm}$ and therefore the corresponding discharge state q_o^{lm} is given by

$$q_o^{lm} = h_o^{lm}\sqrt{gh_o^{lm}} \tag{52}$$

Equations (51) and (52) claim the rightness of Equations (40) and (41). To verify the concavity and the decreasing-increasing intervals given in Equations (42) and (43), we start from the left rarefaction Equation (37) and Equations (50) to obtain

$$\left.\frac{d\xi_l(h_o)}{dh_o}\right|_{h_o=h_o^{lm}} = \frac{q_l}{h_l} + 2\sqrt{gh_l} - 3\sqrt{gh_o^{lm}}\bigg|_{h_o=h_o^{lm}} = 0 \tag{53}$$

The second derivative gives

$$\left.\frac{d^2\xi_l(h_o)}{dh_o^2}\right|_{h_o=h_o^{lm}} = -\frac{3g}{2\sqrt{gh_o}}\bigg|_{h_o=h_o^{lm}} < 0, \quad \forall \quad h_o > 0 \tag{54}$$

The increasing and decreasing parts of the concave function are rather claimed as given in Equations (42) and (43). This ends the proof of Lemma 2.4.1. ∎

Thus, for any state $\mathbf{v}_o$ such that $h_o < h_o^{lm}$, the flow becomes supercritical and we have

$$q_o > h_o\sqrt{gh_o} \tag{55}$$

The latter statement can be proved as follows. Considering the rarefaction portion of the first locus curve

$$\xi_l(h_o) = \frac{q_l}{h_l} + 2\sqrt{gh_l} - 2\sqrt{gh_o} \tag{56}$$

From Lemma 2.4.1

$$h_o^{lm} = \frac{1}{g}\left(\frac{1}{3}\frac{q_l}{h_l} + \frac{2}{3}\sqrt{gh_l}\right)^2 \tag{57}$$

Combine Equations (56) and (57) we get

$$\begin{aligned}
\xi_l(h_o) &= h_o\left(3\sqrt{gh_o^{lm}} - 2\sqrt{gh_o}\right) \\
&\geq h_o\left(3\sqrt{gh_o^{lm}} - 2\sqrt{gh_o^{lm}}\right), \quad \text{since } h_o \leq h_o^{lm} \\
&\geq h_o\sqrt{gh_o^{lm}} \\
&\geq h_o\sqrt{gh_o^{lm}}, \quad \text{as } h_o \leq h_o^{lm}
\end{aligned} \tag{58}$$

This gives the transcritical flow conditions such that the Froude number $\text{Fr} > 1$ gives the supercritical flow condition and $\text{Fr} = 1$ gives the critical flow condition.

2.4.2. Lemma

Considering the subcritical flow conditions, the only portion of the right loci curve $\tau_r(\mathbf{v}_r)$ that intersects with the left critical curve C^- is the rarefaction

portion. This intersection denoted by $\mathbf{v}_o^{rm}$ is characterized by the minimum of ξ_r and is given by

$$h_o^{rm} = \frac{1}{g}\left(-\frac{q_l}{3h_l} + \frac{2}{3}\sqrt{gh_l}\right)^2 \tag{59}$$

$$q_o^{rm} = \xi_r(h_o^{rm}) = -h_o^{rm}\sqrt{gh_o^{rm}} \tag{60}$$

Moreover, $\tau_r(v_r)$ is given by a convex function that is decreasing in the interval $]0,h_o^{rm}]$ and increasing in the interval $[h_o^{rm},+\infty[$. Therefore, the deceasing part of the function varies from

$$\lim_{h_o\to 0^+}\xi_r(h_o) = 0 \quad \text{to} \quad \xi_r(h_o^{lm}) = -h_o^{rm}\sqrt{gh_o^{rm}} \tag{61}$$

and the increasing part varies from

$$\xi_r(h_o^{rm}) = -h_o^{rm}\sqrt{gh_o^{rm}} \quad \text{to} \lim_{h_o\to+\infty}\xi_r(h_o) = +\infty \tag{62}$$

Proof

Following the same steps performed as in proof of Lemma 2.4.1 where it is rather the right instead of the left locus curve that is considered and starting from the right shock portion of the right locus curve $\tau_r(h_o,\mathbf{v}_r)$ and trying to intersect it with the right critical curve C^-, we get

$$-h_o\sqrt{gh_o} = h_o\frac{q_r}{h_r} + (h_o - h_r)\left[\sqrt{\frac{gh_o(h_o+h_r)}{2h_r}}\right], \quad h_o > h_r \tag{63}$$

which implies

$$\frac{q_r}{h_r} + \sqrt{gh_o} < 0 \tag{64}$$

and consequently

$$\frac{q_r}{h_r} + \sqrt{gh_o} < \frac{q_r}{h_r} + \sqrt{gh_r} < 0, \quad \text{since } h_o > h_r \tag{65}$$

This is not possible since the right locus is associated with the second characteristic field, which is the opposite of Equation (65). Therefore, the right shock portion cannot intersect with the left critical curve.

Now, we stay again with the fact that the right rarefaction portion is the only option to intersect with the left critical curve such that

$$-h_o\sqrt{gh_o} = h_o\left(\frac{q_r}{h_l} - 2\left(\sqrt{gh_r} - \sqrt{gh_o}\right)\right), \quad h_o \leq h_r \tag{66}$$

By considering the component h_o^{rm}, we have

$$-\sqrt{gh_o^{rm}} = \frac{q_r}{h_l} - 2\sqrt{gh_r} + 2\sqrt{gh_o^{rm}} \tag{67}$$

and therefore

$$h_o^{rm} = \frac{1}{g}\left(-\frac{1}{3}\frac{q_r}{h_l} + \frac{2}{3}\sqrt{gh_r}\right)^2, \quad q_o^{rm} = \tau_r(h_o^{rm}) = -h_o^{rm}\sqrt{gh_o^{rm}} \tag{68}$$

Applying the first derivative, we confirm that the component h_o^{rm} is the maximum point of the right locus curve

$$\frac{d\xi_r(h_o)}{dh_o}\bigg|_{h_o=h_o^{rm}} = \frac{q_r}{h_r} - 2\sqrt{gh_r} + 3\sqrt{gh_o^{rm}}\bigg|_{h_o=h_o^{rm}} = 0 \tag{69}$$

The convexity is followed by the second derivative such that

$$\frac{d^2\xi_r(h_o)}{dh_o^2}\bigg|_{h_o=h_o^{rm}} = \frac{3g}{2\sqrt{gh_o}}\bigg|_{h_o=h_o^{rm}} > 0, \quad \forall \quad h_o > 0 \tag{70}$$

Moreover, the decreasing and increasing parts of the right locus curve are claimed through the definition of the left critical curve and the previous findings. The proof of Lemma 2.4.2 ends here. ■

It is worth mentioning that for any states v_o such that $h_o < h_o^{rm}$ we have

$$q_o \geq h_o\sqrt{gh_o} \tag{71}$$

This implies that the states v_o are supercritical states if $h_o < h_o^{rm}$. The proof of this statement is as follows.

Considering the rarefaction portion of the second locus curve

$$\xi_r(h_o) = \frac{q_r}{h_r} + 2\sqrt{gh_o} - 2\sqrt{gh_r} \tag{72}$$

From Lemma 2.4.2

$$h_o^{rm} = \frac{1}{g}\left(-\frac{1}{3}\frac{q_r}{h_r} + \frac{2}{3}\sqrt{gh_r}\right)^2 \tag{73}$$

Combine Equations (72) and (73) we get

$$\begin{aligned}
\xi_r(h_o) &= -h_o\left(2\sqrt{gh_o} - 3\sqrt{gh_o^{rm}}\right) \\
&\geq h_o\left(3\sqrt{gh_o^{rm}} - 2\sqrt{gh_o^{rm}}\right), \quad \text{since } h_o \leq h_o^{rm} \\
&\geq h_o\sqrt{gh_o^{rm}} \\
&\geq h_o\sqrt{gh_o^{rm}}, \quad \text{as } h_o \leq h_o^{rm}
\end{aligned} \tag{74}$$

Therefore the state $\mathbf{v}_o = (h_o, q_o)$ is a supercritical state if $\text{Fr} > 1$ and is a critical state if $\text{Fr} = 1$.

Lemma 2.4.1 and Lemma 2.4.2 show that the loci curves τ_l and τ_r intersect at a single point only which gives the intermediate states $\mathbf{v}_* = \tau_l \cap \tau_r$ in the Riemann solution. Therefore, the component (h_*, q_*) can be computed by solving the following function, using a nonlinear solver

$$\xi(h) \equiv \xi_l(h) - \xi_r(h) = 0 \tag{75}$$

2.4.3. Treatment of bottom discontinuity

In [3] the stationary step transition (SST) over the bottom discontinuity is defined. The conservation of mass and energy (Total head) is used to determine the unknown states of the solution over the step. In [3], an almost ideal step is considered, such that no energy loss is counted and it is forbidden for the flow to

change the state over the step, *i.e.*, no change of the flow nature from subcritical to supercritical and vice versa. This leads to the Riemann solution. The Riemann solution consists of three states. The first and the third state are computed in accordance with the previous Lemmas. The second state is computed according to the SST methodology which is presented in [3], based on the conservation of the energy and mass. Therefore, the Riemann solution in the presence of the bottom discontinuities consists of shock or rarefaction waves that are connected to the unperturbed states. The unperturbed states can be connected through a contact wave satisfying the SST. Further mathematical investigations [4] have led to defining the involved waves in the Riemann solution. Starting from the given state (h_o, q_o, z_o), there are three admissible waves for the system (3): the rarefaction wave and the shock wave, and the stationary wave with zero velocity. This has been defined as the contact wave by [3]. The stationary wave is supposed to satisfy the Rankine-Hugoniot relations associated with the system (3), but with zero speed. In other words, the mass and the energy are conservative over the discontinuity of the bottom. Therefore, the shock and rarefaction waves are something that is defined in the previous Subsection. It remains only to give more details on the stationary waves. As stated by [4], there are two possible stationary jumps. This is due to the function that is derived directly from the energy conservation concept over the bottom discontinuity as shown in the following

$$
\begin{aligned}
u &= \frac{h_o u_o}{h} \\
z + h + \frac{u^2}{2g} &= z + h_o + \frac{u_o^2}{2g}
\end{aligned}
\tag{76}
$$

System (76) leads to the following one parameter function

$$
\Phi(h) := h^3 + (\Delta z - h_o - \frac{q_o^2}{2g})h^2 + \frac{q_o^2}{2g}
\tag{77}
$$

According to [23], the function Φ admits two physical roots corresponding to the subcritical and supercritical flow states, respectively. This is equivalent to the possible stationary jumps stated in [4]. The researchers use the convexity of the function to declare the admissibility condition for the stationary wave. Therefore, the mass and energy conservation concept over the bottom discontinuity will ensure the well posed Riemann problem of the SWE in a single channel. In the next Chapter, we will discover the use of such information to establish the Riemann solution at junction networks.

For more clarification, numerical examples of the standard Riemann solution are given in the next Section to justify the previous methodology.

2.5. Numerical examples

Here, we present a numerical example that gives the states of the Riemann solution in both geometrical and numerical frameworks.

2.5.1. Example

Consider the Riemann problem (3) together with the following initial conditions

$$\mathbf{v}_l = \begin{bmatrix} 2 \\ 0 \\ 0 \end{bmatrix}, \quad \mathbf{v}_r = \begin{bmatrix} 1 \\ 0 \\ 0 \end{bmatrix} \tag{78}$$

We have $h_l > h_r$ and $q_l = q_r$, this Riemann problem analogues to the dam break problem [14].

Figure 8 shows a geometric picture of the Riemann solution with the initial conditions given by Equation (78). The Riemann solution consists of two ongoing waves. The first is a rarefaction wave that connects the unperturbed left state $\mathbf{v}_l$ to the perturbed state $\mathbf{v}_*$. The second is a shock wave that connects the unperturbed right state $\mathbf{v}_l$ to the perturbed state $\mathbf{v}_*$. Furthermore, Figure 9 shows the time evolution of the Riemann solution, where the dashed-lines refer to the initial states at the zero time which is located at zero in the space domain $[-1,1]$. It is obvious that the Riemann solution is given by the solid-lines. Two waves are seen (*i.e.*, shock and rarefaction waves).
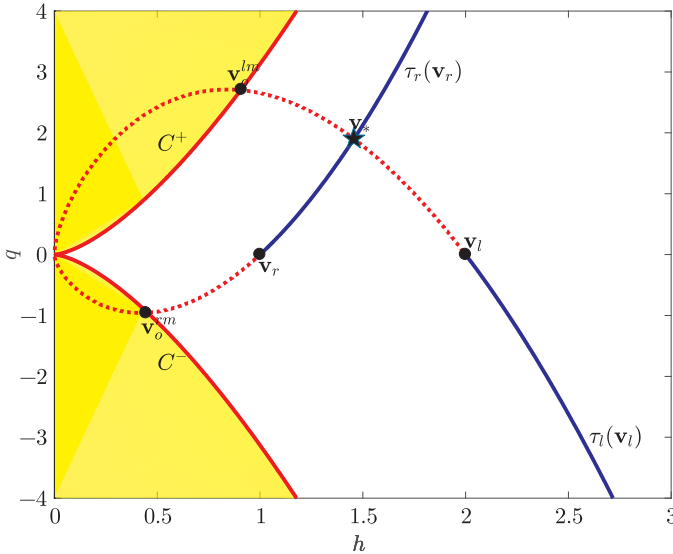

Figure 8. Standard Riemann solution in phase plane of Example 2.5.1

2.6. Summary of Chapter 2

In this Chapter we set up some useful tools that are used in what follows to establish the overall aim of the paper. Critical curves *i.e.*, right and left, are shown to distinguish the flow nature. The flow is critical along the critical curves, *i.e.* Fr = 1. There are areas where the flow is supercritical above the right critical curve and below the left critical curve, *i.e.* Fr > 1. The flow is subcritical in between the critical curves, *i.e.* Fr < 1. The loci curves have
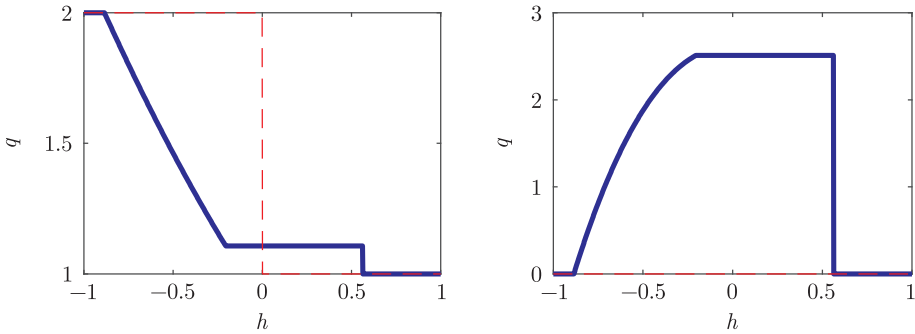
Figure 9. Discharge and water depth profiles of Riemann solution in phase plane of Example 2.5.1 at time $t = 0.2$s

been introduced to combine the possible wave pattern of the Riemann solution. The only admissible waves under subcritical flow conditions that can intersect with the critical curves are the rarefaction waves starting from the maximum and the minimum of the left locus and the right locus, respectively. These tools are mathematically proved. Therefore, the standard Riemann solution is shown in both the analytical expression and the geometrical configuration. The Riemann solution of the 1D-SWE in a single channel is a self-similar solution that is composed of two ongoing waves. These ongoing waves are the shock and rarefaction waves. The entropy condition must be satisfied across the shock wave. This condition contributes to selecting the right shock wave. A well known fact about the shock wave is the dissipation of energy. The standard Riemann solution is geometrically obtained through the intersection between the loci curves. The states at the intersection are the intermediate states in the Riemann solution. These states are connected to the unperturbed states through either the shock wave or the rarefaction wave. For justification, the Riemann solution is also illustrated by a numerical example. Thus, the Riemann solution is briefly given for the case with a channel bottom discontinuity. However, deep investigations about the bottom discontinuity are referenced back to the literature.

3. Junction Riemann problem

3.1. Introduction

In the recent years, mathematical models for network flows constituted by partial differential equations (PDEs) are well defined (*e.g.*, well posedness, existence, and uniqueness), see [24–26] for general systems, [27] for applications in gas dynamics, [28] for applications in traffic flows, and [29] for applications in open channel networks. These applications can be of great benefit for the mathematical development. Typical examples of real applications are free surface flows in irrigation systems or natural rivers [13, 30], traffic flows [28], and blood flows [31]. Particularly, the open channel flow in networks is of great interest from the environmental-hydraulic prospective. The simplest configuration of channel networks is the star network. The star network comprises three identical rectangular chan-

nels combined together at what is the so-called junction node. The junction node is an internal node generated by an intersection channels. Realistic conditions are fundamentally crucial for computational reasons to connect the fluid at the junction in order to characterize the water flow at the junction node in channel networks.

We can see from the literature such as [15, 3, 32, 4, 14] that the one-dimensional (1D) shallow water equations (SWE) are well established for simulation of an open channel flow in a single open channel, where the flow is either subcritical or supercritical. Thus, the bottom topography is continuous or discontinuous. However, using the SWE in open channel networks is not an easy task because the SWE become singular [33] at the junction node. Hereafter, performing 1D numerical simulations in channel networks requires the internal boundary conditions. Those conditions are defined as functions which depend on the SWE solution to provide a connection of the channels at each junction node.

In almost half a decade, the 1D-SWE are used for simulations of open channel networks, see for example [34, 7, 35, 36]. [34] has used a recursive formula derived from finite elements equations. Relationships in a channel junction are established to provide the internal boundary conditions. Therefore, a system of equations is obtained and numerically solved to provide the junction conditions. Then, the finite element method (FEM) is used to perform numerical simulations. [7] performed simulations of subcritical flows at an open channel junction using the finite volume method (FVM). Researchers evaluate various existing theoretical models. These models are used to provide the internal boundary conditions at the junction. Researchers conclude that all models have almost the same results for a small Froude number $\mathrm{Fr} < 0.35$. Significant differences between the junction models are reported for the Froude number $\mathrm{Fr} > 0.35$. The best results are obtained by the Shabayek model [12]. It is classified as a momentum based model. [35] have investigated the behavior of 1D and 2D simulations of a channel junction. In both cases the approximated Saint-Venant equations coupled with the junction model were used to perform the simulations. A second-order FVMw is used to discretize the equations. The Shabayek model [12] is used to provide the inner boundary conditions at the junction for the 1D simulation. [35] conclude that the 2D simulations match the experimental data better than the 1D simulations. This finding was due to the 3D nature of such phenomena (*i.e.*, the junction flow). It is worth mentioning that the study was limited to the subcritical flows. Then, [36] obtain the same results for transcritical and supercritical flows. Furthermore, [36] use the Rice model [37] to supply the junction conditions for the 1D simulations. However, junction models have been used without any further mathematical investigations (*e.g.*, existence and uniqueness) of the generated solutions of such models. Even more, such mathematical analysis is hardly achieved in such a situation due to the empirical nature of these models. To avoid the ill-possedness of the mathematical model in a junction network of three branches as mathematically required, six unknowns (*i.e.*, three water depths and three water

discharges) must be generated at the junction node due to the internal boundary conditions that ensure the flow continuity at the junction. The mathematical model is well posed if the internal boundary conditions are well defined. Indeed, six relationships have to be supplied. These relationships form a system of non-linear equations. Thus, they have to be numerically solved at each time step to provide the internal boundary conditions. Furthermore, for subcritical flows one characteristic field of the SWE is involved at each boundary [7, 36, 38] and therefore three relationships are obtained by using the characteristic curves [39]. The other three relationships are obtained by enforcing the mass, energy, momentum conservations at the junction node [33, 9, 10, 40, 12].

For the supercritical flow [36, 38], two characteristic fields are involved at the inflow boundary, and therefore four relationships are obtained. This is achieved by using the characteristic curves, which is fully explained in [39]. The remaining relationships are obtained by using the mass continuity [33] node and the Rice model [37] or the nonlinear dynamical equation with momentum conservation [41, 42, 6] at the junction.

The junction models are defined based on the previous principles for both subcritical and supercritical flow conditions. The focus is on the subcritical flow conditions, meanwhile the classical junction models are represented by the Equality [9], Gurram [10], Hsu [40], and Shabayek [12] models. Full details about the classical junction models are given in the next section. It is noticed that the classical junction models are extensively developed by engineers without any mathematical analysis that guarantee the existence and uniqueness of the solutions of models.

Motivated by the mathematical weakness of classical junction models and based on mathematical analysis, a recent approach to provide the internal boundary conditions is determined by [29]. [29] have proposed to use the Runge-Kutta discontinuous Galarkian methods to numerically simulate the 1D water flow in channel networks. The internal boundary conditions are provided by defining an extended Riemann problem of the SWE at the junction node. This approach is based on the results obtained by [43] to provide the necessary theoretical findings that guarantee the well-possedness of the Riemann problem at the junction. [43] have built their theoretical analysis of the Riemann problem taking into account the huge amount of literature that was previously developed. Starting from the well-posed evidence of the hyperbolic systems at the junction network as developed by [17, 22, 24, 26, 25] and the recent results of the Riemann solution in a single open channel by [3, 4, 21]: [43] have investigated the existence and uniqueness of the Riemann solution of the water flow in a star network of three identical rectangular channels. The flow is supposed to be subcritical everywhere. However, the results are only promising for a specific network being an identical star network. In reality, nothing is ideal. Therefore, the [43] results open only the door for more investigation of the Riemann problem in channel networks. Hence, the purpose of this section is to extend the results by [43] to include an unconditional network

configuration. In particular, assumptions of symmetry and equality of the channel width are relaxed. Bottom discontinuities between the channels at the junction are also taken into account. Since the majority of water flows in nature are classified to be fluvial (subcritical) flows [44], then, considering only the subcritical flow condition will not limit the application of the Riemann problem in nature. Moreover, the Riemann solution is geometrically given by plotting the intersection points of the loci curves and the junction curves in the phase space. The loci curves are defined in the previous section. The junction curves have been lately defined using the methodology presented in this section. The solution is obtained while physical explanations of each mathematical term are given.

The remaining part of this section is organized as follows: In Section 3.2 we redefine the Riemann problem that describes the SWE at a junction network. The Riemann solution is also given in a theorem. The theorem is validated by a vast set of numerical examples in Section 3.4. Finally, a summary of this section is included in Section 3.5.

3.2. *Nonlinear junction Riemann problem*

The Riemann problem is redefined to consider the water flow in a channel network. Moreover, the Riemann solution is given by the theorem. This theorem includes the solution of the junction Riemann problem in a non-symmetric channel network. The bottom is discontinuous. The presented theorem proved in this section is well suited for both diffluence and confluence networks. However, the analysis will be only present for the diffluence network where one channel splits into two channels as shown in Figure 10. The same results are obtainable for the confluence network by reverse analysis. By considering the channel network shown in Figure 10, the Riemann problem of the 1D-SWE is written in the following subsection.

3.2.1. *The junction Riemann problem*

The junction Riemann problem is given by

$$\begin{cases} \frac{\partial \mathbf{v}_1}{\partial t} + \mathbf{A}(\mathbf{v}_1)\frac{\partial \mathbf{v}_1}{\partial x} = 0, & x < x_j \\ \frac{\partial \mathbf{v}_2}{\partial t} + \mathbf{A}(\mathbf{v}_2)\frac{\partial \mathbf{v}_2}{\partial x} = 0, & x > x_j \\ \frac{\partial \mathbf{v}_3}{\partial t} + \mathbf{A}(\mathbf{v}_3)\frac{\partial \mathbf{v}_3}{\partial x} = 0, & x > x_j \end{cases} \tag{79}$$

where x_j refers to the junction node and $\mathbf{A}(\mathbf{v})$ is the system matrix as defined in Equation (4). Here, the junction Riemann problem is associated with the following initial data:

$$\begin{cases} \mathbf{v}_1(0,x) = \mathbf{v}_{1l}, & x < x_j \\ \mathbf{v}_2(0,x) = \mathbf{v}_{2r}, & x > x_j \\ \mathbf{v}_3(0,x) = \mathbf{v}_{3r}, & x > x_j \end{cases} \tag{80}$$

Indeed, the set of Equations (79)–(80) are locally forming the Riemann problem at the junction node x_j. The Riemann solution is expected to consist of six states denoted by v_{1l}, v_{2r}, v_{3r}, v_{1*}, v_{2*}, and v_{3*}. According to the Riemann solution in
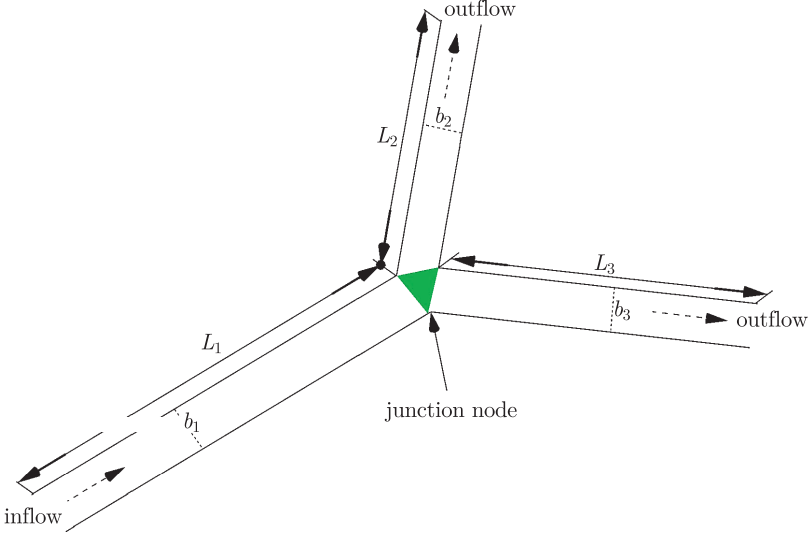
Figure 10. Channel network junction of three non-identical branches

a single channel, we have from the state v_{1l} to the state v_{1*} that the relationship by Equation (22) or Equation (33) is true. From the state v_{2r} to the state v_{2*} and from the state v_{3r} to the state v_{3*}, the relationship by Equation (23) or Equation (34) is true. The states v_{1*}, v_{2*}, and v_{3*} are connected to each other through the mass conservation and the total head balance relationships [23]. The mass conservation and the total head balances at the junction node give

$$q_{1*} = \omega_2 q_{2*} + \omega_3 q_{3*}; \quad q_{2*} = \left(\frac{r}{\omega_2}\right) q_{1*}, \quad q_{3*} = \left(\frac{1-r}{\omega_3}\right) q_{1*}, \quad \text{at } x_j \qquad (81)$$

$$h_{1*} + \frac{q_{1*}^2}{2gh_{1*}^2} = Z_2 + h_{2*} + \frac{q_{2*}^2}{2gh_{2*}^2}, \quad \text{at } x_j \qquad (82)$$

$$h_{1*} + \frac{q_{1*}^2}{2gh_{1*}^2} = Z_3 + h_{3*} + \frac{q_{3*}^2}{2gh_{3*}^2}, \quad \text{at } x_j \qquad (83)$$

where $0 < r = \omega_2 \frac{q_{2*}}{q_{1*}} < 1$ is the discharge ratio. $0 < \omega_2 = \frac{b_2}{b_1}$ and $0 < \omega_3 = \frac{b_3}{b_1}$ are the ratios between the second channel width and the first channel width, the third channel width and the first channel width, respectively. $Z_2 = z_2 - z_1$ and $Z_3 = z_3 - z_1$ are the bottom discontinuities between the first and the second channels, the first and the third channels, respectively. Therefore, for a channel network of three branches forming a single junction, we are possibly having eight admissible waves:

1. If $h_{1*} < h_{1l}$, $h_{2*} < h_{2r}$, and $h_{3*} < h_{3r}$ *i.e.*, the left and right waves are rarefaction waves, then (v_{1*}, v_{2*}, v_{3*}) satisfies Equations (81)–(83) such that $v_{1*} \in R_{1l}$, $v_{2*} \in R_{2r}$, and $v_{3*} \in R_{3r}$.
2. If $h_{1*} > h_{1l}$, $h_{2*} > h_{2r}$, and $h_{3*} > h_{3r}$ *i.e.*, the left and right waves are shock waves, then (v_{1*}, v_{2*}, v_{3*}) satisfies Equations (81)–(83) such that $v_{1*} \in S_{1l}$, $v_{2*} \in S_{2r}$, and $v_{3*} \in S_{3r}$.

3. If $h_{1*} < h_{1l}$, $h_{2*} > h_{2r}$, and $h_{3*} > h_{3r}$ *i.e.*, the left wave is a rarefaction wave and right waves are shock waves, then (v_{1*}, v_{2*}, v_{3*}) satisfies Equations (81)–(83) such that $v_{1*} \in R_{1l}$, $v_{2*} \in S_{2r}$, and $v_{3*} \in S_{3r}$.

4. If $h_{1*} > h_{1l}$, $h_{2*} < h_{2r}$, and $h_{3*} < h_{3r}$ *i.e.*, the left wave is a shock wave and the right waves are rarefaction waves, then (v_{1*}, v_{2*}, v_{3*}) satisfies Equations (81)–(83) such that $v_{1*} \in S_{1l}$, $v_{2*} \in R_{2r}$, and $v_{3*} \in R_{3r}$.

5. If $h_{1*} > h_{1l}$, $h_{2*} > h_{2r}$, and $h_{3*} < h_{3r}$ *i.e.*, the left wave is a shock wave, the first right wave is a shock wave, and the second right wave is a rarefaction wave, then (v_{1*}, v_{2*}, v_{3*}) satisfies Equations (81)–(83) such that $v_{1*} \in S_{1l}$, $v_{2*} \in S_{2r}$, and $v_{3*} \in R_{3r}$.

6. If $h_{1*} > h_{1l}$, $h_{2*} < h_{2r}$, and $h_{3*} > h_{3r}$ *i.e.*, the left wave is a shock wave, the first right wave is a rarefaction wave, and second right wave is a shock wave, then (v_{1*}, v_{2*}, v_{3*}) satisfies Equations (81)–(83)) such that $v_{1*} \in S_{1l}$, $v_{2*} \in R_{2r}$, and $v_{3*} \in S_{3r}$.

7. If $h_{1*} < h_{1l}$, $h_{2*} > h_{2r}$, and $h_{3*} < h_{3r}$ *i.e.*, the left wave is a rarefaction wave, the first right wave is a shock wave, and the second right wave is a rarefaction wave, then (v_{1*}, v_{2*}, v_{3*}) satisfies Equations (81)–(83) such that $v_{1*} \in R_{1l}$, $v_{2*} \in S_{2r}$, and $v_{3*} \in R_{3r}$.

8. If $h_{1*} < h_{1l}$, $h_{2*} < h_{2r}$, and $h_{3*} > h_{3r}$ *i.e.*, the left wave is a rarefaction wave, the first right wave is a rarefaction wave, and second right wave is a shock wave, then (v_{1*}, v_{2*}, v_{3*}) satisfies Equations (81)–(83) such that $v_{1*} \in R_{1l}$, $v_{2*} \in R_{2r}$, and $v_{3*} \in S_{3r}$.

Here, knowing that the admissible shock wave is subject to the fulfillment of the entropy condition and considering the mass conservation, the total head balances at the junction node, and the three relationships that generate from applying the Rankine-Hugoniot or the Riemann invariant in system (79)–(80), we get the following system of nonlinear equations.

$$q_{1*} = \omega_2 q_{2*} + \omega_3 q_{3*} \tag{84}$$

$$h_{1*} + \frac{q_{1*}^2}{2gh_{1*}^2} = Z_2 + h_{2*} + \frac{q_{2*}^2}{2gh_{2*}^2} \tag{85}$$

$$h_{1*} + \frac{q_{1*}^2}{2gh_{1*}^2} = Z_3 + h_{3*} + \frac{q_{3*}^2}{2gh_{3*}^2} \tag{86}$$

$$q_{1*} = \xi_{1l}(h_{1*}; v_{1l}) \tag{87}$$

$$q_{2*} = \xi_{2r}(h_{2*}; v_{2r}) \tag{88}$$

$$q_{3*} = \xi_{3r}(h_{3*}; v_{3r}) \tag{89}$$

where ξ_{1l} is given by Equation (37). ξ_{2r} and ξ_{3r} are given by Equation (38). Therefore, the Riemann solution is equivalent to the solution of the nonlinear system (84)–(89).

3.3. *Existence and uniqueness of the junction Riemann solution*

Here, we show that the solution of the junction Riemann problem (79)–(80) exists under a certain hypothesis and it is unique under subcritical flow conditions.

Furthermore, we demonstrate also the physical conditions in which the solution does not exist. Therefore, we are looking to find intermediate state components $(h_{1*}, h_{2*}, h_{3*}, q_{1*}, q_{2*}, q_{3*})$ that satisfy the nonlinear system (84)–(89).

3.3.1. Mass-energy conservation at the junction

Let us assume that the left subcritical state v_{1*} is known. The states v_{2*} and v_{3*} are computed by solving the junction conditions (84)–(86). The states v_{2*} and v_{3*} are also expected to be subcritical states with $h_{2*} > 0$ and $h_{3*} > 0$. If we substitute the mass continuity Equation (84) into the total head balances Equations (85) and (86), the junction conditions give two algebraic equations of third order:

$$h_{2*}^3 + a_2 h_{2*}^2 + c_2 = 0, \, a_2 = -h_{1*} + Z_2 - \frac{q_{1*}^2}{2gh_{1*}^2}, c_2 = \left(\frac{r}{\omega_2}\right)^2 \frac{q_{1*}^2}{2g} \geq 0 \qquad (90)$$

$$h_{3*}^3 + a_3 h_{3*}^2 + c_3 = 0, \, a_3 = -h_{1*} + Z_3 - \frac{q_{1*}^2}{2gh_{1*}^2}, c_3 = \left(\frac{1-r}{\omega_3}\right)^2 \frac{q_{1*}^2}{2g} \geq 0 \qquad (91)$$

We introduce the specific energy in each cross section at the junction node to understand the physics of the flow.

$$\begin{cases} E_{1*} = h_{1*} + \frac{q_{1*}^2}{2gh_{1*}^2} \\ E_{2*} = h_{1*} + \left(\frac{r}{\omega_2}\right)^2 \frac{q_{1*}^2}{2gh_{2*}^2} \\ E_{3*} = h_{1*} + \left(\frac{1-r}{\omega_3}\right)^2 \frac{q_{1*}}{2gh_{3*}^2} \end{cases} \qquad (92)$$

Thus, the corresponding critical flow depths are

$$\begin{cases} h_{c1} = \sqrt[3]{\frac{q_{1*}^2}{g}} \\ h_{c2} = \sqrt[3]{\left(\frac{r}{\omega_2}\right)^2 \frac{q_{1*}^2}{g}} \\ h_{c3} = \sqrt[3]{\left(\frac{1-r}{\omega_3}\right)^2 \frac{q_{1*}^2}{g}} \end{cases} \qquad (93)$$

Using the first critical depth h_{c1} as the reference depth in the network to scale other critical depths, we get

$$\begin{cases} h_{c2} = \left(\frac{r}{\omega_2}\right)^{\frac{2}{3}} h_{c1} \\ h_{c3} = \left(\frac{1-r}{\omega_3}\right)^{\frac{2}{3}} h_{c1} \end{cases} \qquad (94)$$

and the critical specific energy in each cross section at the junction node is

$$\begin{cases} E_{c1} = \frac{3}{2} h_{c1} \\ E_{c2} = \frac{3}{2} \left(\frac{r}{\omega_2}\right)^{\frac{2}{3}} h_{c1} \\ E_{c3} = \frac{3}{2} \left(\frac{1-r}{\omega_3}\right)^{\frac{2}{3}} h_{c1} \end{cases} \qquad (95)$$

The critical depth h_{c1} and the critical specific energy E_{c1} are used to correlate the mathematical formula and the physical meaning. All depths and all specific

energies are in non-dimensional forms. Therefore, the non-dimensional depths are written as

$$\begin{cases} \eta_1 = \frac{h_{1*}}{h_{c1}} \\ \eta_2 = \frac{h_{2*}}{h_{c1}} \\ \eta_3 = \frac{h_{3*}}{h_{c1}} \end{cases} \tag{96}$$

and the non-dimensional specific energies are written to be

$$\begin{cases} \Gamma_1 = \frac{E_{1*}}{E_{c1}} \\ \Gamma_2 = \frac{E_{2*}}{E_{c1}} \\ \Gamma_3 = \frac{E_{3*}}{E_{c1}} \end{cases} \tag{97}$$

Thus, the fundamental relation between the non-dimensional specific energy and the non-dimensional depth at each channel as explained in details in [23] for a single channel, are

$$\begin{cases} \Gamma_1 = \frac{2}{3}\eta_1 + \frac{1}{3}\frac{1}{\eta_1^2} \\ \Gamma_2 = \frac{2}{3}\eta_2 + \frac{1}{3}\left(\frac{r}{\omega_2}\right)^2 \frac{1}{\eta_2^2} \\ \Gamma_3 = \frac{2}{3}\eta_3 + \frac{1}{3}\left(\frac{1-r}{\omega_3}\right)^2 \frac{1}{\eta_3^2} \end{cases} \tag{98}$$

For more clarification about the physical meaning of the previous dimensionless quantities, the relationships by Equation (98) are justified in Figure 11 for a set of parameters $r = 0.7$, $\omega_2 = 0.2$, and $\omega_3 = 0.8$. The solid-curve shows the relation between the energy and the depth for the first channel. This curve is divided into two parts by the dotted unity slope line, the upper part is according to the subcritical flow and the lower part is according to the supercritical flow. Similarly, the dashed and dotted curves are the second channel and third channel curves, respectively. Note that the areas between the curves and the axis are physically not possible and therefore there are no flow states belonging to these areas. Very important parameters are the discharge ratio r and the contraction ratio ω that they control the relationships shown in Figure 11. The influence of r and ω into the solutions is highlighted here rather in such a way that the variables η and Γ are investigated by considering the following domains:

$$1 < \eta_1 < \infty, \quad \left(\frac{r}{\omega_2}\right)^{\frac{2}{3}} < \eta_2 < \infty, \quad \left(\frac{1-r}{\omega_3}\right)^{\frac{2}{3}} < \eta_3 < \infty \tag{99}$$

$$1 \le \Gamma_1 < \infty, \quad \left(\frac{r}{\omega_2}\right)^{\frac{2}{3}} \le \Gamma_2 < \infty, \quad \left(\frac{1-r}{\omega_3}\right)^{\frac{2}{3}} \le \Gamma_3 < \infty \tag{100}$$

Since the study is limited to the subcritical flow, then the choking of the flow and the critical transition are excluded. In other words, the specific energy in any cross-section in the network is necessary larger than the critical value.

This condition is important to pass over the junction without transition from the subcritical to supercritical flow. Using the dimensionless quantities by
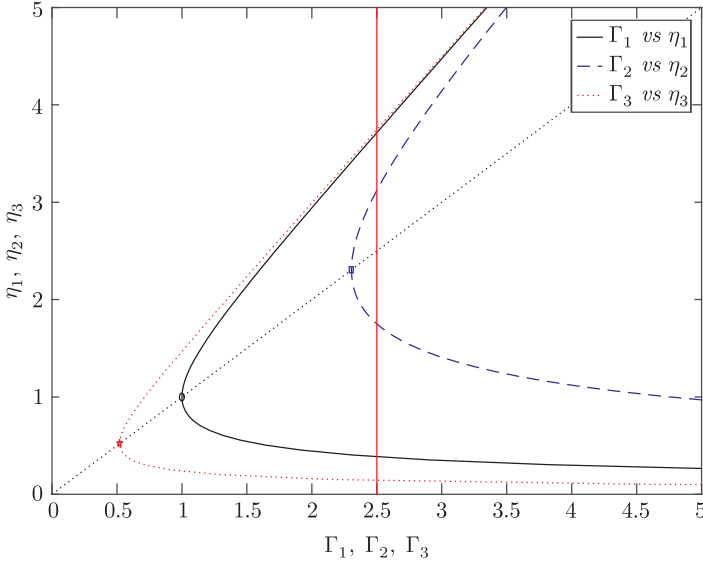
Figure 11. Energy *vs* depth

Equations (96)–(98), Equations (90) and (91) are rewritten in the following non-dimensional forms

$$\eta_2^3 + \Theta_2\eta_2^2 + \mu_2 = 0, \Theta_2 = -\frac{3}{2}\Gamma_1 + \Delta\mathcal{Z}_2, \mu_2 = \frac{1}{2}\left(\frac{r}{\omega_2}\right)^2 \qquad (101)$$

$$\eta_3^3 + \Theta_3\eta_3^2 + \mu_3 = 0, \Theta_3 = -\frac{3}{2}\Gamma_1 + \Delta\mathcal{Z}_3, \mu_3 = \frac{1}{2}\left(\frac{1-r}{\omega_3}\right)^2 \qquad (102)$$

$\Delta\mathcal{Z}_2 = \frac{Z_2}{h_{c1}}$ and $\Delta\mathcal{Z}_3 = \frac{Z_3}{h_{c1}}$ are the non-dimensional bottom discontinuities terms. Equations (101)–(102) are third degree polynomial generalized in the following form

$$P(\eta) = \eta^3 + \Theta\eta^2 + \mu; \quad \eta = (\eta_2, \eta_3) \quad \Theta = (\Theta_2, \Theta_3), \quad \mu = (\mu_3, \mu_3) \qquad (103)$$

Taking into account the proper domains of r and ω that ensure the fulfillment of the subcritical conditions, this always implies μ to be positive. For the forward facing step bottom the maximum permitted step height is simply equal to the difference between the upstream specific energy and the critical downstream specific energy as shown in [16], that gives:

$$\frac{2}{3}\Delta\mathcal{Z}_2 \le \Gamma_1 - \left(\frac{r}{\omega_2}\right)^{\frac{2}{3}}, \quad \frac{2}{3}\Delta\mathcal{Z}_3 \le \Gamma_1 - \left(\frac{1-r}{\omega_3}\right)^{\frac{2}{3}} \qquad (104)$$

It is worth mentioning that Equation (104) and the restriction on the subcritical conditions imply $\Theta < 0$. $\mu > 0$ follows from the constrains on the discharge ratio r and the width ratio ω. By applying Cardano's method to compute the roots of the

cubic equation which is explained in detail by [45], the roots of Equation (103) depend on the following relationships (discriminants):

$$\Delta_2 = \mu_2 \left(\frac{4}{27} \Theta_2^3 + \mu_2 \right) \tag{105}$$

$$\Delta_3 = \mu_3 \left(\frac{4}{27} \Theta_3^3 + \mu_3 \right) \tag{106}$$

The polynomial roots are complex roots if $\Delta > 0$, they are multiple roots if $\Delta = 0$, and they are real roots if $\Delta < 0$.

Considering the definitions of Θ and μ parameters in Equations (101)–(102), and the subcritical conditions, the following equations are true

$$\frac{4}{27} \Theta_2^3 + \mu_2 = -\frac{1}{2} \left(\Gamma_1 - \frac{2}{3} \Delta \mathcal{Z}_2 \right)^3 + \frac{1}{2} \left(\frac{r}{\omega_2} \right)^2 = -\frac{1}{2} \Gamma_2^3 + \frac{1}{2} \left(\frac{r}{\omega_2} \right)^2 < 0 \tag{107}$$

$$\frac{4}{27} \Theta_3^3 + \mu_3 = -\frac{1}{2} \left(\Gamma_1 - \frac{2}{3} \Delta \mathcal{Z}_3 \right)^3 + \frac{1}{2} \left(\frac{1-r}{\omega_3} \right)^2 = -\frac{1}{2} \Gamma_3^3 + \frac{1}{2} \left(\frac{1-r}{\omega_3} \right)^2 < 0 \tag{108}$$

in the physical domain of Γ_1, Γ_2, and Γ_3 as given in Equation (100). Furthermore, $\mu > 0$ and Equations (107)–(108) lead to $\Delta < 0$ and therefore the polynomial shown by Equation (103) has three real roots. Equation (104) is equivalent to the inequalities $\Delta_2 < 0$ and $\Delta_3 < 0$. Indeed, the restriction on the discriminants (Δ) is related to the step height that it is compared to the specific energy values.

For a given set of initial states and parameters (Γ_1, $\Delta \mathcal{Z}_2$, $\Delta \mathcal{Z}_3$), the admissible ranges of $\frac{r}{\omega_2}$ and of $\frac{1-r}{\omega_3}$ are determined as follows

$$\left(\frac{r}{\omega_2} \right) \leq \left(\Gamma_1 - \frac{2}{3} \Delta \mathcal{Z}_2 \right)^{\frac{3}{2}}, \quad \left(\frac{1-r}{\omega_3} \right) \leq \left(\Gamma_1 - \frac{2}{3} \Delta \mathcal{Z}_3 \right)^{\frac{3}{2}} \tag{109}$$

The discharge ratio r and the width ratio (*i.e.*, contraction ratio) ω must fulfill the condition given in Equation (109) for a certain range of η_1 and $\Delta \mathcal{Z}$. Equation (109) can be read as the maximum contraction degree of the channel width that is compatible with the subcritical flow conditions across the junction. Moreover, considering the following expressions

$$-1 - \frac{27 \Theta_2}{2 \mu_2^3} = -1 + 2 \left(\frac{r}{\omega_2} \right)^2 \frac{1}{\Gamma_2^3}, \quad -1 - \frac{27 \Theta_3}{2 \mu_3^3} = -1 + 2 \left(\frac{1-r}{\omega_3} \right)^2 \frac{1}{\Gamma_3^3} \tag{110}$$

and using the physical domains defined in Equation (100), we obtain

$$-1 < -1 - \frac{27 \Theta}{2 \mu^3} < 1, \quad 0 < \theta = \arccos \left(-1 - \frac{27 \Theta}{2 \mu^3} \right) < \pi \tag{111}$$

Thus, taking into account $\Delta < 0$ and the inequalities shown by Equation (111), applying Cardano's method and trigonometry properties, the polynomial shown by Equation (103) admits three real roots. The first root is

$$\eta^{(1)} = \left(\frac{1}{2} \Gamma_1 - \frac{1}{3} \Delta \mathcal{Z} \right) \left[1 - 2 \cos \left(\frac{\theta}{3} \right) \right] \tag{112}$$

From Equations (100) and (111), $\eta^{(1)}$ is determined to be real and negative and therefore it is excluded because the water depth is negative (water depth must be greater than zero). The second root is

$$\eta^{(2)} = \left(\frac{1}{2}\Gamma_1 - \frac{1}{3}\Delta \mathcal{Z}\right)\left[1 - 2\cos\left(\frac{2\pi - \theta}{3}\right)\right] \tag{113}$$

Similarly, from Equations (100) and (111), $\eta^{(2)}$ is determined to be positive and less than $\left(\frac{r}{\omega_2}\right)^{2/3}$ for the second channel and less than $\left(\frac{1-r}{\omega_3}\right)^{2/3}$ for the third channel. Therefore, the root $\eta^{(2)}$ is said to be the supercritical solution. This solution is excluded because it is beyond the scope of the thesis. Finally, the third root is

$$\eta^{(3)} = \left(\frac{1}{2}\Gamma_1 - \frac{1}{3}\Delta \mathcal{Z}\right)\left[1 - 2\cos\left(\frac{2\pi + \theta}{3}\right)\right] \tag{114}$$

In the same way, $\eta^{(3)}$ is determined to be real and positive from Equations (100) and (111). It is greater than $\left(\frac{r}{\omega_2}\right)^{2/3}$ for the second channel and greater than $\left(\frac{1-r}{\omega_3}\right)^{2/3}$ for the third channel. Therefore, the root $\eta^{(3)}$ is the subcritical solution.

The following lemma summarizes the results in terms of dimensional variables such that $Y = \eta^{(3)}h_{c1}$ and $\eta^{(3)} = (\eta_2, \eta_3)$

3.3.2. Lemma

For a given left state v_{1*} such that the subcritical flow condition is fulfilled, there will be only two right states v_{2*} and v_{3*} that satisfy the junction conditions given in Equations (81)−(83). Therefore, the right states are determined as follows

$$v_{2*} = \begin{bmatrix} Y(a_2, c_2) \\ \left(\frac{r}{\omega_2}\right)q_{1*} \\ z_2 \end{bmatrix} ; Y(a_2, c_2) = -\frac{a_2}{3}\left[1 - 2\cos\left(\frac{2\pi + \theta_2}{3}\right)\right] \tag{115}$$

$$v_{3*} = \begin{bmatrix} Y(a_3, c_3) \\ \left(\frac{1-r}{\omega_3}\right)q_{1*} \\ z_3 \end{bmatrix} ; Y(a_3, c_3) = -\frac{a_3}{3}\left[1 - 2\cos\left(\frac{2\pi + \theta_3}{3}\right)\right] \tag{116}$$

where

$$a_2 = -h_{1*} + Z_2 - \frac{q_{1*}^2}{2gh_{1*}^2}, c_2 = \left(\frac{r}{\omega_2}\right)^2\frac{q_{1*}^2}{2g}, \theta_2 = \arccos\left(-1 - \frac{27c_2}{2a_2^3}\right) \tag{117}$$

$$a_3 = -h_{1*} + Z_3 - \frac{q_{1*}^2}{2gh_{1*}^2}, c_3 = \left(\frac{1-r}{\omega_3}\right)^2\frac{q_{1*}^2}{2g}, \theta_3 = \arccos\left(-1 - \frac{27c_3}{2a_3^3}\right) \tag{118}$$

The discharge ratio r and the width ratio ω satisfy Equations (81) and (109).

3.3.3. Junction curves

We consider the loci curves defined in Section 2.3 and the mass-energy conservation at the junction in Subsection 3.3.1.

We take the states $\mathbf{v}_{1o} \in \tau_{1l}(h_{1o}, \mathbf{v}_{1l})$, $\mathbf{v}_{2o} \in \tau_{2r}(h_{2o}, \mathbf{v}_{2r})$, and $\mathbf{v}_{3o} \in \tau_{3r}(h_{3o}; \mathbf{v}_{3r})$. Then, the physically admissible states for any value of h_{1o} are the state pair $(h_{2\triangleright}, q_{2\triangleright})$ and $(h_{3\triangleright}, q_{3\triangleright})$. These states satisfy the subcritical flow conditions. They connect to the state $\mathbf{v}_{1o}$ by the mass-energy conservation at the junction. The state pair $(h_{2\triangleright}, q_{2\triangleright})$ and $(h_{3\triangleright}, q_{3\triangleright})$ satisfy the following equations

$$h_{2\triangleright} = Y(\mathrm{a}_2(h_{1o}), \mathrm{c}_2(h_{1o})), \quad q_{2\triangleright} = \frac{r}{\omega_2}\xi_{1l}(h_{1o}, \mathbf{v}_{1l}) \tag{119}$$

$$h_{3\triangleright} = Y(\mathrm{a}_3(h_{1o}), \mathrm{c}_3(h_{1o})), \quad q_{3\triangleright} = \frac{(1-r)}{\omega_3}\xi_{1l}(h_{1o}, \mathbf{v}_{1l}) \tag{120}$$

where $Y(.,.)$ is given by Equations (115) and (116) such that

$$\mathrm{a}_2(h_{1o}) = -h_{1o} + Z_2 - \frac{\xi_{1l}^2(h_{1o}, \mathbf{v}_{1l})}{2gh_{1o}^2}, \quad \mathrm{c}_2(h_{1o}) = \left(\frac{r}{\omega_2}\right)^2 \frac{\xi_{1l}^2(h_{1o}, \mathbf{v}_{1l})}{2g} \tag{121}$$

$$\mathrm{a}_3(h_{1o}) = -h_{1o} + Z_3 - \frac{\xi_{1l}^2(h_{1o}, \mathbf{v}_{1l})}{2gh_{1o}^2}, \quad \mathrm{c}_2(h_{1o}) = \left(\frac{(1-r)}{\omega_3}\right)^2 \frac{\xi_{1l}^2(h_{1o}, \mathbf{v}_{1l})}{2g} \tag{122}$$

$\xi_{1l}(h_{1o}, \mathbf{v}_{1l})$ is given in Equations (37) and (38). Hence, the junction curves denoted by $J_2(h_{1o}, \mathbf{v}_{1l})$ and $J_3(h_{1o}, \mathbf{v}_{1l})$ are defined as follows

$$J_2(h_{1o}, \mathbf{v}_{1l}) = \begin{bmatrix} h_{2\triangleright} \\ q_{2\triangleright} \end{bmatrix}, \quad J_3(h_{1o}, \mathbf{v}_{1l}) = \begin{bmatrix} h_{3\triangleright} \\ q_{3\triangleright} \end{bmatrix} \tag{123}$$
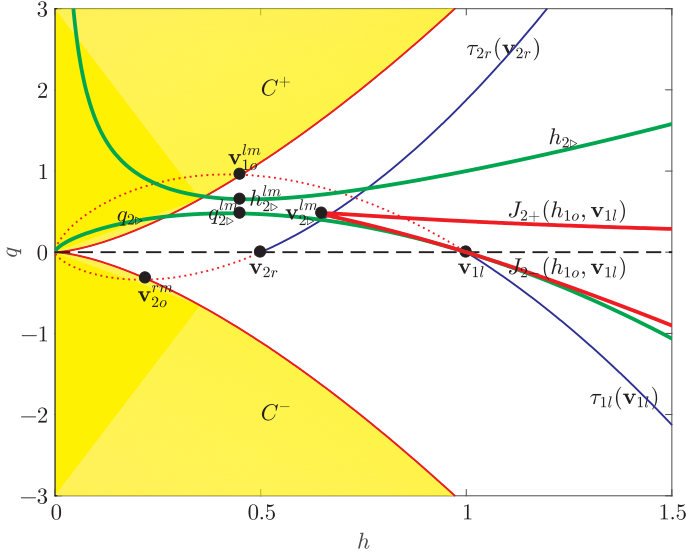

Figure 12. Two branches of single junction curve

The two generated branches of each single junction curve are geometrically described by Figure 12. The curves shown in green-thick lines are the discharge and depth components of the junction curve. The upper one refers to the depth components given by Equations (119)–(120). The lower green curve shows the

discharge components given by Equations (119)–(120). The minimum and the maximum values of the upper and lower green curves are $q_{2\triangleright}^{lm}$ and $h_{2\triangleright}^{lm}$, respectively. The intervals $]0, h_{2\triangleright}^{lm}]$ and $]0, q_{2\triangleright}^{lm}]$ are due to the supercritical flow conditions and therefore they are combined together to plot the first junction branch $J_{2+}(\mathbf{v}_{1l})$. The intervals $]h_{2\triangleright}^{lm}, +\infty]$ and $]q_{2\triangleright}^{lm}, +\infty]$ are due to the subcritical flow conditions which are mostly combined together to give the second junction branch $J_{2-}(\mathbf{v}_{1l})$. Both junction branches are shown in thick-red lines. Here and after, the only admissible junction branch which fulfills the subcritical flow conditions is the branch $J_{2-}(\mathbf{v}_{1l})$. We globally refer to this branch as the junction curve for simplicity. Note that the branches of the second junction curve $J_2(\mathbf{v}_{1l})$ are defined in the same way. These results are matching the physical meaning showing in Figure 11.

Indeed, the intermediate states in the solution of the junction Riemann problem are determined when the junction curve J_{2-} intersects with the locus curve τ_{2r}. The junction curve J_{3-} intersects with the locus curve τ_{3r} and the corresponding states on the locus curve τ_{1l}. In the next Lemmas, we investigate the extrema of the junction functions $Y(\mathrm{a}(h_{1o}), \mathrm{c}(h_{1o}))$.

3.3.4. Lemma

Consider the functions $Y(a(h_{1o}), c(h_{1o}))$ defined by Equations (115)–(116), the minima of such functions are determined at the maximum states $(h_{1o}^{lm}, q_{1o}^{lm})$ given by Lemma 2.4.1, such that the following holds

$$
\begin{cases}
\frac{dY(\mathrm{a}_2(h_{1o}), \mathrm{c}_2(h_{1o}))}{dh_{1o}}\big|_{h_{1o}=h_{1o}^{lm}} = 0 \\
\frac{d^2Y(\mathrm{a}_2(h_{1o}), \mathrm{c}_2(h_{1o}))}{dh_{1o}^2}\big|_{h_{1o}=h_{1o}^{lm}} > 0
\end{cases}
\tag{124}
$$

$$
\begin{cases}
\frac{dY(\mathrm{a}_3(h_{1o}), \mathrm{c}_3(h_{1o}))}{dh_{1o}}\big|_{h_{1o}=h_{1o}^{lm}} = 0, \\
\frac{d^2Y(\mathrm{a}_3(h_{1o}), \mathrm{c}_3(h_{1o}))}{dh_{1o}^2}\big|_{h_{1o}=h_{1o}^{lm}} > 0
\end{cases}
\tag{125}
$$

Moreover, the functions $Y(a(h_{1o}), c(h_{1o}))$ are decreasing in $]0, h_{1o}^{lm}]$ and increasing in $[h_{1o}^{lm}, \infty[$. The decreasing part of the functions varies from

$$
\lim_{h_{1o}\to 0^+} Y(\mathrm{a}_2(h_{1o}), \mathrm{c}_2(h_{1o})) = \frac{9}{2} h_{1o}^{lm} - Z_2 \quad \text{to} \quad Y_{2o}^{lm}
\tag{126}
$$

$$
\lim_{h_{1o}\to 0^+} Y(\mathrm{a}_3(h_{1o}), \mathrm{c}_3(h_{1o})) = \frac{9}{2} h_{1o}^{lm} - Z_3 \quad \text{to} \quad Y_{3o}^{lm}
\tag{127}
$$

while, the increasing part varies from

$$
Y_{1o}^{lm} \quad \text{to} \quad \lim_{h_{1o}\to 0^+} Y(\mathrm{a}_2(h_{1o}), \mathrm{c}_2(h_{1o})) = +\infty
\tag{128}
$$

$$
Y_{2o}^{lm} \quad \text{to} \quad \lim_{h_{1o}\to 0^+} Y(\mathrm{a}_3(h_{1o}), \mathrm{c}_3(h_{1o})) = +\infty
\tag{129}
$$

with

$$
Y_{1o}^{lm} = \left(\frac{h_{1o}^{lm}}{2} - \frac{Z_2}{3} \right) \left[1 - 2\cos\left(\frac{\theta_2 + 2\pi}{3} \right) \right]
\tag{130}
$$

$$Y_{2o}^{lm} = \left(\frac{h_{1o}^{lm}}{2} - \frac{Z_3}{3} \right) \left[1 - 2\cos\left(\frac{\theta_3 + 2\pi}{3} \right) \right] \tag{131}$$

such that

$$\theta_2 = \arccos\left(-1 + 2 \left(\frac{r}{\omega_2} \right)^2 \left(\frac{h_{1o}^{lm}}{h_{1o}^{lm} - \frac{2}{3}\Delta Z_2} \right)^3 \right) \tag{132}$$

$$\theta_3 = \arccos\left(-1 + 2 \left(\frac{1-r}{\omega_3} \right)^2 \left(\frac{h_{1o}^{lm}}{h_{1o}^{lm} - \frac{2}{3}\Delta Z_3} \right)^3 \right) \tag{133}$$

The proof of Lemma 3.3.4 is as follows.

Proof

The functions $Y(a(h_{1o}), c(h_{1o}))$, and $\xi(h_{1o})$ are smooth functions and therefore their derivatives exist. Denote

$$\Psi(h_{1o}) = -1 - \frac{27c(h_{1o})}{2a^3(h_{1o})} \tag{134}$$

Then, the derivatives of $Y(a(h_{1o}), c(h_{1o}))$ with respect to the depth component h_{1o} give

$$\begin{aligned} \frac{dY(a(h_{1o}), c(h_{1o}))}{dh_{1o}} &= \frac{1}{3} a'(h_{1o}) \left[2\cos\left(\frac{1}{3}\arccos\left(\Psi(h_{1o})\right) + \frac{2\pi}{3} \right) - 1 \right] \\ &\quad - \frac{2}{9} \frac{a(h_{1o})\Psi'(h_{1o})}{\sqrt{1 - \Psi^2(h_{1o})}} \sin\left(\frac{1}{3}\arccos(\Psi(h_{1o})) + \frac{2\pi}{3} \right) \end{aligned} \tag{135}$$

By Equation (134), the derivatives of $\Psi(h_{1o})$ with respect to h_{1o} give

$$\Psi' = -\frac{27c'(h_{1o})}{2a^3(h_{1o})} + \frac{81a'(h_{1o})c(h_{1o})}{2a^4(h_{1o})} \tag{136}$$

such that

$$a'(h_{1o}) = -1 - \frac{\xi_{1l}'(h_{1o})}{gh_{1o}^2} + \frac{\xi_{il}^2(h_{1o})}{gh_{1o}^3} \tag{137}$$

$$c'(h_{1o}) = \frac{R}{\omega} \frac{\xi_{il}'(h_{1o})\xi_{il}(h_{1o})}{2g} \tag{138}$$

where, R is equal to r or $1-r$ according to the order of the channels. From Equations (40)–(41) in Lemma 2.4.1, the derivative of the discharge component $\xi_{1l}(h_{1o})$ when h_{1o} tends to h_{1o}^{lm}, gives

$$\xi_{1l}'(h_{1o}^{lm}) = 0; \quad \xi_{1l}(h_{1o}^{lm}) = h_{1o}^{lm}\sqrt{gh_{1o}^{lm}} \tag{139}$$

Thus

$$\begin{aligned} a'(h_{1o}^{lm}) &= 0 \\ c'(h_{1o}^{lm}) &= 0 \end{aligned} \tag{140}$$

and therefore

$$\Psi'(h_{1o}^{lm}) = 0 \tag{141}$$

Inserting Equations (140)–(141) inside Equation (135) gives

$$\frac{dY(a(h_{1o}),c(h_{1o}))}{dh_{1o}}\Big|_{h_{1o}=h_{1o}^{lm}} = 0 \tag{142}$$

Equation (142) proves the minimum of the functions $Y(a(h_{1o}),c(h_{1o}))$ at the depth h_{1o}^{lm}. As for the second derivatives that show the convexity of the function, we rewrite the first derivatives of functions $Y(a(h_{1o}),c(h_{1o}))$ for simplicity as follows

$$\frac{dY(a(h_{1o}),c(h_{1o}))}{dh_{1o}} = \frac{1}{3}a'(h_{1o})\Phi_1(h_{1o}) - \frac{2}{9}a(h_{1o})\Psi'(h_{1o})\Phi_2(h_{1o})\Phi_3(h_{1o}) \tag{143}$$

such that,

$$\Phi_1(h_{1o}) = 2\cos\left(\frac{1}{3}\arccos(\Psi(h_{1o})) + \frac{2\pi}{3}\right) - 1 \tag{144}$$

$$\Phi_2(h_{1o}) = \frac{1}{\sqrt{1 - \Psi^2(h_{1o})}} \tag{145}$$

$$\Phi_3(h_{1o}) = \sin\left(\frac{1}{3}\arccos(\Psi(h_{1o})) + \frac{2\pi}{3}\right) \tag{146}$$

The second derivatives of $Y(a(h_{1o}),c(h_{1o}))$ give

$$\frac{d^2Y(a(h_{1o}),c(h_{1o}))}{dh_{1o}^2} = \frac{1}{3}\left(a''(h_{1o})\Phi_1(h_{1o}) + a'(h_{1o})\Phi_1'(h_{1o})\right)$$

$$- \frac{2}{9}\Phi_2(h_{1o})\Phi_3(h_{1o})\left[a'(h_{1o})\Psi'(h_{1o}) + a(h_{1o})\Psi''(h_{1o})\right] \tag{147}$$

$$- \frac{2}{9}a(h_{1o})\Psi'(h_{1o})\left[\Phi_2'(h_{1o})\Phi_3(h_{1o}) + \Phi_2(h_{1o})\Phi_3'(h_{1o})\right]$$

where from Equation (136) the second derivative of Ψ is

$$\Psi'' = -\frac{27c''}{2a^3} + \frac{81a''c}{2a^4} + \frac{135a'c'}{2a^4} - \frac{162(a')^2c}{a^5} \tag{148}$$

such that a' and c' are given by Equations (137) and (138), respectively. The second derivatives of a' and c' are

$$a'' = \frac{1}{g}\left[-\frac{\xi_{1l}''\xi_{1l}}{h_{1o}^2} - \frac{(\xi_{1l}')^2}{h_{1o}^2} + 4\frac{\xi_{1l}'\xi_{1l}}{h_{1o}^3} - 3\frac{\xi_{1l}^2}{h_{1o}^4}\right] \tag{149}$$

$$c'' = \frac{1}{2g}\left(\frac{R}{w}\right)^2 (\xi_{1l}''\xi_{1l} + (\xi_{1l}')^2) \tag{150}$$

where, ξ_{1l}' and ξ_{1l}'' are given by Equations (53) and (54), respectively. The remaining derivatives are

$$\Phi_1' = -\frac{2}{3}\frac{\Psi'}{\sqrt{1-\Psi^2}}\sin\left(\frac{1}{3}\arccos(\Psi) + \frac{2\pi}{3}\right)$$

$$\Phi_2' = \frac{\Psi'\Psi}{(1-\Psi^2)^{3/2}} \tag{151}$$

$$\Phi_3' = \frac{1}{3}\frac{\Psi'}{\sqrt{1-\Psi^2}}\cos\left(\frac{1}{3}\arccos(\Psi) + \frac{2\pi}{3}\right)$$

Since $\xi'_{1l}(h_{1o}^{lm}) = 0$, $a'_{1l}(h_{1o}^{lm}) = 0$, $c'_{1l}(h_{1o}^{lm}) = 0$, and $\Psi'(h_{1o}^{lm}) = 0$, then Equation (147) evaluated at h_{1o}^{lm}, is simplified to

$$
\begin{aligned}
&\frac{d^2 Y(a(h_{1o}), c(h_{1o}))}{dh_{1o}^2}\Big|_{h_{o1}=h_{1o}^{lm}} = \\
&\frac{1}{3} a''(h_{1o}^{lm}) \Phi_1(h_{1o}^{lm}) - \frac{2}{9} \Phi_2(h_{1o}^{lm}) \Phi_3(h_{1o}^{lm}) a(h_{1o}^{lm}) \Psi''(h_{1o}^{lm})
\end{aligned}
\tag{152}
$$

From Equations (41), (54), and (121)–(122) we have

$$
\xi_{1l}(h_{1o}^{lm}) = h_{1o}^{lm} \sqrt{gh_{1o}^{lm}}, \quad \xi''_{1l}(h_{1o}^{lm}) = -\frac{3g}{2\sqrt{gh_{1o}^{lm}}}
\tag{153}
$$

$$
a(h_{1o}^{lm}) = -\frac{3}{2} h_{1o}^{lm} + Z, \quad c(h_{1o}^{lm}) = \frac{1}{2} \left(\frac{R}{\omega} \right)^2 (h_{1o}^{lm})^2
\tag{154}
$$

By inserting Equation (154) into Equation (134), we obtain

$$
\Psi(h_{1o}^{lm}) = -1 - 2 \left(\frac{R}{\omega} \right)^2 \left(\frac{h_{1o}^{lm}}{-h_{1o}^{lm} + \frac{2}{3}Z} \right)^3
\tag{155}
$$

then it follows from Equations (144)–(146) that

$$
\Phi_1(h_{1o}^{lm}) = 2\cos\left(\frac{1}{3} \arccos(\Psi(h_{1o}^{lm})) + \frac{2\pi}{3} \right) - 1
\tag{156}
$$

$$
\Phi_2(h_{1o}^{lm}) = \frac{1}{\sqrt{1 - \Psi^2(h_{1o}^{lm})}}
\tag{157}
$$

$$
\Phi_3(h_{1o}^{lm}) = \sin\left(\frac{1}{3} \arccos(\Psi(h_{1o}^{lm})) + \frac{2\pi}{3} \right)
\tag{158}
$$

and

$$
a''(h_{1o}^{lm}) = -\frac{3}{2} \frac{1}{h_{1o}^{lm}}
\tag{159}
$$

Simple calculation implies directly that Equation (147) satisfies the following

$$
\frac{d^2 Y(a(h_{1o}), c(h_{1o}))}{dh_{1o}^2}\Big|_{h_{1o}=h_{1o}^{lm}} > 0
\tag{160}
$$

Finally, we end the proof of Lemma 3.3.4 by considering Equations (115), (116), (121), (122), and the rarefaction portion of the left locus curve. We have

$$
\lim_{h_{1o}\to 0^+} Y(a(h_{1o}), c(h_{1o})) = -\lim_{h_{1o}\to 0^+} a(h_{1o}) = \frac{9}{2} h_{1o}^{lm} - Z
\tag{161}
$$

$$
\lim_{h_{1o}\to 0^+} Y(a(h_{1o}), c(h_{1o})) = +\infty
\tag{162}
$$

∎

3.3.5. Lemma

The junction curves $J_2(h_{1o}, \mathbf{v}_{1l})$-$J_3(h_{1o}, \mathbf{v}_{1l})$ consist of two branches connected by the minimum states. They are denoted by $\mathbf{v}_{2\triangleright}^{lm}$ and $\mathbf{v}_{3\triangleright}^{lm}$, respectively. These states correspond to $\mathbf{v}_{1o}^{lm}$ by the junction conditions with

$$
\begin{cases}
h_{2\triangleright}^{lm} = Y_{1o}^{lm}, & q_{2\triangleright}^{lm} = \left(\frac{r}{\omega_2}\right) q_{1o}^{lm} \\
h_{3\triangleright}^{lm} = Y_{2o}^{lm}, & q_{3\triangleright}^{lm} = \left(\frac{1-r}{\omega_3}\right) q_{1o}^{lm}
\end{cases}
\tag{163}
$$

where Y_{1o}^{lm} and Y_{2o}^{lm} are given by Proposition 3.3.4. q_{1o}^{lm} is given by Lemma 2.4.1. For any state $(h_{2\triangleright}, q_{2\triangleright})$ on the junction curve $J_2(h_{1o}, \mathbf{v}_{1l})$ and $(h_{3\triangleright}, q_{3\triangleright})$ on the junction curve $J_3(h_{1o}, \mathbf{v}_{1l})$, we have

$$
\begin{cases}
h_{2\triangleright} \geq Y_{1o}^{lm} \\
h_{3\triangleright} \geq Y_{2o}^{lm}
\end{cases}
\tag{164}
$$

Furthermore, the following inequalities are true.

$$
\begin{cases}
\frac{dh_{2\triangleright}}{dh_{1o}} < 0, & \frac{dq_{2\triangleright}}{dh_{1o}} > 0, & \text{if } 0 < h_{1o} < h_{1o}^{lm} \\
\frac{dh_{3\triangleright}}{dh_{1o}} < 0, & \frac{dq_{3\triangleright}}{dh_{1o}} > 0, & \text{if } 0 < h_{1o} < h_{1o}^{lm}
\end{cases}
\tag{165}
$$

$$
\begin{cases}
\frac{dh_{2\triangleright}}{dh_{1o}} = 0, & \frac{dq_{2\triangleright}}{dh_{1o}} = 0, & \text{if } h_{1o} = h_{1o}^{lm} \\
\frac{dh_{3\triangleright}}{dh_{1o}} = 0, & \frac{dq_{3\triangleright}}{dh_{1o}} = 0, & \text{if } h_{1o} = h_{1o}^{lm}
\end{cases}
\tag{166}
$$

$$
\begin{cases}
\frac{dh_{2\triangleright}}{dh_{1o}} > 0, & \frac{dq_{2\triangleright}}{dh_{1o}} < 0, & \text{if } h_{1o}^{lm} < h_{1o} < +\infty \\
\frac{dh_{3\triangleright}}{dh_{1o}} > 0, & \frac{dq_{3\triangleright}}{dh_{1o}} < 0, & \text{if } h_{1o}^{lm} < h_{1o} < +\infty
\end{cases}
\tag{167}
$$

The proof of Lemma 3.3.5 is as follows.

Proof

In general, we provide the proof steps for both junction curves. Consider the state $\mathbf{v}_{\triangleright}^{lm}$ connected to $\mathbf{v}_{1o}^{lm}$ through the mass-energy conditions at the junction. Equation (163) follows by considering Equations (119)–(120) and Lemmas 2.4.1 and 3.3.4. As long as h_{1o}^{lm} is the minimum of the function $Y(a(h_{1o}), c(h_{1o}))$ shown by Lemma 3.3.4, we get

$$
\mathbf{v}_{\triangleright} = Y(a(h_{1o}), c(h_{1o})) \geq Y_o^{lm}
\tag{168}
$$

The proof ends by using Lemmas 2.4.1 and 3.3.4, whilst Equations (165)–(167) hold. ∎

Lemmas 3.3.4 and 3.3.5 illustrate that each junction curve has two branches. Positive branches are due to non-subcritical states, such that Equations (165) and (166) are satisfied. Such branches denote $J_{2+}(h_{1o}, \mathbf{v}_{1l})$ and $J_{3+}(h_{1o}, \mathbf{v}_{1l})$ for the first and second junction curves, respectively. Therefore, $J_{2+}(h_{1o}, \mathbf{v}_{1l})$ and $J_{3+}(h_{1o}, \mathbf{v}_{1l})$ branches are excluded because subcritical flow conditions are violated. Negative branches of the junction curves denote $J_{2-}(h_{1o}, \mathbf{v}_{1l})$ and $J_{3-}(h_{1o}, \mathbf{v}_{2l})$. They satisfy Equations (166)–(167). These branches fulfill the

subcritical flow conditions. Indeed, the intermediate states in the solution of the junction Riemann problem are obtained such that the junction branches J_{2-} and J_{3-} intersect with the right locus curves $\tau_{2r}(h_{1o}, \mathbf{v}_{2r})$ and $\tau_{3r}(h_{1o}, \mathbf{v}_{3r})$, respectively.

Furthermore, Lemmas 2.4.1, 2.4.2, 3.3.2, 3.3.4, and 3.3.5 are necessary to construct the Riemann solution. The solution is summarized in the following theorem.

3.3.6. Junction Riemann theorem

The Riemann Problem defined in (79)–(83) has a unique solution if and only if

$$
\begin{cases}
q_{2\triangleright}^{lm} > \xi_{2r}(h_{2\triangleright}^{lm}, \mathbf{v}_{2r}) \\
q_{3\triangleright}^{lm} > \xi_{3r}(h_{3\triangleright}^{lm}, \mathbf{v}_{3r})
\end{cases}
\tag{169}
$$

where the state pair $(h_{2\triangleright}^{lm}, q_{2\triangleright}^{lm})$ and $(h_{3\triangleright}^{lm}, q_{3\triangleright}^{lm})$ are given by Lemma 3.3.5, and the locus functions ξ_{2r} and ξ_{3r} are given by Equation (38), such that the condition is satisfied by Equation (104). Therefore, the intermediate states of the junction Riemann solution are determined by

$$
\mathbf{v}_{1*} = \begin{bmatrix} h_{1*} \\ q_{1*} \\ z_1 \end{bmatrix} = \begin{bmatrix} h_{1\triangleright} \\ \xi_{1l}(h_{1\triangleright}, \mathbf{v}_{1l}) \\ z_1 \end{bmatrix}
\tag{170}
$$

$$
\mathbf{v}_{2*} = \begin{bmatrix} h_{2*} \\ q_{2*} \\ z_2 \end{bmatrix} = \begin{bmatrix} Y(\mathrm{a}_2(h_{1\triangleright}), \mathrm{c}_2(h_{1\triangleright})) \\ \xi_{2r}(Y(\mathrm{a}_2(h_{1\triangleright}), \mathrm{c}_2(h_{1\triangleright})), \mathbf{v}_{2r}) \\ z_2 \end{bmatrix}
\tag{171}
$$

$$
\mathbf{v}_{3*} = \begin{bmatrix} h_{3*} \\ q_{3*} \\ z_3 \end{bmatrix} = \begin{bmatrix} Y(\mathrm{a}_3(h_{1\triangleright}), \mathrm{c}_3(h_{1\triangleright})) \\ \xi_{3r}(Y^{(1)}(\mathrm{a}_3(h_{1\triangleright}), \mathrm{c}_3(h_{1\triangleright})), \mathbf{v}_{3r}) \\ z_3 \end{bmatrix}
\tag{172}
$$

where the depth component $h_{1\triangleright}$ is the solution of the following equation

$$
\xi(h_{1\triangleright}, \mathbf{v}) \equiv \xi_{2r}\left(Y(\mathrm{a}_2(h_{1\triangleright}), \mathrm{c}_2(h_{1\triangleright})), \mathbf{v}_{2r}\right) + \xi_{3r}\left(Y(\mathrm{a}_3(h_{1\triangleright}), \mathrm{c}_3(h_{1\triangleright})), \mathbf{v}_{3r}\right) -
$$
$$
\left(\frac{r}{\omega_2} + \frac{1-r}{\omega_3}\right)\xi_{1l}(h_{1\triangleright}, \mathbf{v}_{1l}), h_{1\triangleright} > h_{1o}^{lm}
\tag{173}
$$

where, the depth component h_{1o}^{lm} is the maximum depth value of the left locus curve given by Equation (40).

Proof

Here, we deduce the proof of the theorem 3.3.6 as follows:

The valid junction branches that determine the subcritical states are J_{1-} and J_{2-} such that Equations (169) and (104) are true. The mass conservation at the junction as well as the subcritical flow condition must be satisfied. Geometrically, the discharge components $q_{2\triangleright}^{lm}$ and $q_{3\triangleright}^{lm}$ must be also located above the right locus curves τ_{2r} and τ_{3r}, respectively. Indeed, from Lemma 2.4.1 and Lemma 3.3.5 the junction curves J_{2-} and J_{3-} intersect with the locus curves τ_{2r} and τ_{3r} at unique points. These points give the intermediate states $\mathbf{v}_{2*}$ and $\mathbf{v}_{3*}$ of

the Riemann solution. Furthermore, the intermediate states satisfy the subcritical condition and the mass conservation such that the following relationships are obtained

$$h_{2*} = Y(a_2(h_{1\triangleright}), c_2(h_{1\triangleright})); \quad \xi_{2r}(h_{2*}, \mathbf{v}_{2r}) = \left(\frac{r}{\omega_2}\right)\xi_{1l}(h_{1\triangleright}, \mathbf{v}_{1l}) \tag{174}$$

$$h_{3*} = Y(a_3(h_{1\triangleright}), c_3(h_{1\triangleright})); \quad \xi_{3r}(h_{3*}, \mathbf{v}_{3r}) = \left(\frac{1-r}{\omega_3}\right)\beta_{1l}(h_{1\triangleright}, \mathbf{v}_{1l}) \tag{175}$$

$h_{1\triangleright} > h_{1o}^{lm}$ belongs to the junction curve for any depth component and combining Equations (174)–(175) together, we obtain

$$\xi_{2r}\left(Y(a_2(h_{1\triangleright}), c_2(h_{1\triangleright})), \mathbf{v}_{2r}\right) + \xi_{3r}\left(Y(a_3(h_{1\triangleright}), c_3(h_{1\triangleright})), \mathbf{v}_{3r}\right) -$$
$$\left(\frac{r}{\omega_2} + \frac{1-r}{\omega_3}\right)\xi_{1l}(h_{1\triangleright}, \mathbf{v}_{1l}) = 0, h_{1\triangleright} > h_{1o}^{lm} \tag{176}$$

Therefore, the depth component $h_{1\triangleright}$ is determined by finding the root of the following function

$$\xi(h_{1\triangleright}, \mathbf{v}) \equiv \xi_{2r}\left(Y(a_2(h_{1\triangleright}), c_2(h_{1\triangleright})), \mathbf{v}_{2r}\right) + \xi_{3r}\left(Y(a_3(h_{1\triangleright}), c_3(h_{1\triangleright})), \mathbf{v}_{3r}\right) -$$
$$\left(\frac{r}{\omega_2} + \frac{1-r}{\omega_3}\right)\xi_{1l}(h_{1\triangleright}, \mathbf{v}_{1l}), h_{1\triangleright} > h_{1o}^{lm} \tag{177}$$

Furthermore, the intermediate state $\mathbf{v}_{1*}$ in the Riemann solution is determined by

$$\mathbf{v}_{1*} = \begin{bmatrix} h_{1*} \\ q_{1*} \\ z_1 \end{bmatrix} = \begin{bmatrix} h_{1\triangleright} \\ \xi_{1l}(h_{1\triangleright}, \mathbf{v}_{1l}) \\ z_1 \end{bmatrix} \tag{178}$$

In fact the junction curves J_{1-}, J_{2-} and the locus curves τ_{2r}, τ_{3r} intersect if and only if the states $\mathbf{v}_{2\triangleright}^{lm}$ and $\mathbf{v}_{3\triangleright}^{lm}$ are located above the locus curves τ_{2r} and τ_{3r}, respectively. If the state $\mathbf{v}_{2\triangleright}^{lm} \in \tau_{2r}$ and the state $\mathbf{v}_{3\triangleright}^{lm} \in \tau_{3r}$, the Riemann intermediate states are determined through non-valid states due to Lemma 2.4.1. Lemma 2.4.1 shows that $\mathbf{v}_{1o}^{lm}$ is a critical state. Hence, the conditions in Equations (169)–(104) must be satisfied to have the subcritical solution. Finally, the proof ends here while the same results can be obtained if we start from any given right state to deduce the left states in case of a network of two ingoing branches and one outgoing branch. Therefore, it is important to stress that the theorem is valid for both confluence and diffluence networks. Also, the theorem can be applied to a large network of N number of branches. ∎

3.4. Numerical examples

In this part, we numerically investigate the theoretical findings of the Riemann solution in channel networks. A vast set of examples with different initial conditions are considered to clarify the necessary conditions for the solution to be existing or not, either unique or not. Furthermore, the numerical results are

given for the Riemann solution in a simple channel network of three non-identical branches (one ingoing channel and two outgoing channels). All the solution components (*i.e.*, depths and discharges) are plotted in the phase plane $h-q$. In addition to that, the depth and the discharge components are also given in the phase planes $h-x$ and $q-x$ after a certain time. To be more organized, we present the numerical results for both symmetric and non-symmetric channel network. Width contractions ω and bottom discontinuities z are considered for the non-symmetric network only as a state of the art in the current framework. However, the examples are limited to a simple network for simplicity of presentation. In all examples, the discharge ratio r is determined through the nonlinear system (84)–(89). The system is numerically solved by using the hybrid method as explained in [46] that is based on the Newton iteration procedure. Thus, the contraction ratio ω is priorly defined. This implies that r is only determined if the system (84)–(89) admits a solution. The computed value of r is considered. If the system (84)–(89) admits no solution, the discharge ratio r is chosen for clarification.

3.4.1. Example

Consider the initial Riemann states

$$\mathbf{v}_{1l} = \begin{bmatrix} 1.5 \\ 1.0 \\ 0 \end{bmatrix}, \quad \mathbf{v}_{2r} = \begin{bmatrix} 1.7 \\ 0.8 \\ 0 \end{bmatrix}, \quad \mathbf{v}_{3r} = \begin{bmatrix} 1.7 \\ 0.8 \\ 0 \end{bmatrix} \tag{179}$$

for the symmetric channel network with a downstream flow characterized by equal width and equal discharge (*i.e.*, $b_1 = b_2 = b_3 = 1$m, $z_1 = z_2 = z_3 = 0$, and $q_2 = q_3$), where the discharge ratio $r = 0.5$ by the symmetry of the downstream flow.
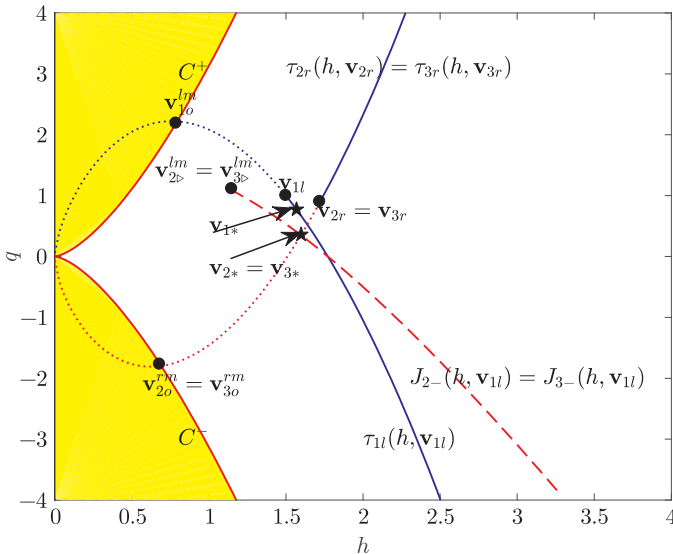

Figure 13. $q-h$ phase plane for symmetric channel network without bottom discontinuities for given initial states by Example 3.4.1
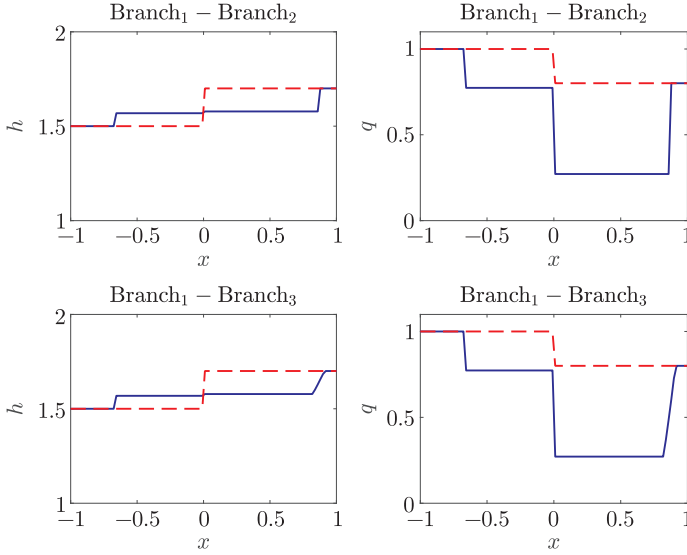
Figure 14. Water depth h and flow discharge q profiles evolve at $t = 0.2$ s for a symmetric channel network without bottom discontinuities for given initial states by Example 3.4.1

Figure 13 shows the Riemann solution for a symmetric flow in a star channel network of equal width and length with a continuous bottom. The intermediate states are given $\mathbf{v}_{1*}$, $\mathbf{v}_{2*}$, and $\mathbf{v}_{3*}$. We notice that the states $\mathbf{v}_{2*}$ and $\mathbf{v}_{3*}$ are coincided due to the symmetry of the downstream flow. It is noticed that the intermediate states $\mathbf{v}_{2*} = \mathbf{v}_{3*}$ are computed through the intersection of the junction curves J_- (dashed line) and the right locus curves τ_{2r}-τ_{3r} (dotted-solid lines). Whilst, the state $\mathbf{v}_{1*}$ is the corresponding state on the left locus curve τ_{1l}. Hence, the Riemann solution is demonstrated by the outgoing left shock (solid line) that connects the unperturbed initial state $\mathbf{v}_{1l}$ and the intermediate state $\mathbf{v}_{1*}$ (perturbed state) for the inflow channel (first channel). The unperturbed initial states $\mathbf{v}_{2r} = \mathbf{v}_{3r}$ are likely connected to the perturbed states $\mathbf{v}_{2*} = \mathbf{v}_{3*}$ through the outgoing right rarefaction (dotted lines) for the outflow channels (second and third channel). Here, the condition given by Equation (169) is fulfilled. In Figure 14, we demonstrate the time evolution of the depth and discharge profiles after the time elapse $t = 0.2$ s in the space domain $[-1, 1]$. The Riemann solution is shown in the solid lines. The dashed lines represent the initial data profiles. The perturbed states satisfy the mass-energy conservation at the junction. The Riemann solution consists of the left outgoing shock occurring at the inflow channel where $x < 0$ and the outgoing rarefaction occurring in the outflow channels such that $x > 0$. In the next examples, we justify theorem 3.3.6 by demonstrating the effect of the backward bottom discontinuities and the width contraction in the Riemann solution.

3.4.2. Example

Consider the following initial states with small backward bottom discontinuities $z_1 > (z_2, z_3)$ and the computed $r = 0.76$. The channels width are chosen such that $b_1 = 1\text{m}$, $b_2 = 0.9\text{m}$, and $b_3 = 0.5\text{m}$.

$$\mathbf{v}_{1l} = \begin{bmatrix} 1.2 \\ 1.3 \\ 0.15 \end{bmatrix}, \quad \mathbf{v}_{2r} = \begin{bmatrix} 1.3 \\ 0.4 \\ 0 \end{bmatrix}, \quad \mathbf{v}_{3r} = \begin{bmatrix} 1.8 \\ 0.35 \\ 0 \end{bmatrix} \tag{180}$$

Figure 15 shows the Riemann solution in a non-symmetric channel network with small backward bottom discontinuities. The junction curves are shown in dashed lines. They intersect with the locus curves (dotted-solid lines). The perturbed states are shown by $\mathbf{v}_{1*}$, $\mathbf{v}_{2*}$, and $\mathbf{v}_{3*}$. v_{1*}, v_{2*}, and v_{3*} are connected
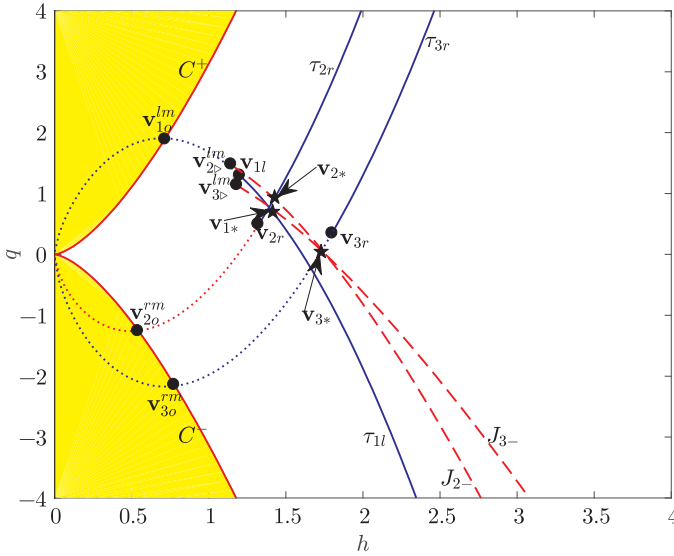

Figure 15. The Riemann solution with small backward bottom discontinuities (*e.g.*, $z_1 = 0.15\text{m}$, $z_2 = z_3 = 0$) and with the computed $r = 0.7$ for given initial states by Example 3.4.2

to the unperturbed initial states $\mathbf{v}_{1l}$, $\mathbf{v}_{2r}$, and $\mathbf{v}_{3r}$ through the outgoing left shock (solid-line) for the inflow channel, the outgoing right shock (solid-line) for the second channel, and the right rarefaction (solid-line) for the third channel, respectively. Here, the Riemann solution exists and is unique since Equation (169) is fulfilled. r and ω satisfy Equation (104). Towards better understanding of the Riemann solution, Figure 16 shows the time evolution of the depth and discharge profiles after the time elapse $t = 0.2\text{s}$. The Riemann solution is shown by the solid lines. The initial states are in the dashed lines. Two kinds of waves are noticed, the shock wave occurs in the first channel for $x < 0$ and in the second channel for $x > 0$. The rarefaction wave occurs in the third channel for $x > 0$.
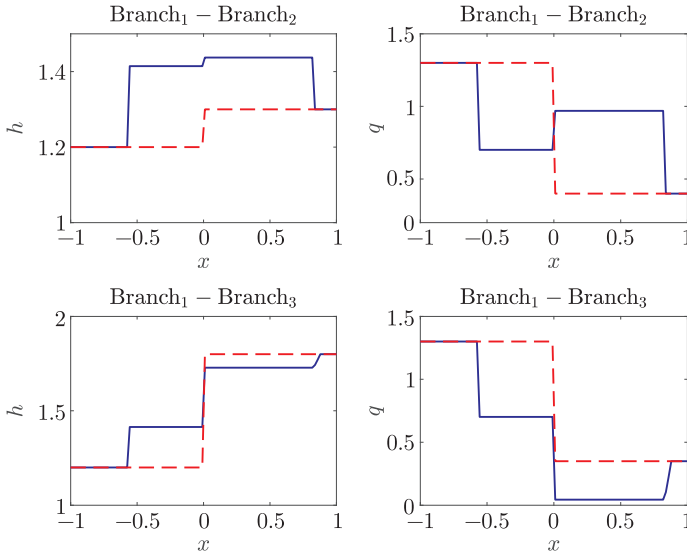
Figure 16. Water depth h and flow discharge q profiles evolve at $t = 0.2$s for symmetric channel network with bottom discontinuities (*e.g.*, $z_1 = 0.15$m, $z_2 = z_3 = 0$) for given initial states by Example 3.4.2

3.4.3. Example

Consider the following initial states with large backward bottom discontinuities and discharge ratio $r = 0.7$. The channels widths are $b_1 = 1$m, $b_2 = 0.9$m, and $b_3 = 0.5$m.

$$\mathbf{v}_{1l} = \begin{bmatrix} 1.2 \\ 1.3 \\ 1.0 \end{bmatrix}, \quad \mathbf{v}_{2r} = \begin{bmatrix} 1.3 \\ 0.4 \\ 0.0 \end{bmatrix}, \quad \mathbf{v}_{3r} = \begin{bmatrix} 1.8 \\ 0.35 \\ 0.0 \end{bmatrix} \tag{181}$$

Figure 17 shows that the Riemann solution does not exist while the condition by Equation (169) is violated and there is no intersection between the junction curves and the right wave curves. This situation is analogue to the cascade of water falling from height [47]. It is formed when the river steam flows over a steep incline, and therefore there is no physical connection between the left and right states. Thus, the flow is highly accelerated. Here, the backward bottom step minimizes the region of the Riemann solution existence.

In the following examples, we demonstrate the effect of the forward bottom discontinuities on the Riemann solution.

3.4.4. Example

Consider the following initial states with small forward bottom discontinuities $(z_2, z_3) > z_1$ such that the computed discharge ratio $r = 0.7$. The channels widths are $b_1 = 1$m, $b_2 = 0.9$m, and $b_3 = 0.5$m.

$$\mathbf{v}_{1l} = \begin{bmatrix} 1.2 \\ 1.3 \\ 0.0 \end{bmatrix}, \quad \mathbf{v}_{2r} = \begin{bmatrix} 1.3 \\ 0.4 \\ 0.15 \end{bmatrix}, \quad \mathbf{v}_{3r} = \begin{bmatrix} 1.8 \\ 0.35 \\ 0.15 \end{bmatrix} \tag{182}$$
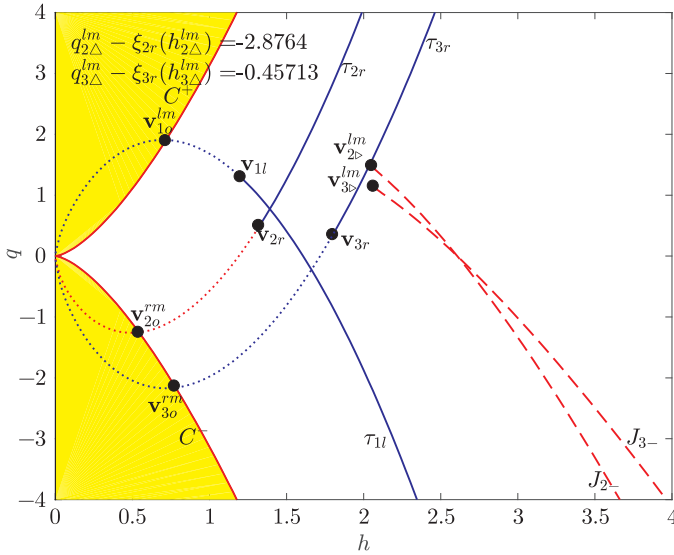
Figure 17. Non-existing Riemann solution with large backward bottom discontinuous (*e.g.*, $z_1 = 1.0$m, $z_2 = z_3 = 0$) and $r = 0.7$ for initial states given in Example 3.4.3
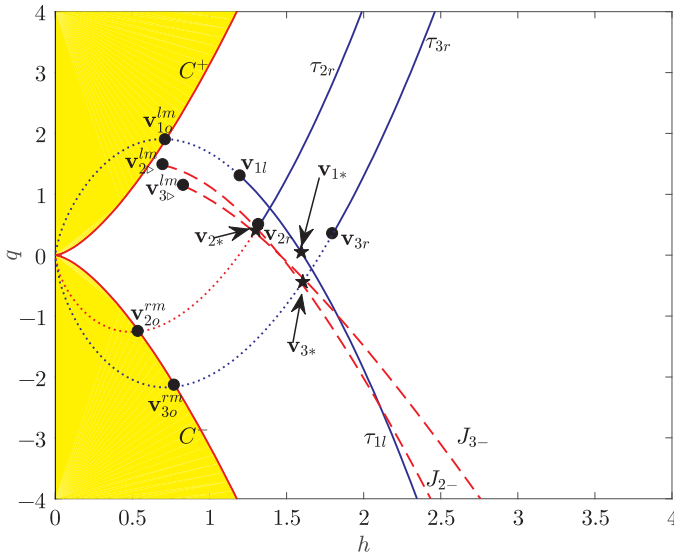

Figure 18. Riemann solution states with small forward bottom discontinuities (*e.g.*, $z_1 = 0.0$, $z_2 = z_3 = 0.15$m) and computed $r = 0.7$, initial states are given in Example 3.4.4

In Figure 18, we demonstrate that the Riemann solution exists under small forward bottom discontinuities supported by the fulfillment of the conditions given by Equations (104)–(169). It is also clear that the Riemann solution consists of the left outgoing shock, connecting the left unperturbed state and the first perturbed state in the inflow channel. Two right outgoing rarefactions connect the right unperturbed states and the second and third perturbed states. Furthermore,
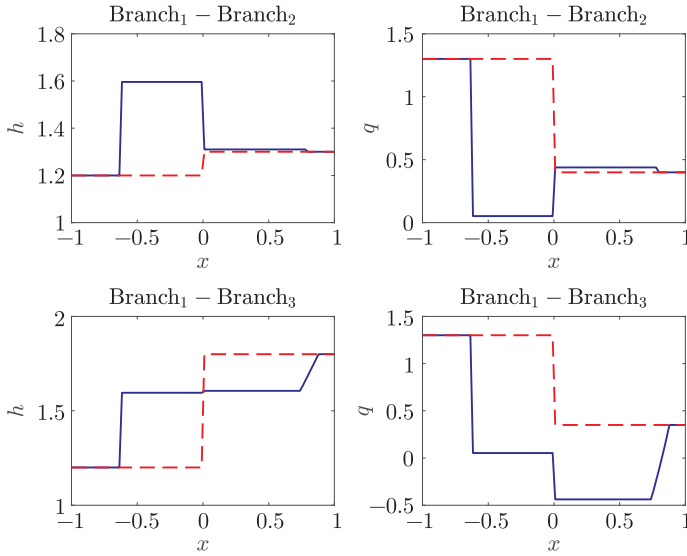
Figure 19. Depth and discharge profiles evolution of Riemann solution in non-symmetric channel network with small forward bottom discontinuities (*e.g.*, $z_1 = 0.0$, $z_2 = z_3 = 0.15\,\mathrm{m}$) after time elapsed $t = 0.2\,\mathrm{s}$

Figure 19 illustrates that the depth and the discharge profiles evolve after the time elapse $t = 0.2\,\mathrm{s}$. The structure of the solution is more clear in the finite domain x.

3.4.5. Example

Consider the following unperturbed initial states with large forward bottom discontinuities such that the discharge ratio $r = 0.7$. The channels widths are $b_1 = 1\,\mathrm{m}$, $b_2 = 0.9\,\mathrm{m}$, and $b_3 = 0.5\,\mathrm{m}$.

$$\mathbf{v}_{1l} = \begin{bmatrix} 1.2 \\ 1.3 \\ 0.0 \end{bmatrix}, \quad \mathbf{v}_{2r} = \begin{bmatrix} 1.3 \\ 0.4 \\ 0.4 \end{bmatrix}, \quad \mathbf{v}_{3r} = \begin{bmatrix} 1.8 \\ 0.35 \\ 0.4 \end{bmatrix} \tag{183}$$

Figure 20 shows that there is no solution under the large forward bottom discontinuities such that the discriminants given by Equations (107)–(108) are violated. This leads to the supercritical flow states as well as the condition in Equation (104) fails. This is because the energy is not enough to allow the flow passing the bottom step. Even more, the transcritical flow is expected because of the forward bottom discontinuities. In other words, the flow is choked [16]. Finally, the examples justify theorem 3.3.6.

3.5. Summary and conclusion

In this section we study the well-posed Riemann problem in open channel networks. Based on mathematical analysis (*e.g.* existence and uniqueness) and physical interpretation, we provide the necessary conditions to plot the Riemann solution. The solution is present assuming a non-special hypothesis (geometric configurations or symmetric flow). The subcritical flow condition is supposed
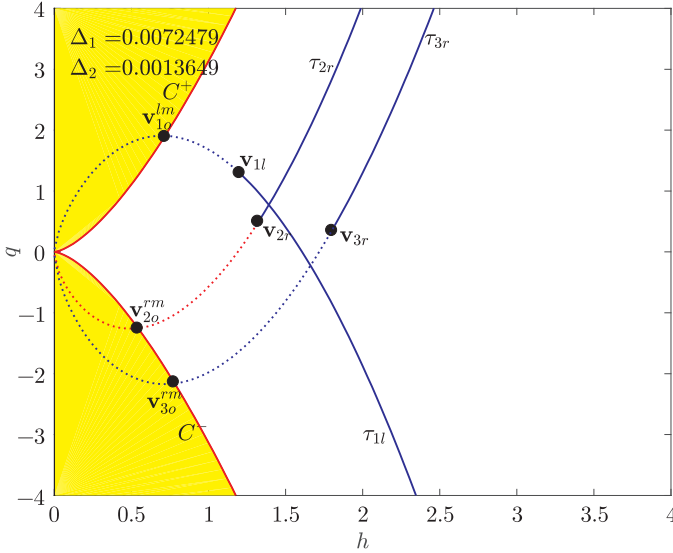
Figure 20. Non-existing Riemann solution present with large forward bottom discontinuities (*e.g.*, $z_1 = 0.0$, $z_2 = z_3 = 0.4$m) and $r = 0.7$, for given initial states in Example 3.4.5

to preserve the hyperbolicity of the PDE system. The analysis is challenged by the presence of bottom discontinuities and the channel width contraction at the junction. Taking into account the mass and the total head at the junction, we investigate the domain of existence of the Riemann solution. There are relationships involving the bottom discontinuities, the width contraction ratio, and the discharge ratio. Furthermore, the relationships between the physical quantities across the rarefaction and the shock waves complete the analysis of the domain of existence. Each stage of the solution is highlighted in association to the physical meaning. We conclude the results in the theorem. This theorem shows that the Riemann solution in a channel network junction is guaranteed by the energy and mass conservation conditions under suitable initial conditions. The solution does not exist if the subcritical flow condition is violated. Where the supercritical flow is not treated. The greatest advantage of this theorem is the possibility to apply the Riemann solution to provide the inner boundary conditions for 1D simulations in open channel networks (confluence and diffluence with the N number of branches). A vast set of examples are numerically performed to clarify the theorem. The examples start by the symmetric case that has been investigated in [43] and end by the non-symmetric case that is extended in this section. The effects of the channel width contraction, the discharge ratio, and bottom discontinuities on the Riemann solution are demonstrated under the conditions in the theorem 3.3.6. In some examples there are no solutions due to the breach of the necessary condition in Equation (169) or because of the violation of the subcritical flow conditions in Equations (105)–(106). Coping with such limitations can be considered as the subject matter of future work. In the next section we validate the Riemann solution against other models to have a full insight into the

theorem applications. This will allow us to have a consistent model and discover how convenient the Riemann solution for real applications is.

4. Applications of Riemann problem in channel networks

4.1. Introduction

Channel networks are found in natural river basins, irrigation and drainage canals, and urban water treatment plants. In addition to the complexity of the flow in a single channel, a network junction node poses more complexity to understand the network flows. In particular, the junction flow is fundamentally important in hydraulic engineering as well as in computational fluid dynamics.

Due to a large scale of natural networks, the use of 2D or 3D simulations seems to be numerically expensive with excessive operating time costs. Therefore, the 1D simulation is probably still the best choice to understand the network flows. It is mainly the 1D-SWE that are used to describe natural flows [15] as the water depth is small enough compared to the horizontal length scale in rivers and channels. The 1D-SWE are the simplest model to study the natural flow in networks. However, there are mathematical difficulties appearing challengeable to solve the 1D-SWE system in a junction network. Indeed, special attention at the junction is necessary to avoid falsifying the numerical scheme. There are two methods to tackle such difficulties in the literature. The first method has been extensively used by engineers based on some conditions. These conditions meet the flow physics [8, 48, 9, 37, 49, 10, 11, 40, 12]. The second method was provided by mathematicians based on the harmony between mathematical theories and the flow physics. The hyperbolic theory is applied in parallel to the conservation laws [17, 19, 22, 24, 4, 26, 25, 43].

[8] carried out an experiment to study the increased water level at the junction. In this study, the channels are of equal widths and zero slopes. Additional assumptions are added. The friction forces are negligible. The hydrostatic pressure distributions are assumed. The water levels upstream of the junction are equal. The velocities are uniformly distributed over all the network cross-sections. By applying the momentum and continuity equations over the control volume containing the junction, the 1D equation was obtained to predict the depth ratio (upstream to downstream). The results were verified by [8] for the junction angle of 45°.

Later on, [48] carried out a similar study for junction angles of 30°, 60°, and 90°. Based on assumptions that were slightly different from those made in [8], [9] verified the condition of the energy levels equality at the junction node. The equality of energy levels is simplified to the equality of water levels under a small velocity head. This model is given here by the Equality model taken from [9]. Further studies were conducted by [10]. The main flow characteristics are investigated. The flow is supposed to be subcritical everywhere. The energy and momentum balances are applied over the control volume in a model similar to [8]. The energy and momentum correction factors are equal to unity. The outcome

model is given here by the Gurram model. This model is used to predict the water depth ratio at the junction. Similarly and under the same assumptions as in [10], [11] applied the momentum and energy balances. The energy and momentum losses are considered by introducing energy and momentum correction factors. These factors were computed in previous experiments by [11] for 30°, 45°, and 60° junction angles and by [40] for the 90° junction angle. The outcome model is given here by the Hsu model. The Hsu model is used to predict the water depth ratio at the junction. Lastly, [12] introduced a general nonlinear formulation of the momentum and continuity equations. The assumptions of the channel depth equality and the channel width equality at the junction node are removed. However, the Shabayek model implies the use of two empirical coefficients. These coefficients require further characterization as stated by [50]. Therefore, they are excluded. The previous models belong to the same category (classical models). The classical models have been deduced by engineers for a network of three rectangular channels. The network consists of three branches and a single junction. Different junction angles are considered. The flow is supposed to be subcritical everywhere in the network. As for the supercritical flow in a channel network, [37] deduced a mathematical model to predict the water depth ratio at the junction. However, the Rice model is not included in our work as the model was derived for the supercritical flow case. Going back to the classical models in the subcritical flow domain, the characteristic and mass conservation equations are used to close the system at the junction in the 1D numerical simulations. The characteristic equations are heavily presented in [39]. They are extended in [51] to be a generic solution of the SWE. The mass conservation equation is fairly explained in [13, 15] where the physical aspects of the water flow are covered. In this paper, the classical models are the Equality, Gurram, and Hsu models. They are used to supply the conditions at the junctions for the purposes of numerical simulations.

Due to the absence of further mathematical evidence of the classical models, an alternative method has been extensively discussed by mathematicians to provide the conditions at the junction. Starting from the well posed Riemann problem in networks, [24] proved the well posed Riemann problem for the p-system at an ideal junction. The results are justified for the Euler system in the standard case. Two years later, [26] proved the existence and the uniqueness of the Cauchy problem solution for a 2×2 system of conservation laws at the junction. In particular, [25] extend the 1D Euler model to define the junction. The Cauchy problem is proved to be well posed. The outcome model describes the non-viscous isotropic or isothermal fluid across the junction [25]. Later on, [43] proved the existence and uniqueness of the Riemann problem solution of the 1D-SWE in an ideal junction network. The flow is supposed to be subcritical everywhere. The flow is symmetric in the downstream channels. It is worth mentioning that the hyperbolic theories developed in [17, 19, 22, 4] prepared to a large extent the grounds for [43] findings. However, the Riemann solution for an ideal network is limited. There is no physical meaning of the solution. Recently, [52] have extended

the Riemann solution of the 1D-SWE for the general junction network despite the symmetry assumed in [43]. Thus, the physical meaning of the solution stages is given. The necessary conditions are the fulfillment of the energy dissipation concept and the non-transition state of the flow. Therefore, the entropy condition is used to select the proper wave to pass through the junction. Furthermore, the Riemann solution has an additional advantage which allows the bottom discontinuities at the junction node.

As previously explained, there are two approaches to supply the junction conditions in 1D numerical simulations of channel networks. The first approach is defined by the classical models. The classical models have been well studied in many works. The Equality, Gurram, and Hsu, Shabayek models have been investigated for both steady and unsteady flows in junction networks by [7]. [7] demonstrate that the Equality model has poor momentum conservation at the junction. The Froude number (Fr) is greater than 0.35. Also, [7] demonstrate that the junction angle δ (the angle between the main and lateral channels) is shown to be of less influence than the downstream Froude number (Fr) on the junction flow. However, the results in [7] are only given for the asymmetrical confluence [53], where a flume with a concordant bed (*i.e.*, the bed is continuous at the junction with the same level in all channels) and a straight main channel are considered. Therefore, the [7] study ignored the effect of the bottom discordance and other types of confluences and diffluences such as symmetrical confluence (*i.e.*, Y-shaped) [53]. Indeed, the behavior of the classical models is doubtful and it is not complete in the literature. It is also noticed that the classical models are not mathematically easy to investigate. In particular, the existence and uniqueness of the solutions of classical models are hard to investigate. The second approach is the Riemann model. The Riemann model is tested firstly and only by [29] for an ideal unsteady flow case. However, there are still many issues concerning the behavior of the Riemann model missing in the literature. In this thesis, a complete revision of the junction models being either the classical models or the Riemann model is presented. We include most of the experiments in the literature to evaluate the junction models. The advantages and disadvantages of each model are well stated.

Many experiments concerning the junction flow in a network have been found in the literature. A selective set of these experiments with sufficient diversity is considered. [11, 40] performed experiments to determine the characteristics of the flume flow. The flume consists of three rectangular channels. The flow is considered to be subcritical and steady. The bottom friction is neglected. The junction angle δ is ranging from 30° to 90°. Another steady flow experiment in flume was conducted by [50] for the junction angle δ equal to 30° and 60° with a small bottom slope. The channel bottom is flat. In other words, the bed is a concordant. A different experiment examines the effect of the bed discordance on the junction flow by [54, 55]. The flow field at the confluence is affected by the bed discordance (*i.e.*, the bed level is not the same in all channels and is discontinuous at the confluence) between lateral and mainstream channels. In

the previous experiments, the networks were asymmetrical. A different type of networks was found in nature where the network was symmetric such as the Y-shaped confluences. Therefore, the experiments by [56, 57] were performed to study the junction flows in such confluences. The bed is discordance using the available experimental data, the junction models are validated through the analytical solutions provided in [52] for the unsteady flows in the junction network. Technically, a hybrid method to solve the nonlinear systems [46] is used as a compulsory step to the numerical simulations. Here, the nonlinear systems are the junction models.

The 1D-SWE are numerically solved to perform the numerical simulations that correspond to previous experiments. Different numerical methods, such as the finite difference method (FDM), the finite element method (FEM), or the finite volume method (FVM) can be used to numerically solve the SWE; see [58, 7, 35, 36, 59] and the references therein. In addition to the Eulerian mesh based methods, the Lagrangian meshless methods are also adopted to solve the 1D-SWE; see [38] for more details and the references therein. Independently from the used numerical method, when solving the 1D-SWE in open channel networks, mathematical difficulties are found at the intersection of channels (*i.e.*, junctions) as the internal boundaries at the junction are singular points. Therefore, proper treatment of the boundaries is necessary to ensure the well-posedness of the numerical scheme [24]. The FVM is used in this thesis without any loss of generality. We consider the Dumbser Osher Toro (DOT) Riemann solver [60] to discretize the 1D-SWE of subcritical flows in open channel networks. The conditions at the internal boundaries are given by the numerical solution of one of the junction models (Equality, Gurram, Hsu, or Riemann models). The numerical scheme is based on the Fortran coding language [61].

The rest of the chapter is organized as follows: The junction models are explained in Section 4.2. In Section 4.3, the DOT Riemann solver is explained to form a numerical scheme. Next, the junction models are tested for both steady and unsteady open channel flows. The results are given in Section 4.4. The numerical results are compared to the experimental data and the analytical solutions for steady and unsteady flows, respectively. Finally, a summary and conclusion are given in Section 4.6.

4.2. Junction models

In this chapter we describe nonlinear junction models. Junction models are used to provide internal boundary conditions for numerical simulation purposes. The junction models are classified into two categories. The first category is the mathematical model that matches the flow physics which is pointed by the Riemann model [52]. The second category are the classical physical models that are derived by engineers. These models are indicated by the Equality [9], Gurram [10], and Hsu [11] models. Note that the Gurram and Hsu models are adopted here to be used in general channel networks. The Gurram and Hsu models are modified to predict the water depth ratio at the Y-shaped confluence

(Figure 21). They are derived in Appendices A and B. Indeed, the lateral bed discordance effect on the junction flow is taken into account in the modified Gurram and Hsu models.
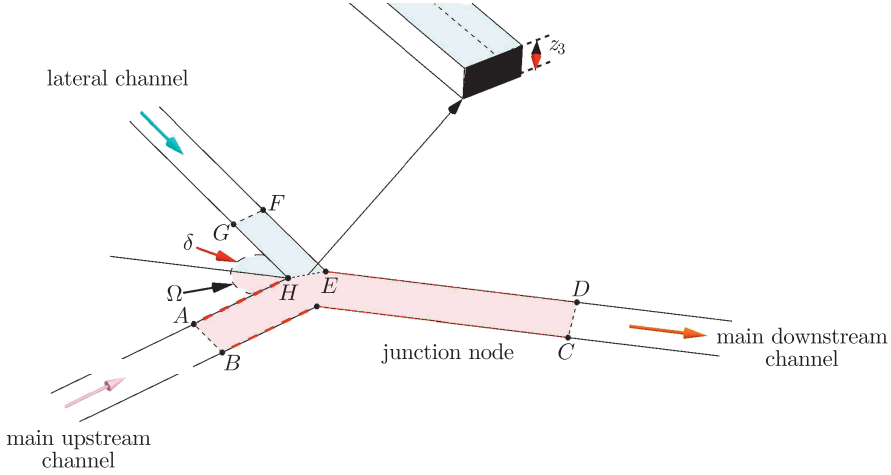

Figure 21. Y-shaped channel network with non-straight main channel

4.2.1. The Riemann model

The Riemann problem at the junction is written analogously to the classical Riemann problem in a single open channel. The classical Riemann solution is extensively described in [14] for a continuous bed and in [3, 4, 21] for a discontinuous bed. For a junction network of three rectangular channels, the Riemann problem consists of the system given in Equation (79). It is completed by the following constant initial conditions in each channel:

$$
\begin{bmatrix} h(x,0) \\ u(x,0) \\ z(x,0) \end{bmatrix} = \begin{bmatrix} h_{ok} \\ u_{ok} \\ z_k \end{bmatrix}, \, k = 1, 2, 3 \tag{184}
$$

where the indices $k = 1$, $k = 2$, and $k = 3$ specify the channel name being the main upstream channel, the lateral channel, and the main downstream channel, respectively. The unknowns (discharges and depths) at the junction node can be predicted using the Riemann solution of system (79)–(184). This method was for the first time reported by [29] in their work on ideal networks. Therefore, the Riemann model structure gives the following system:

$$
\sum_{k=1}^{3} \Pi_k b_k h_k u_k = 0, \quad k = 1, 2, 3 \tag{185}
$$

$$
\frac{u_1^2}{2g} + h_1 + z_1 = \frac{u_k^2}{2g} + h_k + z_k, \quad k = 2, 3 \tag{186}
$$

$$
u_k - u_{ok} + \Pi_k f(h_{ok}, h_k) = 0, \quad k = 1, 2, 3 \tag{187}
$$

where

$$f(h_{ok}, h_k) = \begin{cases} 2(\sqrt{gh_{ok}} - \sqrt{gh_k}), & h_k < h_{ok} \\ (h_{ok} - h_k)\sqrt{\frac{g}{2}(\frac{1}{h_{ok}} + \frac{1}{h_k})}, & h_k \geq h_{ok} \end{cases} \qquad (188)$$

(h_{ok}, u_{ok}) represent the initial states, b is the channel width. In this chapter, the channel bed heights $z_1 = z_3 = 0$, and $z_2 \neq 0$ are forming the bottom step between the second (lateral) channel and the main channels, as shown in the upper part of Figure 21. The symbolic quantity

$$\Pi_k = \begin{cases} 1, & \text{if} \quad x_k = L_k, \quad k = 1, 2, 3 \\ -1, & \text{if} \quad x_k = 0, \quad k = 1, 2, 3 \end{cases} \qquad (189)$$

specifies the inner boundary edge at the network junction. L is the length of each channel. The relationships in Equation (187) give the proper SWE wave (*i.e.*, either a shock or rarefaction wave) in each channel to pass through the junction. They are computed using the Rankine-Hugoniot conditions or the constancy of the Riemann invariants; see [14]. The continuity equation, or in other words, the mass conservation is shown by Equation (185). It must be satisfied together with the total head equality (Equation (186)) at the junction. The hypothesis of the total head and the flow discharge preservations in a single 1D open channel over the bottom step is discussed by [23, 62]. These hypotheses are also investigated by [52] for the junction network of three non-identical channels that are shown explicitly in Chapter 3.

4.2.2. The Equality model

The Equality model is considered to be the simplest model among all other junction models. It is given in the following form:

$$\sum_{k=1}^{3} \Pi_k b_k h_k u_k = 0, \quad k = 1, 2, 3 \qquad (190)$$

$$h_1 = h_2 + z_2 \qquad (191)$$

$$h_2 + z_2 = h_3 \qquad (192)$$

$$u_k h_k = A_k h_k + C_k, \quad k = 1, 2, 3 \qquad (193)$$

where $A = u_0 \pm \sqrt{gh_o}$ and $C = \mp h_o\sqrt{gh_o}$; the sign depends on the characteristic direction at the junction. Since the flow is supposed to be subcritical everywhere, then three characteristics (left and right) are involved at the junction. Equation (190) gives the mass conservation and Equations (191)–(192) fulfill the water elevation equality at the junction. These assumptions have been recognized by [9]. The energy equality at the junction is simplified to the water level equality such that the kinetic head is considered small. Equation (193) gives the characteristic equations where three relationships are obtained; see [39, 51] for more details about the characteristic SWE method.

4.2.3. The Gurram model

The Gurram formula by [10] to predict the depth ratio (h_1/h_3) at the junction was based on the momentum conservation principle. [10] assume the

water depth equality upstream of the junction. The channels are equal in width. The Gurram formula is limited to the asymmetrical channel networks of equal width and with a flat bed. Here, the Gurram formula is rather generalized to treat the discordant bed and any network configuration. More details about the derivation of the modified Gurram formula are given in Appendix A. Meanwhile, the depth and discharge unknowns at the junction are determined through solving the following nonlinear system:

$$\sum_{k=1}^{3} \Pi_k b_k h_k u_k = 0, \quad k = 1, 2, 3 \tag{194}$$

$$h_1 = h_2 + z_2 \tag{195}$$

$$\left(\frac{h_1}{h_3}\right)^3 \cos(\Omega) - \left(\frac{b_3 h_1}{b_1 h_3}\right) \left[1 + 2\mathrm{Fr}^2 - \left(\frac{2b_2}{b_3}\right)\left(\frac{h_s}{h_3^2}\right) z_2 \cos(\delta)\right] +$$
$$2\mathrm{Fr}^2 \left[\left(\frac{h_1 u_1}{h_3 u_3}\right)^2 \cos(\Omega) + \left(\frac{b_3^2 h_1}{b_1 b_2 (h_1 - z_2)}\right)\left(1 - \frac{b_1 h_1 u_1}{b_3 h_3 u_3}\right) \cos\left(\frac{8\delta}{9}\right)\right] = 0 \tag{196}$$

$$u_k h_k = A_k h_k + C_k, \quad k = 1, 2, 3 \tag{197}$$

where Fr is the main downstream Froude number. Ω is the angle between the main upstream channel and the main downstream channel as shown in Figure 21. h_s is the depth over the lateral bed step and it is computed according to [62, 52]. Equation (194) satisfies the mass conservation principle. Equation (195) is claimed by assuming the water elevation equality upstream of the junction. Equation (196) is the modified Gurram formula. Finally, Equation (197) is obtained by the characteristic equations according to [39, 51] being three relationships associated to three characteristics.

4.2.4. The Hsu model

The [11] formula is derived similarly to the Gurram formula, but the energy and momentum coefficients taken are different from unity. The depth and discharge unknowns at the junction are determined through solving the following nonlinear system:

$$\sum_{k=1}^{3} \Pi_k b_k h_k u_k = 0, \quad k = 1, 2, 3 \tag{198}$$

$$h_1 = h_2 + z_2 \tag{199}$$

$$\left(\frac{h_1}{h_3}\right)^3 \cos(\Omega) - \left(\frac{b_3 h_1}{b_1 h_3}\right) \left[1 + \frac{2\beta \mathrm{Fr}^2}{\gamma} - \left(\frac{2b_2}{b_3}\right)\left(\frac{h_s}{h_3^2}\right) z_2 \cos(\delta)\right] +$$
$$\frac{2\beta \mathrm{Fr}^2}{\gamma} \left[\left(\frac{h_1 u_1}{h_3 u_3}\right)^2 \cos(\Omega) + \left(\frac{b_3^2 h_1}{b_1 b_2 (h_1 - z_2)}\right)\left(1 - \frac{b_1 h_1 u_1}{b_3 h_3 u_3}\right) \cos(\delta)\right] = 0 \tag{200}$$

$$u_k h_k = A_k h_k + C_k, \quad k = 1, 2, 3 \tag{201}$$

where β is the momentum coefficient and γ is the energy coefficient. Equation (198) satisfies the mass conservation, while Equations (199) are claimed by setting

equal water elevation upstream of the junction. Equation (200) gives the modified Hsu formula shown in Appendix B and Equation (201) is obtained through the characteristic equations according to [39, 51].

4.3. Numerical method

A numerical method has to be used to solve the 1D-SWE in channel networks numerically. There are many methods that can be used. Since the shallow water equations system is a class of a hyperbolic conservative system, we use the Finite Volume Method (FVM). The FVM has been widely used to descretize the SWE [14]. The FVM is the numerical method to represent and convert the PDE into algebraic equations [63, 14, 18]. In the FVM, PDE are integrated and evaluated over the control volume. The integral form of the PDE contains a divergence term that is converted into the surface integral by using the divergence theorem that is known as Gauss's theorem [64]. The surface integral is evaluated through the flux at the boundaries of the cells. The most famous form of the FVM is the Godunov scheme [65]. The Godunov method is a conservative form of the FVM which requires the Riemann problem to be solved exactly or approximately at each boundary of cells. The Godunov scheme is considered to be the basis of higher order schemes. The most significant difference is the way to compute the Godunov flux. [66] present a novel approach to solve the Riemann problem approximately to evaluate the Godunov flux. The resulting Riemann solver is known as the HLL Riemann solver. It is extended by [67] and called the HLLE Riemann solver. The HLLE solver is modified by [67] and named HLLM. However, the HLL and HLLE Riemann solvers are limited to the 2×2 hyperbolic system such as the 1D-SWE. It cannot be used for a large system [14]. Later on, the HLLC solver is proposed by [68, 68] for a time dependent Euler system. Another well known Riemann solver is the Roe Riemann solver [69]. Many refinements of the Roe Riemann solver have been made over the last twenty years [14]. At the same time, the Osher Riemann solver was introduced in [70, 71]. We recommend the handbook to find more information about the progression history of the Osher Riemann solver [14]. Recently, [60] have produced the DOT Riemann solver. They were motivated by the capability of the DOT Riemann solver to solve the quasilinear PDE. Based on that, we have decided to use the DOT Riemann solver to perform the numerical simulations. The DOT Riemann solver is explained in the next subsection.

4.3.1. DOT Riemann solver

We start by integration of Equation (3) over the finite control volume. We get the following path-conservative formulation [60]:

$$\mathbf{W}_i^{n+1} = \mathbf{W}_i^n - \frac{\Delta t}{\Delta x}(\mathcal{D}_{i+\frac{1}{2}}^- + \mathcal{D}_{i-\frac{1}{2}}^+) \tag{202}$$

where the fluctuations $\mathcal{D}_{i\pm\frac{1}{2}}^\pm$ have to satisfy the compatibility condition:

$$\mathcal{D}_{i+\frac{1}{2}}^- + \mathcal{D}_{i+\frac{1}{2}}^+ = \int_0^1 \mathbf{A}(\psi(\mathbf{W}_{i+1},\mathbf{W}_i,s))\frac{\partial\psi}{\partial s}ds \tag{203}$$

$\mathbf{W}_i^n$ refers to the cell average of the non conservative variables at time t^n. The uniform spatial step is $\Delta x = x_{i+\frac{1}{2}} - x_{i-\frac{1}{2}}$ and the time step is $\Delta t = t^{n+1} - t^n$. We choose the linear integration path $\boldsymbol{\psi}(s)$ [60] in the parameter $s \in [0,1]$:

$$\boldsymbol{\psi}(s) = \boldsymbol{\psi}(\mathbf{W}^-, \mathbf{W}^+, s) = \mathbf{W}^- + s(\mathbf{W}^+ - \mathbf{W}^-) \tag{204}$$

The Osher fluctuations term becomes:

$$\mathcal{D}_{i+\frac{1}{2}}^{\pm} = \frac{1}{2}\left(\int_0^1 \mathbf{A}(\boldsymbol{\psi}(s))ds \pm \int_0^1 |\mathbf{A}(\boldsymbol{\psi}(s))|ds \right)(\mathbf{W}_{i+1} - \mathbf{W}_i) \tag{205}$$

By using the Gauss-Legendre quadrature, the analytical path integral in Equation (205) is replaced by

$$\mathcal{D}_{i+\frac{1}{2}}^{\pm} = \frac{1}{2}\left(\sum_{j=1}^G \omega_j \left[\mathbf{A}(\boldsymbol{\psi}(s_j)) \pm |\mathbf{A}(\boldsymbol{\psi}(s_j))| \right] \right)(\mathbf{W}_{i+1} - \mathbf{W}_i) \tag{206}$$

with a given G-point quadrature rule in the interval $[0,1]$. s_j is the nodes and ω_j is the weights; see [72]. Note that the DOT Riemann solver for the non-conservative form of the PDE is automatically reduced to the Osher Riemann solver for the conservative form [60], if the source term is zero. The time step must satisfy the Courant-Fredrich-Lewy stability criterion (CFL) to ensure the stability of the scheme.

$$\Delta t = \text{CFL} \frac{\Delta x}{\max(|u \pm c|)} \tag{207}$$

where $\text{CFL} < 1$ and $c = \sqrt{gh}$ is the wave celerity.

Since the computation domain is finite, the numerical scheme has to be completed with boundary conditions. Therefore, two types of boundary conditions are necessary. They are the external and internal boundary conditions. The external boundary conditions are the conditions at the inflow-outflow sections of the network. They are computed according to the nature of the flow. As we only work with the subcritical flow, each inflow boundary has two conditions. One is the physical condition as the discharge hydrograph and the second is the numerical condition such as the depth. These conditions have to be imposed at the inflow sections. The numerical condition is computed using the strategy shown in [51] that is based on the characteristic curves. Taking into account the junction models, the internal boundary conditions are the conditions at the interfaces of the junction node. They depend on the number of the segment channels at the junction. The unknowns for a network of three channels are three water depths and three water discharges. These unknowns are computed by using one of the junction models as defined in Section 4.2.

4.4. Numerical results of steady flows

In this section, we present the numerical simulations to reproduce a set of experiments that are found in the literature for steady flows. The selected experiments are chosen to include most of the natural effects such as different

junction angles, different confluences, channel contractions, and bed discordance at the junction. Therefore, the chosen experiments here are due to [54, 11, 40, 57, 50]. Each experiment is fully described in the next subsection.

4.4.1. Steady flow in asymmetrical confluence with lateral concordant bed

(1) Hsu experiments: [11] carried out experiments in a rectangular flume, Figure 21, where the angle $\Omega = 0$ and the bed heights were $z_1 = z_2 = z_3 = 0$. The lateral and main channels were 1.5 and 6 m long, respectively. The channel width was 0.155 m for both lateral and main channels. The junction angles δ were 30°, 45°, and 60°, whereas in the experiment [40], the lateral and main channels were 4 and 12 m long, respectively, the channel width was 0.155 m in both channels with the junction angle δ of 90°. The Froude number Fr was smaller than 0.7.

(2) [50] experiment: a rectangular flume as shown in Figure 21 was considered where the angle $\Omega = 0$ and the bed heights are $z_1 = z_2 = z_3 = 0$. Both the lateral and main channels were 0.30 m wide and 0.50 m deep. The main channel was 10 m long with a small bed slope of 0.141, %. The junction angles were 30° and 60°. Similarly to the Hsu experiments, the downstream Froude number Fr was smaller than 0.7.

The numerical scheme (Section 4.3) is used to reproduce the previous experiments. The scheme is equipped by the solutions of the junction models (Section 4.2). Thus, the inner boundary conditions are determined. The mean values of β and γ are taken equal to 1.12 and 1.27, respectively. However, the mean values of the momentum and energy coefficients are selected according to the suggestions provided in [11]. The relative error percentages (E) are calculated between the predicted depth ratio ($X = h_1/h_3$) and the corresponding experimental value for a quantitative comparison between the experimental results and the numerical results. Therefore, the following formula is used to compute E

$$E = \frac{|X_{exp} - X_{num}|}{X_{exp}} \times 100 \tag{208}$$

where X_{exp} refers to the experimental depth ratio (main upstream to downstream) in [11, 40, 50]. X_{num} refers to the depth ratio which is computed using either the Riemann, Equality, Gurram, or Hsu model.

Table 1. Relative error percentages in the determined depth ratio h_1/h_3 at the junction, compared to the experimental data of [11, 40]

Junction angle δ	Riemann	Equality	Gurram	Hsu
30°	2.68	10.59	3.02	0.72
45°	2.87	11.64	2.37	0.61
60°	2.88	13.02	2.48	1.27
90°	5.84	19.91	3.78	2.21

Table 2. Relative error percentages in the determined depth ratio h_1/h_3 at the junction, compared to the experimental data of [50]

Junction angle δ	Riemann	Equality	Gurram	Hsu
30°	2.83	17.84	1.54	1.64
60°	5.62	20.63	0.70	1.49

In Figure 22, the junction models are compared to the experimental data of [11, 40]. The depth ratio h_1/h_3 is plotted versus the discharge ratio Q_1/Q_3 ($Q = bhu$). The junction angles δ are 30°, 45°, 60°, and 90°. Figure 23 shows the performance of the junction models against the [50] data, where the junction angles are 30° and 60°. It is noticed that good agreement between the numerical results and the experiments is obtained, if the Riemann, Gurram, and Hsu models are used. On the contrary, The worst behavior is rendered by the Equality model. This is not surprising as the Equality model has bad performance for Fr greater than 0.35 as confirmed by [7]. And, in these experiments the Froude number Fr ranges between 0.52 and 0.7. Quantitatively, the relative error percentages are listed in Tables 1–2. The errors are corresponding to Figure 22 and Figure 23. The effect of the junction angle is also well noticed in these such Tables. As far as the results are considered, the Equality model gives the maximum error percentage (19.91%) while the Hsu model gives the minimum error percentage (0.61%) followed by the Gurram model (2.37%) and the Riemann model (2.68%). In general, the error with the Riemann model is near to the errors with the Gurram and Hsu models for the junction angles of 30°, 45°, and 60°. On the contrary, the difference increases for the 90° junction angle.

According to the current results, we can say that it is not only the momentum based junction models (the Gurram and Hsu models) the can be used with an acceptable error (less than 8%) as stated in [7], but it is also the Riemann model that gives tolerable errors. The Riemann model is classified to be an energy based model. However, the use of the momentum based junction models (the Gurram and Hsu models) is not trivial in many situations due to the empirical coefficients such as energy and momentum coefficients. These coefficients require proper calibration based on the geometry of the junction and on the characteristics of the flow dynamics. This fact is highlighted in the following subsections.

Table 3. Error percentage in computed downstream velocity u_3 relative to experimental layout of [54] approximated by TELEMAC-2D software

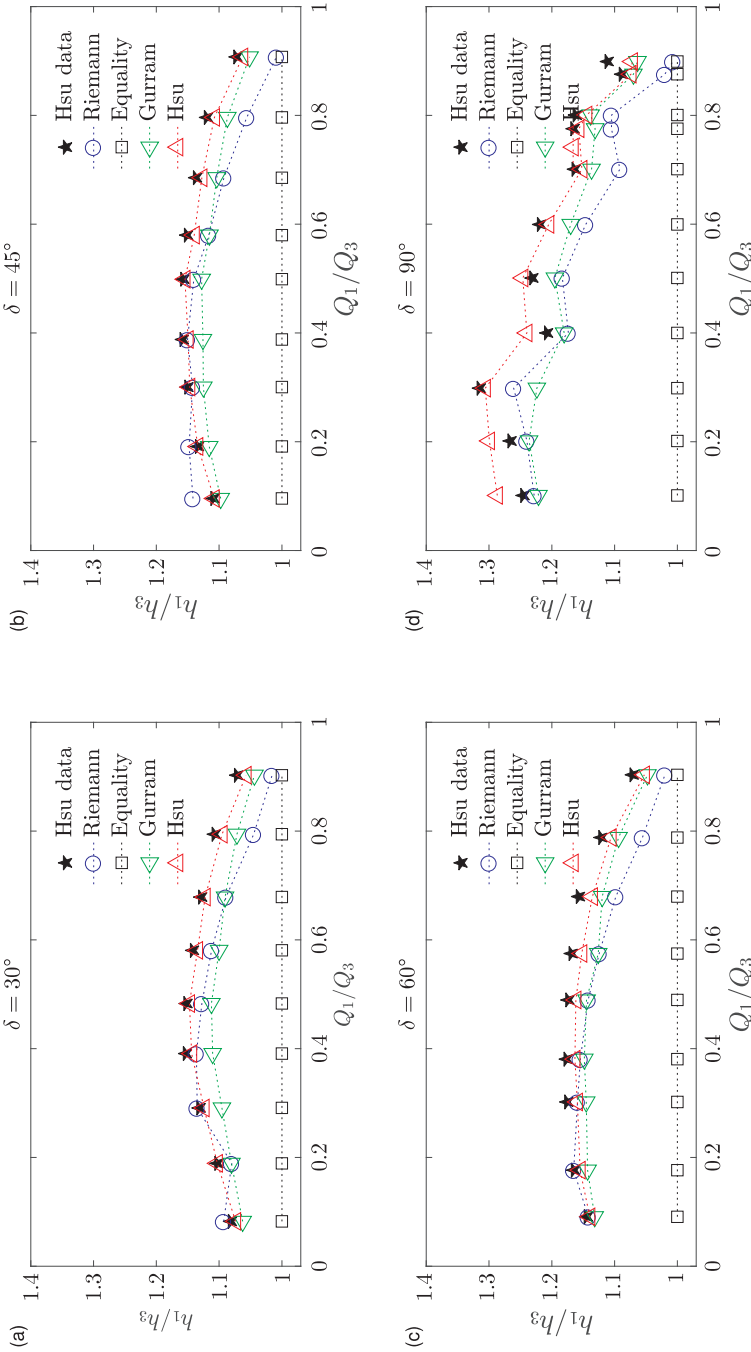| Junction model	Discordant bed
Riemann	0.60
Equality	1.78
Gurram	7.05
Hsu	5.95

Figure 22. Numerical solutions *vs.* experimental data of [11] with junction angles 30°, 45°, and 60°; and *vs.* the experimental data of [40] with junction angle 90°. The experimental data is shown in filled stars, circles, squares, triangles, and the diamond markers refer to the Riemann, Equality, Gurram, and the Hsu models, respectively
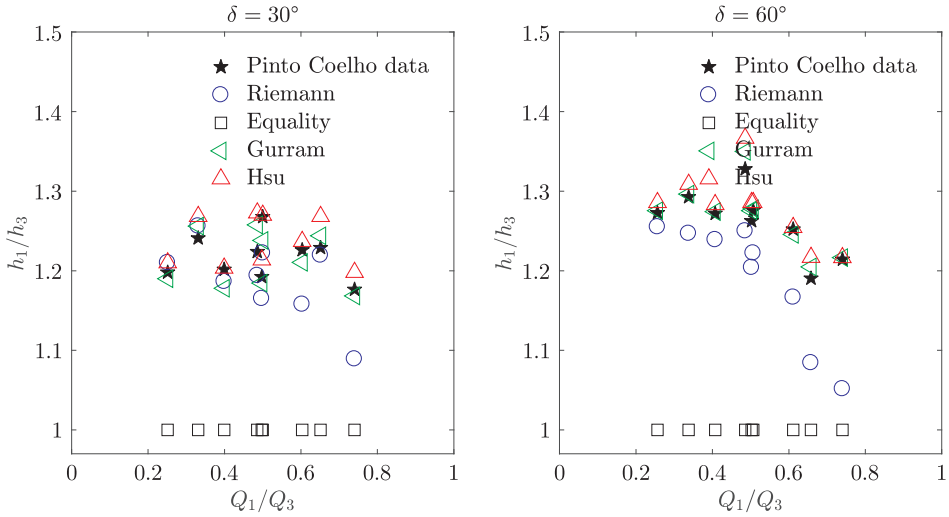
Figure 23. Numerical solutions vs. experimental data of [50] with the junction angles of 30° and 60°

4.4.2. Steady flow in asymmetrical confluence with lateral discordant bed

(1) According to [54], the discordant bed noticeably affects the flow in river confluences even with a small Froude number (*e.g.*, Fr less than 0.35). Therefore, a further study to investigate the behavior of the junction models is presented for the lateral discordant bed case. [54] carried out experiments in asymmetrical confluence such that $\Omega = 0$ and $\delta = 30°$ (Figure 21) to investigate the effects of the bed discordance on the confluence flow. The study focuses on four flow dynamics regions at the junction, *i.e.*, the flow deflection zone, the separation layer, the velocity, and the mixing layer. Following the work of [54], we consider the numerical experiment characterized by the main upstream channel, the lateral channel, and the main downstream channel. These channels are 0.12, 0.08, and 0.137 m wide and 3.5, 3.5, and 10 m long, respectively. The height of the lateral bed is 0.03 m. The Froude number Fr is less than 0.20. The discharges are $2.688 \cdot 10^{-3}$, $2.808 \cdot 10^{-3}$, and $5.496 \cdot 10^{-3}$ m^{3}s^{-1} in the main upstream, lateral, and main downstream channels, respectively. The corresponding depths are 0.16, 0.13, and 0.16 m. The discharge ratio Q_r between the main upstream channel and the lateral channel is equal to 1.04. The experimental data by [54] is not available. Therefore, the TELEMAC-2D software [73] is employed to produce a cross-section averaged in such a way that it can be used as a reference solution for 1D models. Indeed, the experiments by [54] are approximated and the corresponding 2D numerical results are averaged on a cross-section located 8 m downstream of the junction.

A significant difference between the Riemann and Equality models on the one hand, and the Gurram and Hsu models on the other hand is observed. Figure 24 shows the matching between numerical solutions and approximated experimental data of [54]. The results obtained by the Gurram and Hsu models

might be affected by specific values of the energy and momentum coefficients ($\beta = 1.12$ and $\gamma = 1.27$). However, the recalibration of such coefficients is beyond the present work that is conceived on the contrary to avoid case-dependent coefficients as much as possible. The bed discordance divides the four models into two categories: empirical (Gurram-Hsu) and non-empirical (Riemann-Equality) models. Observing the relative error behavior as listed in Table 3, the maximum error (7.05%) is obtained by the Gurram model and followed by the Hsu model (5.95%). The minimum error (0.60%) is obtained by the Riemann model followed by the Equality model (1.78%).
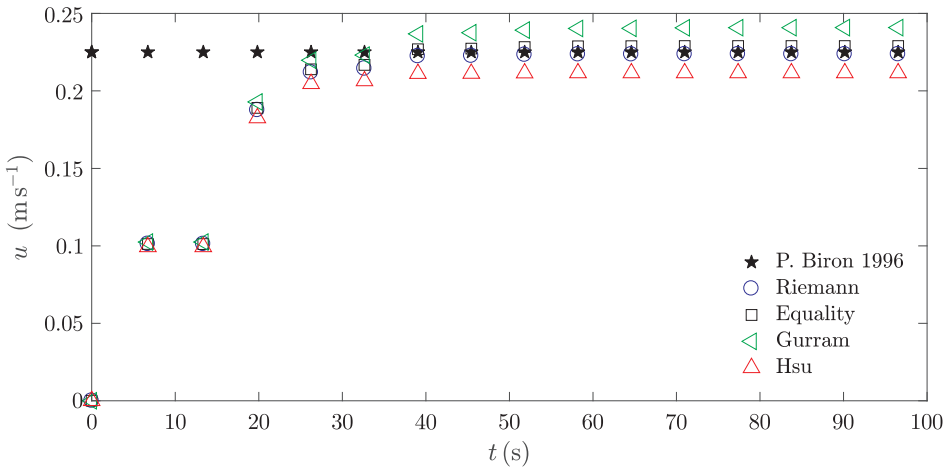

Figure 24. Four different numerical solutions for downstream velocity vs. time for discharge ratio Q_r=1.04. The experimental layout of [54] is approximated by the TELEMAC-2D software

The computations show that the momentum based junction models (Gurram and Hsu models) are hardly extendible to more general cases without tuning the empirical coefficients (β and γ) even if Fr < 0.3. The highest error value obtained by the Gurram model is very near the 8% limit of acceptability that is stated in [7]. Such limitations declare a level of weakness to the momentum based methods. For Fr < 0.35, the results disproved the [7] findings. We can observe that the Riemann model attains the best agreement with the approximated experimental layout of [54].

Table 4. Error percentage in computed downstream velocity u_3 versus experimental layout of [57] approximated by TELEMAC-2D software

Junction model	Concordant bed	Discordant bed
Riemann	1.08	2.33
Equality	6.67	7.76
Gurram	3.86	4.49
Hsu	6.19	7.23

4.4.3. Steady flow in Y-shaped confluence with lateral concordant and discordant beds

(1) The experiments performed by [57] are used to test the effect of the bed discordance on the flow at the Y-shaped confluence with $\Omega = \delta = 45°$ in Figure 21. Thus, they are used to validate the junction models. The [57] experimental data is presented in the 3D form. The TELEMAC-2D software is used to approximate the [57] experimental layout to use this data in the 1D framework. The averaged cross-section values of the downstream velocity located at 4 m are obtained downstream of the junction. These values are used to validate the 1D numerical simulations. The lateral channel is 0.3 m wide and 2.4 m long. The main channel is 0.45 m wide with 2.4 and 4.8 m long in the main upstream channel and the downstream channel, respectively. This test case is divided into two cases: the first is due to the concordant bed and the second is due to the discordant bed. For the concordant bed case (*i.e.*, $z_2 = 0$), the discharges are $3.12 \cdot 10^{-2}$, $1.68 \cdot 10^{-2}$, and $4.8 \cdot 10^{-2} \, \mathrm{m^3 s^{-1}}$ in the main upstream channel, the lateral channel, and the main downstream channel, respectively. The corresponding water depths are 0.25 m in all channels. The discharge ratio Q_r between the lateral channel and the main downstream channel is equal to 0.35. For the discordant bed case (*i.e.*, $z_2 = 0.05$ m), the discharges are $1.8 \cdot 10^{-2}$, $3.0 \cdot 10^{-2}$, and $4.8 \cdot 10^{-2} \, \mathrm{m^3 s^{-1}}$. The corresponding water depths are 0.30, 0.25, and 0.30 m with $Q_r = 0.6$.

Table 5. Initial water depth, discharge profiles, and bed heights for unsteady flow in a star network with a concordant bed at $t = 0$

Variables	Upstream main channel	Lateral channel	Downstream main channel
$h \, (\mathrm{m})$	0.5	0.5	1.0
$Q \, (\mathrm{m^3 s^{-1}})$	0.1	0.1	0.0
$z \, (\mathrm{m})$	0.01	0.01	0.01

Figures 25–26 show a comparison between the junction models in matching the reference data of [57] at the Y-shaped confluence with a concordant and discordant bed, respectively. Fr was less than 0.27 in both cases. However, a significant difference between the numerical solutions and the reference data of [57] is noticed. In particular, the Equality, Gurram, and Hsu models did not well match the reference data of [57]. The influence of the bed on the solution is noticed in Table 4. The error percentages are approximately increased by 1% comparing the discordant vs. concordant bed. The Riemann model shows the best agreement with the reference data of [57]. It is followed by the Gurram, Hsu, and Equality models, respectively.

4.5. Numerical results for unsteady flows

Junction models in unsteady flow conditions are not fully validated in the literature. Few studies only have been performed; *cf.* [74, 7, 38, 29]. Here, analytical Riemann solutions for a symmetric fluvial flow according to [43] and
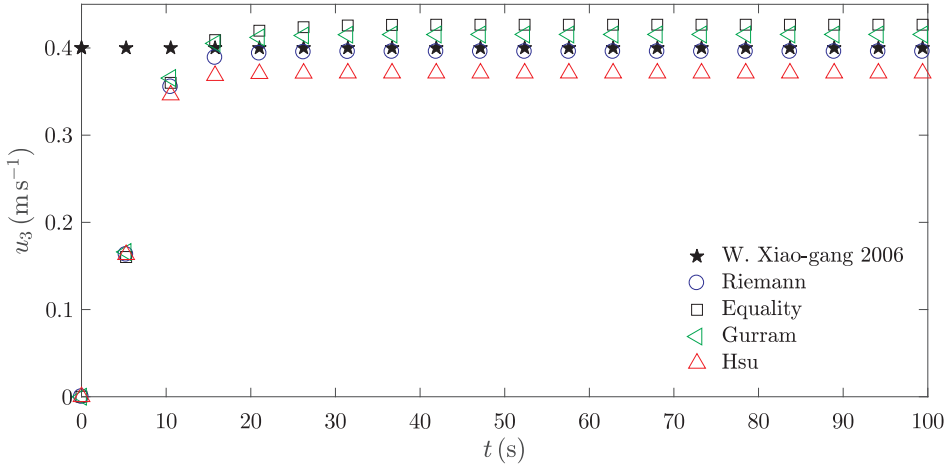
Figure 25. Numerical solutions for downstream velocity vs. time for discharge ratio Q_r=0.35. The experimental layout of [57] is approximated by the TELEMAC-2D software

Figure 26. Numerical solutions for downstream velocity vs. time for discharge ratio Q_r= 0.6. The experimental layout of [57] is approximated by the TELEMAC-2D software
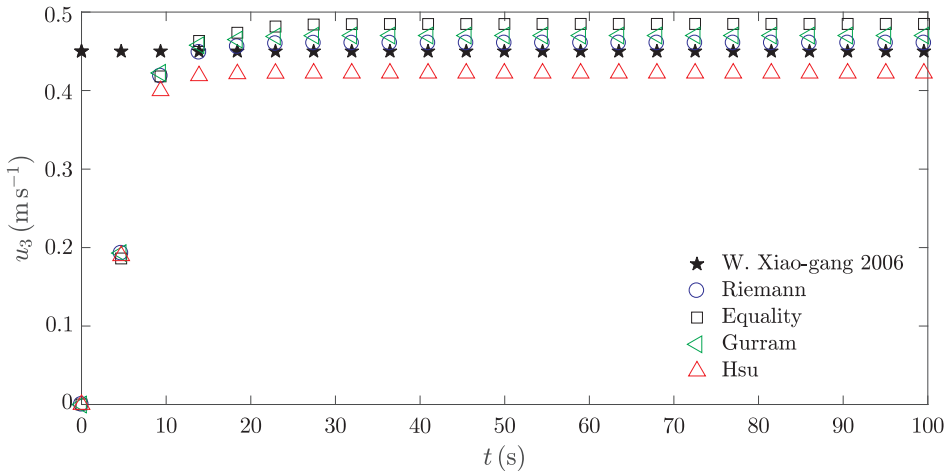
Table 6. ℓ^1 error in determined water depths with respect to analytical solutions according to [43]

Junction model	Upstream channel	Lateral channel	Downstream channel
Riemann	$1.6997 \cdot 10^{-3}$	$1.6997 \cdot 10^{-3}$	$4.2037E \cdot 10^{-3}$
Equality	$1.1143 \cdot 10^{-2}$	$1.1143 \cdot 10^{-2}$	$2.8994 \cdot 10^{-2}$
Gurram	$4.3977 \cdot 10^{-3}$	$4.3977 \cdot 10^{-3}$	$1.2914 \cdot 10^{-2}$
Hsu	$2.1425 \cdot 10^{-3}$	$2.1425 \cdot 10^{-3}$	$5.9129 \cdot 10^{-3}$

for a general fluvial flow according to [52] are used to validate the junction models discussed in Section 4.2.

4.5.1. Unsteady flows in star network with concordant bed

Consider the general network layout that is illustrated in Figure 21 such that $\Omega = \delta = 45°$. Three rectangular channels with equal width (*i.e.*, $b_1 = b_2 = b_3 = 1.0\,\mathrm{m}$) and equal length (*i.e.*, $L_1 = L_2 = L_3 = 1\,\mathrm{m}$) are connected at the junction forming a star network. The flow is assumed to go from the first and second channels (main upstream and lateral channels) to the third channel (main downstream channel).

Table 7. ℓ^1 error in determined water discharges with respect to analytical solutions according to [43]

Junction model	Upstream channel	Lateral channel	Downstream channel
Riemann	$4.2644 \cdot 10^{-3}$	$4.2644 \cdot 10^{-3}$	$8.8333 \cdot 10^{-3}$
Equality	$3.5669 \cdot 10^{-2}$	$3.5669 \cdot 10^{-2}$	$3.8996 \cdot 10^{-2}$
Gurram	$1.1279 \cdot 10^{-2}$	$1.1279 \cdot 10^{-2}$	$1.7570 \cdot 10^{-2}$
Hsu	$6.4912 \cdot 10^{-3}$	$6.4912 \cdot 10^{-3}$	$1.0272 \cdot 10^{-2}$

Thus, taking into account the given piecewise constant initial states in Table 5, we observe that the current study case is the counterpart of the dam break problem in a single open channel [14]. The unsteady simulations are performed by using the numerical scheme presented in Section 4.3. The external boundary conditions and the constant discharges are chosen upstream of the lateral and main channels. The downstream condition is the dynamic rating curve due to the subcritical flow conditions. The inner boundary conditions are supplied at each time step by solving the junction models according to Section 4.2. The spatial grid Δx is 0.02 m. The time step is computed according to Equation (207). The mesh cells number N is equal to 50 cells.

Figures 27–28 show the numerical results for the junction models (Riemann, Equality, Gurram, and Hsu models). The ℓ^1 errors for water depths and water discharges are listed in Tables 6–7, respectively. They are determined according to the following formulas:

$$e_k^h = \Delta x \sum_{i=1}^{N} |h_k^*(x_i,t) - h_k(x_i,t)|, \quad k = 1,2,3 \tag{209}$$

$$e_k^Q = \Delta x \sum_{i=1}^{N} |Q_k^*(x_i,t) - Q_k(x_i,t)|, \quad k = 1,2,3 \tag{210}$$

where h^* and Q^* are the water depths and the water discharges obtained using the analytical solutions. h and Q are the water depths and the water discharges estimated by the junction models after the time elapsed ($t = 0.2\,\mathrm{s}$). N is the mesh cell number. The best agreement between the numerical and analytical solutions is demonstrated when the Riemann model is used to supply the inner boundary conditions at the junction.
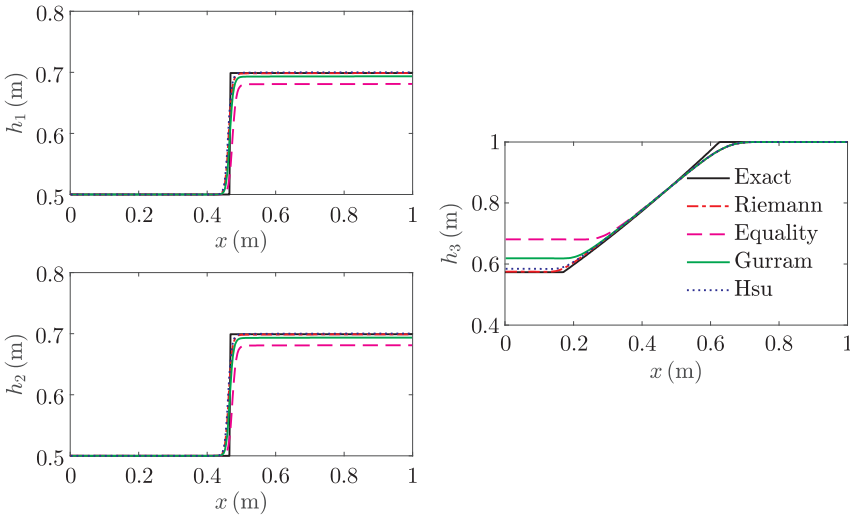
Figure 27. Evolution of water depths after time elapsed of 0.2 s. The analytical solutions [43] are shown by the black solid lines. The Riemann, Equality, Gurram, and Hsu models are shown by the dashed-dot lines, dashed lines, green solid lines, and dots, respectively

Figure 28. Evolution of water discharges after time elapsed of 0.2 s. The analytical solutions [43] are shown by the black solid lines. The Riemann, Equality, Gurram, and Hsu models are shown by the dashed-dot lines, dashed lines, green solid lines, and dots, respectively
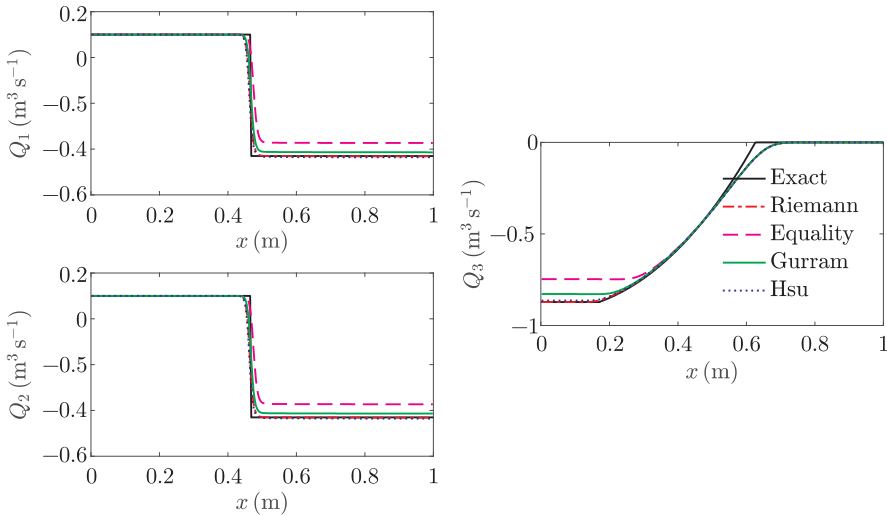
4.5.2. Unsteady flows in star network with discordant bed

By considering the initial profiles given in Table 8 and the same network setup given in subsection 4.5.1, the numerical solutions are compared to the analytical solutions according to [52]. Similarly to the previous case, the Riemann model continues to give the best results among the junction models. However,

Table 8. Initial water depth, discharge profiles and bed heights for unsteady flow in a star network with a concordant bed at $t = 0$

Variables	Upstream main channel	Lateral channel	Downstream main channel
$h\,(\mathrm{m})$	0.5	0.5	1.0
$Q\,(\mathrm{m^3 s^{-1}})$	0.1	0.1	0.0
$z\,(\mathrm{m})$	0.02	0.02	0.0

Table 9. ℓ^1 error in determined water depths with respect to analytical solutions according to [52]

Junction model	Upstream channel	Lateral channel	Downstream channel
Riemann	$2.8259 \cdot 10^{-3}$	$2.9823 \cdot 10^{-3}$	$4.4822 \cdot 10^{-3}$
Equality	$3.3888 \cdot 10^{-3}$	$1.3163 \cdot 10^{-2}$	$1.3813 \cdot 10^{-2}$
Gurram	$9.9045 \cdot 10^{-3}$	$2.4654 \cdot 10^{-2}$	$3.7784 \cdot 10^{-2}$
Hsu	$6.6270 \cdot 10^{-3}$	$2.1015 \cdot 10^{-2}$	$3.03213 \cdot 10^{-2}$

Table 10. ℓ^1 error in determined water discharges with respect to analytical solutions according to [52]

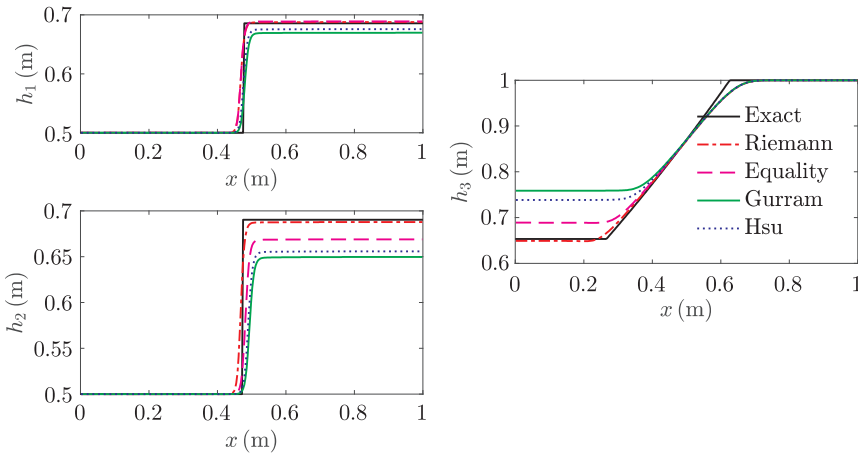| Junction model	Upstream channel	Lateral channel	Downstream channel
Riemann	$8.3438 \cdot 10^{-3}$	$7.7162 \cdot 10^{-3}$	$1.0197 \cdot 10^{-2}$
Equality	$1.0211 \cdot 10^{-2}$	$4.0485 \cdot 10^{-2}$	$2.3116 \cdot 10^{-2}$
Gurram	$3.0104 \cdot 10^{-2}$	$7.4928 \cdot 10^{-2}$	$6.5073 \cdot 10^{-2}$
Hsu	$1.9684 \cdot 10^{-2}$	$6.4204 \cdot 10^{-2}$	$5.1050 \cdot 10^{-2}$

Figure 29. Evolution of water depths after time elapsed of 0.2 s. The analytical solutions [52] are shown by the black solid lines. The Riemann, Equality, Gurram and Hsu models are shown by the dashed-dot lines, dashed lines, green solid lines, and dots, respectively

for the first time, it is followed by the Equality model. This might be due to the consideration of the total head balances at the junction. Figures 29–30 confirm the best agreement between the numerical and analytical solutions according to [52]
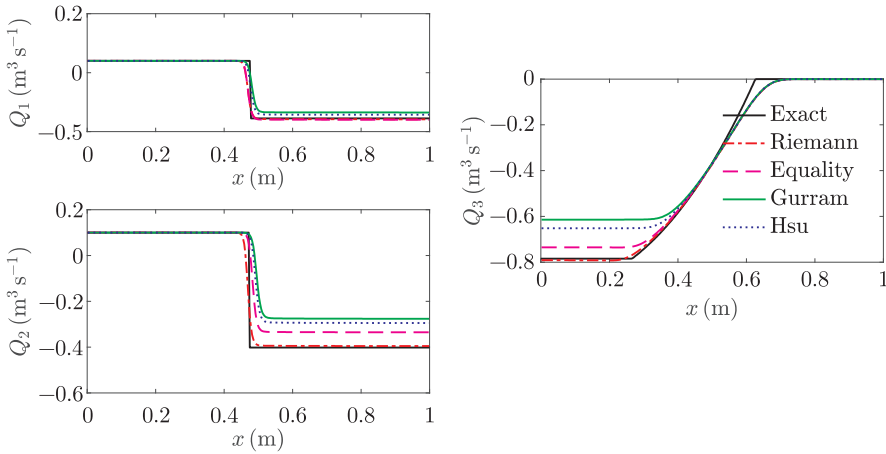
Figure 30. Evolution of water discharges after time elapsed of 0.2 s. The analytical solutions [52] are shown by the black solid lines. The Riemann, Equality, Gurram, and Hsu models are shown by the dashed-dot lines, dashed lines, green solid lines, and dots, respectively

if the Riemann model is used. These results can be qualitatively seen from the listed ℓ^1 errors in Tables 9–10. According to this test case, the solutions by the Gurram and Hsu models fail to match the analytical solutions even with a small downstream Froude number Fr. It might be due to the violation of the total head balance at the junction.

4.6. Conclusion and summary

In this research we investigate the use of an extended Riemann problem solution to set up the internal boundary conditions at the junction in order to perform numerical simulations in open channel networks. The internal boundary conditions are of fundamental importance to develop a well posed numerical scheme for the 1D-SWE. The proposed model is known as the Riemann model. A brief description of the Riemann solution is referenced to the results obtained in Chapter 3. The other junction models such as the Equality, Gurram, Hsu models are also presented. The Gurram and Hsu models are modified to adopt to the current study. A full comparison between the junction models (Riemann, Equality, Gurram and Hsu models) is made in the steady flows over asymmetrical and symmetrical confluences. A set of experiments are numerically reproduced. Both lateral concordant and discordant beds are considered at the junction. In general, the Riemann model is fairly matching the experimental data despite the angle or the geometric shape of the junction. Thus, this study claims poor performance in fitting the experimental data if the Equality model is used. Stressing the importance of the junction angle, the Gurram and Hsu models give better performance in fitting the experimental data obtained in asymmetrical confluence of the equal channel width and a concordant bed for different junction angles. Fr ranges from 0.5 to 0.7. On the contrary, for the asymmetrical confluence

with a non-equal channel width and with a lateral discordant bed and for the Y-shaped confluence, the Gurram and Hsu models are mismatched with respect to the reference experimental data even with Fr smaller than 0.35. In unsteady flows over symmetrical confluences with concordant and discordant beds, the Riemann model shows the best agreement to the analytical solution given in [43] for the concordant bed. For the discordant bed, the same results are obtained in matching the analytical solutions given in [52]. The Gurram and Hsu models mismatch the analytical solutions and are outperformed by the Equality model. This might be due to the violation of the total head balances at the junction. Finally, we conclude that the Riemann model is a good choice to supply the internal boundary conditions instead of the other junction models such as the Equality, Gurram, and Hsu models. It includes the following benefits: lack of empirical coefficients, avoiding complicated models and maintaining a large range of applicability of the solution. It is as easy to use as the Equality model, so it can be attractive for model developers. The Riemann solution is supported by theoretical findings proving its existence and uniqueness. The overall behavior is generally satisfying.

5. Final remarks

In this paper we have shown that the Riemann problem is well posed at the junction network. The Riemann problem is first defined at the junction network for symmetric cases. The Riemann solution is given in the framework shown by [43]. Indeed, the Riemann problem is newly extended to the non-symmetric case, where the channel width variation and bed discontinuities at the junction are considered. The extended Riemann problem is proven to be well posed. The Riemann solution is shown to exist and be unique under subcritical flow conditions, and thus, the necessary physical conditions are given to provide this mathematical evidence. For the forward facing bed step case, sufficient energy is necessary to pass the step where the flow cocking is prohibited. For the backward step bed, the flow might be accelerated, and therefore the relative ratio between the step height and the downstream depth is mandatory, supported by the energy dissipation conditions. The solution of the Riemann problem at the junction network is heavily dependent on the junction curve. The junction curve is shown to be the curve which ensures the conservation of mass and energy. Two types of waves are the main features of the solution. The shock and rarefaction waves are part of the solution. Contact waves might be present at the junction. The results are summarized in a theorem, and this theorem is numerically validated through a set of numerical examples to illustrate the solution structure in the phase plane and with time evolution. The theorem is valid for N number of channels and nodes, as well as for any type of confluences and diffluences. Due to the lack of mathematical evidence (analysis of existence and uniqueness) on such classical models as Equality, Gurram, and Hsu models to supply the inner boundary conditions at the junction, for numerical purposes, the extended Riemann solution (the Riemann model) is used. The Riemann model proves to be a proper choice. The Riemann model is supported by

theoretical findings, which are discussed above. The missing part is how convenient it is to use the Riemann model to supply the inner boundary conditions to perform 1D numerical simulations in channel networks. The advantages and disadvantages of the Riemann model compared to the classical model are shown. A set of experimental data has been used to test each model for steady state flows in channel networks (asymmetric and symmetric confluences). The Riemann model proves to perform well with an acceptable error in all simulations. The Equality model continues to give poor results, in particular with a Froude number greater than 0.35. The Riemann model has the best results in matching the experimental data if the bottom becomes discontinuous at the junction. The modified Gurram and Hsu models shown in Appendices A and B failed in comparison with the Riemann model to best match the experimental results since the bottom becomes discontinuous at the junction, even with a Froude number smaller than 0.35. For unsteady state flow simulations, the Riemann model continues to show the best results among the other junction models for matching the analytical solutions provided in [43, 52]. However, the performance of the junction models remains questionable due to the missing experimental data that could be used to validate them. Based on the results shown in Chapter 4, the Riemann model is considered to be a good choice in supplying the inner boundary conditions and includes the following advantages:

– No empirical coefficients that would limit the applicability of the model are involved.
– The Riemann model is physically and mathematically identical to the SWE.
– The Riemann model is as simple as the Equality model, which attracts software developers.
– The Riemann model can be used for networks consisting of N number of channels and nodes.
– The Riemann model is an energy-based model that can be modified to also include the energy loss in the system.
– The Riemann model is not limited to a specific network configuration. It is valid for both confluences and diffluences.

We conclude that the Riemann model can be used to supply the inner boundary conditions that are supported by the theoretical findings proven in this paper.

Appendix A

The modified Gurram model

In this appendix we introduce the modified Gurram formula. Taking into account the assumptions made by [10]. The flow is assumed to be steady with a small bottom slope. The friction slope is nearly compensated. The flow is nearly 1D in the main channel. The momentum and energy coefficients (β_1 at AB, β_3 at CD, and γ at CD) are assumed to be unity. Flowing towards the junction, the water flow in the lateral channel is accelerated due to the flow contraction at the

separation zone [10] and therefore the lateral momentum M_2 at EH in the later channel Figure 21 is written as

$$M_2 = \beta_2 \rho b_2 h_2 u_2^2 \cos(\delta) \tag{211}$$

where ρ is the water density and β_2 is the lateral momentum coefficient in the lateral channel. [10] highlighted that β_2 can be computed through the following relationship

$$\beta_2 = \frac{b_3 h_3 u_3}{b_2 h_2 u_2} \frac{\cos(\alpha)}{\cos(\delta)} \tag{212}$$

α is the angle between the representative lateral velocity vector at EH and the main channel direction. A relation between α and δ is due to [49] where

$$\alpha = \frac{8}{9}\delta \tag{213}$$

Due to the presence of the bed step in the lateral channel, the flow mixing is expected to increase, in particular between the upstream and the lateral channels. The relationship between δ and α has to be recalibrated. However, it is beyond the aim of this work. Hence, the suggestion of [49] is maintained. Assuming the hydrostatic pressure distribution, the force exerted by the lateral bottom step determined according to [52], the equality of the water level rather than the equality of the water depth between the upstream main channel and the lateral channel, and taking into account the angle Ω, then the momentum balance in the main downstream channel direction over the control volume ABCDEH in Figure 21 gives

$$\rho b_1 h_1 u_1^2 \cos(\Omega) + \frac{\rho g}{2} b_1 h_1^2 \cos(\Omega) + \rho b_3 h_3 u_3 u_2 \cos(\alpha) +$$
$$rhog b_2 h_s z_2 \cos(\delta) = \rho b_3 h_3 u_3^2 + \frac{\rho g}{2} b_3 h_3^2 \tag{214}$$

where h_s refers to the depth over the lateral bed step. It is determined by applying the conservation of the total head over the step. Only the subcritical solution is considered and the other solutions are omitted as shown in [52]

$$h_s = \frac{1}{3}\left(h_3 + \frac{u_3^2}{2g} - z_2\right)\left(1 - 2\cos\left(\frac{2\pi + \theta}{3}\right)\right) \tag{215}$$

such that

$$\theta = \arccos\left(1 - 27\left(\frac{-h_3 - \frac{u_3^2}{2g} + z_2}{\left(\frac{h_1 u_1}{h_3 u_3}\right)^2 \left(\frac{h_3^2 u_3^2}{g}\right)^{\frac{1}{3}}}\right)\right) \tag{216}$$

For more about the total head concept in a single open channel, we refer to the handbook of [16]. Thus, the work of [62, 52] is appreciated for single open channel and channel networks.

Multiplying Equation (214) by $2/b_3 h_3^2$ gives

$$
\begin{aligned}
&\left(\frac{2b_1 h_1 u_1^2}{g b_3 h_3^2} + \left(\frac{b_1}{b_3}\right)\left(\frac{h_1}{h_3}\right)^2\right)\cos(\Omega) + \frac{2u_2 u_3}{g h_3}\cos(\alpha) + \\
&\left(\frac{2b_2}{b_3}\right)\left(\frac{h_s}{h_3^2}\right)z_2\cos(\delta) = \frac{2u_3^2}{g h_3} + 1
\end{aligned}
\tag{217}
$$

The continuity equation implies:

$$
b_1 h_1 u_1 + b_2 h_2 u_2 = b_3 h_3 u_3
\tag{218}
$$

Using the equality of the water level upstream the junction and substituting Equation (218) into Equation (217) and with some arrangement we obtain

$$
\begin{aligned}
&\left(\frac{h_1}{h_3}\right)^3\cos(\Omega) - \left(\frac{b_3 h_1}{b_1 h_3}\right)\left[1 + 2\mathrm{Fr}^2 - \left(\frac{2b_2}{b_3}\right)\left(\frac{h_s}{h_3^2}\right)z_2\cos(\delta)\right] + \\
&2\mathrm{Fr}^2\left[\left(\frac{h_1 u_1}{h_3 u_3}\right)^2\cos(\Omega) + \left(\frac{b_3^2 h_1}{b_1 b_2(h_1 - z_2)}\right)\left(1 - \frac{b_1 h_1 u_1}{b_3 h_3 u_3}\right)\cos(\frac{8\delta}{9})\right] = 0
\end{aligned}
\tag{219}
$$

where

$$
\mathrm{Fr} = \sqrt{\frac{\gamma u_3^2}{g h_3}}
\tag{220}
$$

Indeed, Equation (219) gives the final Gurram formula that is used in the Gurram model shown in System (156)−(158).

Appendix B

The modified Hsu model

This appendix contains a derivation of the modified Hsu formula in the channel network (Figure 21). According to [40], the flows are shown to be accelerated due to the flow contraction at the separation zone as long as the flow towards the junction. Taking into account such effect, the momentum coefficients are introduced (β_1 at AB, β_2 at FG, β_3 at CD, and β_t at EH (Figure 21)). In addition to that, assuming a steady flow, the hydrostatic pressure distribution, neglecting the friction force, taking into account the angle Ω shown in Figure 21, the acting force due to the presence of the lateral step, and further assuming $\beta_1 = \beta_2 = \beta_3 = \beta_t$, then the momentum balance in the main downstream channel direction over the area ABCDEH shown in Figure 21 gives

$$
\begin{aligned}
&\beta\rho b_1 h_1 u_1^2\cos(\Omega) + \frac{\rho g}{2}b_1 h_1^2\cos(\Omega) + \beta\rho b_2 h_2 u_2 u_t\cos(\alpha) + \rho g b_2 h_s z_2\cos(\delta) = \\
&\beta\rho b_3 h_3 u_3^2 + \frac{\rho g}{2}b_3 h_3^2
\end{aligned}
\tag{221}
$$

where u_t is the representative velocity at EH and t refers to the entrance of the lateral channel at the junction. According to [40], the representative velocity u_t is related to the angle α by the following relationship

$$
u_t = \frac{b_2 h_2 u_2}{b_t h_t \sin(\alpha)}
\tag{222}
$$

b_t and h_t are the channel width and the water depth at section EH in the lateral channel, respectively. Substituting Equation (222) into Equation (221). We get

$$\beta \rho b_1 h_1 u_1^2 \cos(\Omega) + \frac{\rho g}{2} b_1 h_1^2 \cos(\Omega) + \frac{\beta \rho (b_2 h_2 u_2)^2}{b_t h_t} \cot(\alpha) + b_2 h_s z_2 \cos(\delta) = \\ \beta \rho b_3 h_3 u_3^2 + \frac{\rho g}{2} b_3 h_3^2 \tag{223}$$

Furthermore, applying the momentum balance in the lateral channel direction over the area EFGH shown in Figure 21 gives

$$\beta \rho b_2 h_2 u_2^2 + \frac{\rho g}{2} b_2 h_2^2 = \frac{\rho g}{2} b_2 h_t^2 + \frac{\beta \rho (b_2 h_2 u_2)^2}{b_t h_t} \frac{\cos(\delta - \alpha)}{\sin(\alpha)} \tag{224}$$

Finally, taking into account the equality of the water level upstream the junction, letting $b_t = b_2 / \sin(\delta)$, further assuming $h_t = h_2$ based on the experimental observation by [40], taking into account the effect of the lateral bottom step h_s [62, 52], using the mass continuity equation, and substituting Equation (224) into Equation (223), we obtain

$$\left(\frac{h_1}{h_3} \right)^3 \cos(\Omega) - \left(\frac{b_3 h_1}{b_1 h_3} \right) \left[1 + \frac{2\beta \mathrm{Fr}^2}{\gamma} - \left(\frac{2b_2}{b_3} \right) \left(\frac{h_s}{h_3^2} \right) z_2 \cos(\delta) \right] + \frac{2\beta \mathrm{Fr}^2}{\gamma} \\ \left[\left(\frac{h_1 u_1}{h_3 u_3} \right)^2 \cos(\Omega) + \left(\frac{b_3^2 h_1}{b_1 b_2 (h_1 - z_2)} \right) \left(1 - \frac{b_1 h_1 u_1}{b_3 h_3 u_3} \right) \cos(\delta) \right] = 0 \tag{225}$$

Equation (225) represents the modified Hsu formula in the System (159).

References

[1] Warner J C, Geyer W R and Lerczak J A 2005 *Journal of Geophysical Research: Oceans*, Wiley Online Library, **110** (C5)

[2] de Saint-Venant A J C, Barré 1871 *Comptes Rendus des séances de l'Académie des Sciences* **73** 237

[3] Alcrudo F and Benkhaldoun F 2001 *Computers & Fluids*, Elsevier, **30** (6) 643

[4] LeFloch P G, Thanh M D *et al.* 2007 *Communications in Mathematical Sciences*, International Press of Boston, **5** (4) 865

[5] Williams M A J 2009 *Global and Planetary Change*, Elsevier, **69** (1) 1

[6] Kesserwani G, Ghostine R, Vazquez J, Ghenaim A and Mosé R 2008 *International journal for numerical methods in fluids*, Wiley Online Library, **57** (12) 1695

[7] Kesserwani G, Ghostine R, Vuez J, Mosé R, Maher A and Ghenaim A 2008 *Advances in Water Resources*, Elsevier, **31** (2) 287

[8] Taylor E H 1944 *Transactions of the American Society of Civil Engineers*, ASCE, **109** (1) 893

[9] Akan A O and Yen B C 1981 *Journal of the Hydraulics Division*, ASCE, **107** (6) 719

[10] Gurram S K, Karki K S and Hager W H 1997 *Journal of Hydraulic Engineering*, American Society of Civil Engineers, **123** (5) 447

[11] Hsu C C, Lee W J and Chang C H 1998a *Journal of Hydraulic Engineering*, American Society of Civil Engineers, **124** (8) 847

[12] Shabayek S, Steffler P and Hicks F E 2002 *Journal of Hydraulic Engineering*, American Society of Civil Engineers, **128** (9) 821

[13] Stoker J J 1957 *Water Waves – The Mathematical Theory With Applications*, Interscience publishers Ltd., London

[14] Toro E F 2009 *Riemann solvers and numerical methods for fluid dynamics*, Springer Science & Business Media

[15] Chow V T 1959 *Open channel hydraulics*, McGraw-Hill Book Company, Inc; New York

[16] Henderson F M 1996 *Open channel flow*, Macmillan

[17] Lax P D 1973 *Hyperbolic systems of conservation laws and the mathematical theory of shock waves*, SIAM

[18] LeVeque R J 1992 *Numerical methods for conservation laws*, Springer, **132**

[19] Dal M G, Murat F *et al.* 1995 *Journal de mathématiques pures et appliquées* **74** 483

[20] Temam R 1984 *Navier-stokes equations*, North-Holland Amsterdam, **2**

[21] Bernetti R, Titarev V A and Toro E F 2008 *Journal of Computational Physics*, Elsevier, **227** (6) 3212

[22] LeFloch P G 2002 *Hyperbolic Systems of Conservation Laws: The theory of classical and nonclassical shock waves*, Springer Science & Business Media

[23] Valiani A and Caleffi V 2008 *Advances in Water Resources*, Elsevier, **31** (3) 447

[24] Colombo R M and Garavello M 2006 *NETWORKS AND HETEROGENEOUS MEDIA*, American Institute of Mathematical Sciences, **1** (3) 495

[25] Colombo R M and Garavello M 2008 *SIAM Journal on Mathematical Analysis*, SIAM, **39** (5) 1456

[26] Colombo R M, Herty M and Sachers V 2008 *SIAM Journal on Mathematical Analysis*, SIAM, **40** (2) 605

[27] Contarino C, Toro E F, Montecinos G I, Borsche R and Kall J 2016 *Journal of Computational Physics*, Elsevier, **315** 409

[28] Garavello M and Piccoli B 2006 *Communications in Partial Differential Equations*, Taylor & Francis, **31** (2) 243

[29] Briani M, Piccoli B and Qiu J-M 2016 *Journal of Scientific Computing* **68** (3) 1101

[30] Fischer H B, List J E, Koh C, Imberger J and Brooks N H 2013 *Mixing in inland and coastal waters*, Elsevier

[31] Müller L O and Blanco P J 2015 *Journal of Computational Physics*, Elsevier, **300** 423

[32] Sturm T W and Tuzson J 2001 *Applied Mechanics Reviews* **54** 107

[33] Cunge J A, Holly F M and Verwey A 1980 *Practical aspects of computational river hydraulics*, Pitman

[34] Zhang Y 2005 *Communications in Nonlinear Science and Numerical Simulation*, Elsevier, **10** (5) 467

[35] Ghostine R, Mose R, Vazquez J, Ghenaim A and Grégoire C 2010 *Journal of Hydraulic Engineering*, American Society of Civil Engineers, **136** (10) 799

[36] Ghostine R, Vazquez J, Terfous A, Mose R and Ghenaim A 2012 *Journal of Hydraulic Research*, Taylor & Francis, **50** (2) 164

[37] Rice C E 1985 *ARS-United States Department of Agriculture, Agricultural Research Service (USA)*

[38] Chang K H, Chang T J and Chiang Y M 2015 *Journal of Hydro-environment Research*, Elsevier

[39] Abbott M B 1966 *An introduction to the method of characteristics*, Thames and Hudson, London

[40] Hsu C C, Wu F S and Lee W J 1998b *Journal of Hydraulic Engineering*, American Society of Civil Engineers, **124** (2) 186

[41] Ramamurthy A S, Carballada L B and Tran D M 1988 *Journal of Hydraulic Engineering*, American Society of Civil Engineers, **114** (12) 1449

[42] Christodoulou G C 1993 *Journal of Hydraulic Engineering*, American Society of Civil Engineers, **119** (3) 409

[43] Goudiaby M S and Kreiss G 2013 *Journal of Hyperbolic Differential Equations*, World Scientific, **10** (03) 431

[44] Graf W H A *et al.* 1998 *Fluvial hydraulics: Flow and transport processes in channels of simple geometry*, **551.483 G7**

[45] Ramana B V 2006 *Higher Engineering Mathematics*, Tata McGraw-Hill Education, **1.14-1.15**

[46] Powell M J D 1970 *Numerical methods for nonlinear algebraic equations* **7** 87

[47] Chanson H 2002 *Hydraulics of stepped chutes and spillways*, CRC Press

[48] Webber N B and Greated C A 1966 *Proceedings of the Institution of Civil Engineers*, Thomas Telford-ICE Virtual Library, **34** (3) 321

[49] Hager W H 1987 *Journal of Hydraulic Engineering*, American Society of Civil Engineers, **113** (4) 539

[50] Pinto C and Márcia M L 2015 *Journal of Hydraulic Research*, Taylor & Francis, **53** (3) 394

[51] Chaudhry M H 1993 *Open channel flow*, Prentice Hall, Englewood Cliffs. New Jersey

[52] Elshobaki M, Valiani A and Caleffi V 2017 *Junction Riemann problem for 1-D shallow water equations with bottom disocntinuities and channel width variations* (unpublished)

[53] Best J L 1985, Birkbeck (University of London)

[54] Biron P, Best J L and Roy A G 1996 *Journal of Hydraulic Engineering*, American Society of Civil Engineers, **122** (12) 676

[55] Biron P, Roy A G and Best J L 1996 *Experiments in Fluids*, Springer, **21** (6) 437

[56] Bradbrook K F, Lane S N, Richards K S, Biron P M and Roy A G 2001 *Journal of Hydraulic Engineering*, American Society of Civil Engineers, **127** (5) 351

[57] Xiao G W and Zhong M Y and Wei D G 2007 *Journal of Hydrodynamics, Ser. B* **19** (5) 587

[58] Aral M M, Zhang Y and Jin S 1998 *Journal of Hydraulic Engineering*, American Society of Civil Engineers, **124** (11) 1125

[59] Borsche R 2016 *Applied Numerical Mathematics*, Elsevier, **108** 157

[60] Dumbser M and Toro E F 2011 *Journal of Scientific Computing*, Springer, **48** (1-3) 70

[61] Chapman S J 2008 *Fortran for scientist and engineers: 1995-2003*, McGraw Hill

[62] Valiani A and Caleffi V 2017 *Advances in Water Resources*, Elsevier, **100** 1

[63] LeVeque R J 2002 *Finite volume methods for hyperbolic problems*, Cambridge university press

[64] Arfken G 1985 *Mathematical Methods for Physicists*, Clarendon Press

[65] Godunov S K 1959 *Matematicheskii Sbornik*, Russian Academy of Sciences, Steklov Mathematical Institute of Russian Academy of Sciences, **89** (3) 271

[66] Harten A, Lax P D and van Leer B 1983 *SIAM review*, SIAM, **25** (1) 35

[67] Einfeldt B 1988 *SIAM Journal on Numerical Analysis*, SIAM, **25** (2) 294

[68] Toro E F, Spruce M and Speares W 1994 *Shock waves*, Springer, **4** (1) 25

[69] Roe P L 1981 *Journal of computational physics*, Elsevier, **43** (2) 357

[70] Engquist B and Osher S 1981 *Mathematics of Computation* **36** (154) 321

[71] Osher S and Solomon F 1982 *Mathematics of computation* **38** (158) 339

[72] Stroud A H 1971 *Approximate calculation of multiple integrals*, Prentice-Hall

[73] Hervouet J-M, Ata R, Audouin Y, Pavan S and Tassi P 2015 *Telemac version 7.0, release notes. Telemac-2D and BIEF* [online] www.opentelemac.org, EDF-R&D V7P2

[74] García N M P and Saviron J M 1992 *Journal of hydraulic research*, Taylor & Francis, **30** (5) 595

[75] Warnecke G and Andrianov N 2004 *SIAM Journal on Applied Mathematics*, SIAM, **64** (3) 878

[76] Bressan A, Crasta G and Piccoli B 2000 *Well-Posedness of the Cauchy Problem for n Xn Systems of Conservation Laws*, American Mathematical Soc., **694**

[77] Bressan A 2000 *Hyperbolic systems of conservation laws: the one-dimensional Cauchy problem*, Oxford University Press

[78] Jacovkis P M 2000 *Southern Hemisphere Paleo-and Neoclimates*, Springer

[79] Burguete J, García N P and Murillo J 2006 *International journal for numerical methods in fluids*, Wiley Online Library, **51** (6) 585

[80] Warren I R and Bach H K 1992 *Environmental Software*, Elsevier, **7** (4) 229

[81] Best J L 1988 *Sedimentology*, Wiley Online Library, **35** (3) 481

[82] Rosatti G and Fraccarollo L 2006 *Journal of Computational Physics*, Elsevier, **220** (1) 312

[83] Chang K H, Chang T J and Chiang Y M 2016 *Journal of Hydro-environment Research*, Elsevier, **13** 76

[84] Toro E F 2013 *Riemann solvers and numerical methods for fluid dynamics: a practical introduction*, Springer Science & Business Media